Nondestructive defect characterization using full-frame spatially structured super resolution laser thermography

vorgelegt von
M.Sc.
Julien Lecompagnon
ORCID: 0000-0001-8614-3296

an der Fakultät V – Verkehrs- und Maschinensysteme
der Technischen Universität Berlin
zur Erlangung des akademischen Grades

Doktor der Ingenieurwissenschaften
- Dr.-Ing. -

genehmigte Dissertation

Promotionsausschuss:

Vorsitzender:	Prof. Dr.-Ing. Dirk Oberschmidt
Gutachter:	Prof. Dr.-Ing. habil. Christian Rupprecht
Gutachter:	Prof. Marco Ricci, PhD

Tag der wissenschaftlichen Aussprache: 31. Oktober 2023

Berlin 2023

Acknowledgements

The presented work has been developed as an external doctoral thesis at the Bundesanstalt für Materialforschung und -prüfung (BAM), Department 8.7: Thermographic Methods in Berlin in cooperation under the supervision of the Chair of Coating Technology at the Institute of Machine Tools and Factory Management at Technische Universität Berlin.

First of all, I would like to thank Prof. Dr.-Ing. habil. Christian Rupprecht for the academic supervision of this work. Prof. Rupprecht has always shown utmost interest and provided invaluable guidance throughout the course of this thesis. In addition, my special sincere gratitude goes to Prof. Marco Ricci, PhD as a recognized expert in nondestructive testing for agreeing to review this thesis. Furthermore, I would like to thank Prof. Dr.-Ing. Dirk Oberschmidt for chairing the doctoral committee.

On top of that, I would like to thank all my colleagues at BAM for their continuous support. First and foremost my sincere gratitude goes to my supervisor Dr. Mathias Ziegler, who has provided unparalleled support and guidance under all circumstances and without whom this work would not have been possible. I am also deeply indebted to Dr. Samim Ahmadi, who excelled at providing the necessary foundational work for this thesis and who has always been a source of valuable discussion. In addition, I would like to express my gratitude for the support I have experienced from my colleagues, specifically, Dr. Christiane Maierhofer†, Philipp Hirsch, Dr. Nelson Pech-May, Dr. Rainer Krankenhagen, Ludwig Rooch, Eileen Nienke, Blerina Mema, Jan Hauffen, Mathias Röllig, Dr. Michael Stamm, Dr. Nils Scheuschner, Philipp Breese, Dr. Simon Altenburg, Simon Oster, Dr. Somsubhro Chaudhuri, Tina Becker, Dr. Christian Metz, Dr. Raphael Bernegger, Christian Hassenstein and Jens-Peter Barow. I would also thank the BAM PhD Programme for funding this work.

Moreover, this endeavor would not have been possible without the continuous support of my friends and family. Especially grateful am I to my beloved wife Theresa Lecompagnon for her selfless support and enduring perseverance without which this work would not have been possible.

Kurzfassung

Die laserbasierte aktive thermografische Prüfung als berührungslose Methode der zerstörungsfreien Werkstoffprüfung (NDT) basiert auf der aktiven Erwärmung des Testobjekts (OuT) und Messung des resultierenden Temperaturanstiegs mit einer Infrarotkamera. Dadurch bedingt können systematische Abweichungen vom vorhergesagten Erwärmungsverhalten Aufschluss über dessen innere Struktur geben. Jedoch ist das Auflösungsvermögen für innenliegende Defekte durch die diffusive Natur der Wärmeleitung in Festkörpern begrenzt. Thermografische Super-Resolution (SR)-Methoden zielen darauf ab, diese Limitation durch die Kombination mehrerer Messungen mit jeweils unterschiedlicher strukturierter Erwärmung und mathematischer Optimierungsmethoden zu überwinden.

Zur Rekonstruktion innerer Defekte mithilfe thermografischer SR-Rekonstruktionsmethodik wird für die Gesamtheit mehrerer Messungen ein schlecht gestelltes und stark regularisiertes inverses mathematisches Problem gelöst, was in einer dünnbesetzten Karte der internen Defektstruktur des OuTs resultiert. Die Inversion mittels iterativer numerischer Minimierungsverfahren profitiert dabei von einzelnen Annahmen wie der vergleichsweisen Seltenheit von Materialdefekten. Nachdem die Methode bisher experimentell fast ausschließlich auf eindimensionale Messbereiche (ROIs) beschränkt war, zielt diese Arbeit auf eine Erweiterung zur Prüfung zweidimensionaler ROIs mit arbiträren Defektverteilungen bei erträglicher experimenteller Komplexität ab. Ziel ist es, durch die Weiterentwicklung des Technologie-Reifegrades (TRL) den Technologietransfer zur industriellen Anwendung zu ermöglichen.

Hierzu werden erst die numerische Erweiterung der SR-Rekonstruktionsmethodik für zweidimensionale ROIs erörtert und zwei neue Algorithmen zur Invertierung des zugrunde liegenden inversen Problems vorgestellt, sowie eine Vorwärtslösung des inversen Problems entwickelt. In Verbindung mit einem neuartigen Algorithmus zur automatisierten Bestimmung der (optimalen) Regularisierungsparameter wird erstmals die Möglichkeit geschaffen, analytische Simulationen zum Einfluss einzelner Parameter auf die erreichbare Rekonstruktionsqualität durchzuführen. Weiterhin wird der experimentelle Ansatz zur Prüfung zweidimensionaler ROIs erweitert. Mehrere Messkampagnen validieren die eingeführten Inversionsalgorithmen, die Vorwärtslösung und zwei exemplarische analytische Studien. Für die experimentelle Umsetzung wird erstmals die Verwendung lasergekoppelter DLP-Technologie für die makroskopische thermografische Prüfung nutzbar gemacht, welche die Projektion großflächiger binärer Pixelmuster ermöglicht. Dadurch kann die Anzahl der erforderlichen Messungen pro ROI ohne Qualitätseinbußen erheblich reduziert werden (bis zu 20×).

Abschließend werden die erzielten Rekonstruktionsergebnisse der internen Defektstruktur eines speziell angefertigten OuTs qualitativ und quantitativ mit auf homogener Erwärmung basierenden etablierten Methoden der thermografischen Prüfung verglichen. Hier zeigt sich, dass die weitgehend rauschfreien SR-Rekonstruktionsergebnisse alle Defektrekonstruktionen der betrachteten Referenzmethoden deutlich übertreffen.

Abstract

Laser-based active thermography is a contactless non-destructive testing method to detect material defects by heating the object and measuring its temperature increase with an infrared camera. Systematic deviations from predicted behavior provide insight into the inner structure of the object. However, its resolution in resolving internal structures is limited due to the diffusive nature of heat diffusion. Thermographic super resolution (SR) methods aim to overcome this limitation by combining multiple thermographic measurements and mathematical optimization algorithms to improve the defect reconstruction.

Thermographic SR reconstruction methods involve measuring the temperature change in an object under test (OuT) heated with multiple different spatially structured illuminations. Subsequently, these measurements are inputted into a severely ill-posed and heavily regularized inverse problem, producing a sparse map of the OuT's internal defect structure. Solving this inverse problem relies on limited priors, such as defect-sparsity, and iterative numerical minimization techniques. Previously mostly experimentally limited to one-dimensional regions of interest (ROIs), this thesis aims to extend the method to the reconstruction of two-dimensional ROIs with arbitrary defect distributions while maintaining reasonable experimental complexity. Ultimately, the goal of this thesis is to make the method suitable for a technology transfer to industrial applications by advancing its technology readiness level (TRL).

In order to achieve the aforementioned goal, this thesis discusses the numerical expansion of a thermographic SR reconstruction method and introduces two novel algorithms to invert the underlying inverse problem. Furthermore, a forward solution to the inverse problem in terms of the applied SR reconstruction model is set up. In conjunction with an additionally proposed algorithm for the automated determination of a set of (optimal) regularization parameters, both create the possibility to conduct analytical simulations to characterize the influence of the experimental parameters on the achievable reconstruction quality. On the experimental side, the method is upgraded to deal with two-dimensional ROIs, and multiple measurement campaigns are performed to validate the proposed inversion algorithms, forward solution and two exemplary analytical studies. For the experimental implementation of the method, the use of a laser-coupled DLP-projector is introduced, which allows projecting binary pixel patterns that cover the whole ROI, reducing the number of necessary measurements per ROI significantly (up to 20×).

Finally, the achieved reconstruction of the internal defect structure of a purpose-made OuT is qualitatively and qualitatively benchmarked against well-established thermographic testing methods based on homogeneous illumination of the ROI. Here, the background-noise-free two-dimensional photothermal SR reconstruction results show to outclass all defect reconstructions by the considered reference methods.

Table of Contents

Abbreviations and Symbols XI

1 Introduction 1

2 State of the Art 5

2.1 Principles and Implementations of Active Thermographic Testing 5
2.1.1 Heat Transfer in Solids 7
2.1.2 Heat Sources 12
2.1.3 Measuring Temperature 14
2.1.3.1 Contact Measurement 14
2.1.3.2 Radiometric Measurement 17
2.1.4 Processing of Active Thermographic Data 23
2.2 Defect Resolution in Thermographic Testing 26
2.2.1 Spatial Resolution of the Temperature Measurement 27
2.2.2 Spatial Resolution Limit of Thermal Diffusion 29
2.2.3 Resolution Limits imposed by the Illumination 31
2.3 Resolution Enhancement beyond Classical Limits 34
2.3.1 Geometric Super Resolution 34
2.3.2 Optical Super Resolution 35
2.3.3 Photothermal Super Resolution 36

3 Motivation and Research Objectives 43

3.1 Limitations of Conventional Testing Methods 43
3.2 Challenges for Super Resolution Defect Reconstruction 47
3.3 Research Objectives 47

4 Approach and Implementation 49

4.1 Expanding the Numerical Inversion of the Photothermal SR Problem 49
4.1.1 Sparse Matrix Stacking 52
4.1.2 Inversion in Frequency Space 56
4.2 Experimental Implementation 58
4.2.1 Sequential Laser Scanning 58

4.2.2 Two-dimensional Pattern Projection . . . 61
4.3 Numerical Modelling . . . 65
4.3.1 Forward Solution . . . 66
4.3.2 Automatic Inversion Parameter Determination . . . 67
4.3.3 Photothermal Super Resolution Parameter Studies . . . 71
4.3.3.1 Pixel Cluster Size . . . 72
4.3.3.2 Number of Projected Patterns . . . 74

5 Experimental Validation and Results 79
5.1 Object Under Test . . . 79
5.2 Sequential Laser Scanning . . . 82
5.2.1 Laser Scanning Setup . . . 82
5.2.2 Reconstruction Results . . . 84
5.3 Two-dimensional Pattern Projection . . . 86
5.3.1 Projection of Illumination Patterns . . . 86
5.3.2 Reconstruction Results . . . 91
5.3.3 Validation of the Forward Solution . . . 93

6 Discussion of the Results 97
6.1 Comparison Metrics . . . 98
6.2 Sequential Laser Scanning . . . 100
6.3 Two-dimensional Pattern Projection . . . 103
6.4 Key Result Summary and Observed Limitations . . . 106

7 Conclusion and Outlook 107
7.1 Summary . . . 107
7.2 Outlook . . . 110

Appendices 115
A1 Derivation of the Fourier Transform of the Thermal Point Spread Function . . . 115
A2 Derivation of the Fourier Transform of a Gaussian Beam Profile . . . 116
A3 Derivation of the Thermal Sparrow Limit . . . 116
A4 Achievable Irradiances using DLP-based Projectors . . . 118

Related Author's Publications 121

References 125

List of Figures and Tables 135

Abbreviations and Symbols

Abbreviations

Abbreviation	Description
ADMM	alternating direction method of multipliers
AI	artificial intelligence
AM	additive manufacturing
AT	acoustic emission testing
BAM	Bundesanstalt für Materialforschung und -prüfung
BC	boundary condition
CCD	charge-coupled device
CDF	cumulative distribution function
CMOS	complementary metal-oxide-semiconductor
CS	compressed sensing
CT	computed tomography
DE	differential evolution
DFT	discrete Fourier transform
DLP	digital light processing
DMD	digital micromirror device
DT	difference thermography
EFNDT	European Federation for NDT
ET	eddy current testing
FFT	fast Fourier transform
FISTA	fast iterative shrinkage-thresholding algorithm
FMC	full matrix capture
FPGA	field-programmable gate array
FWHM	full width at half maximum
I/O	input/output
IC	initial condition
IoU	intersection over union
IR	infrared
LCD	liquid crystal display

Abbreviation	**Description**
LED	light emitting diode
LWIR	longwave infrared
MEMS	micro-electro-mechanical system
MT	magnetic testing
MTF	modulation transfer function
MWIR	midwave infrared
NDT	nondestructive testing
NETD	noise equivalent temperature difference
NIR	near infrared
NMSE	normalized mean square error
NTC	negative temperature coefficient
OTF	optical transfer function
OuT	object under test
PBF-LB	laser powder bed fusion
PDE	partial differential equation
PhTF	phase transfer function
PPT	pulsed phase thermography
PSF	point spread function
PT	penetrant testing
PTC	positive temperature coefficient
ROI	region of interest
RT	radiographic testing
RTD	resistance temperature detector
SBR	signal-to-background ratio
SIM	structured light microscopy
SNR	signal-to-noise ratio
SR	super resolution
SSIM	structural similarity
STED	stimulated emission depletion
SWIR	shortwave infrared
TRL	technology readiness level
TSR	thermal signal reconstruction
TT	thermographic testing
TTL	transistor–transistor logic
TU	technical university
UT	ultrasonic testing
VT	visual testing
VW	virtual wave

Symbols

Symbol	Description	Unit
a	heat source distribution	-
a_{ext}	external heat source distribution	-
a_{illum}	distribution of the external illumination	-
a_{int}	internal heat source distribution	-
a_{rec}	reconstructed (internal) heat source distribution	-
A	(cross-sectional) area	m^2
$A_{\text{background}}$	background signal amplitude	-
A^n_{fft}	amplitude of the nth frequency in frequency space	$\mathrm{K}/\sqrt{\mathrm{Hz}}$
A_{signal}	signal amplitude	-
α	thermal diffusivity	m/s^2
β	pattern fill factor	-
β	polar angle	rad
$\mathcal{B}$	domain boundary	-
c	propagating wave speed	m/s
c	speed of light in vacuum ($2.997\,924\,58 \cdot 10^8$)	m/s
c_p	specific heat capacity	J/(kg K)
d_{defect}	lateral (spherical) defect width	mm
d_{OuT}	side length of the OuT	mm
d_{pix}	size of a single projected pixel	mm
d_{sep}	separation distance between neighboring defects	mm
d_{spix}	size of a projected cluster of pixels	mm
d_{spot}	diameter of the illumination spot	mm
D	general diffusion coefficient	m^2/s
D_{optics}	diameter of an optical aperture	mm
$\mathcal{D}$	problem domain	-
e	thermal effusivity	$\mathrm{W}\sqrt{\mathrm{s}}/(\mathrm{m}^2\mathrm{K})$
ε	(spectral) emissivity	-
f	general frequency	1/m, 1/s
$f(x)$	general scalar function: $f : x \to y$, with $x \in \mathbb{R}^n, y \in \mathbb{R}$	-
$f_{\#}$	f-number of an optical system	-
f_{cam}	sampling frequency	Hz
f_{fft}	frequency component of a FFT analysis	Hz
f_{focal}	focal length	mm
F	external force	N
F_o	Fourier number	-
G_{heat}	Green's function of the heat PDE	$\mathrm{m}^{-n_{\text{dim}}}$

Symbol	**Description**	**Unit**
G_{wave}	Green's function of the wave PDE	1/s
γ_{defect}	aspect ratio (width/depth) of an internal defect	-
γ_{sep}	aspect ratio in terms of (separation distance/defect depth)	-
h	convective heat transfer coefficient	$\mathrm{W/(m^2\,K)}$
h	Planck constant ($6.626\,070\,15 \cdot 10^{-34}$)	J/Hz
I	electrical current	A
I_0	intensity amplitude	W
I_θ	spectral intensity	W/(sr nm)
I_t	temporal structure	-
$I_{x,y}, I_r$	spatial structure	-
J	diffusion flux	$\mathrm{mol/(m^2\,s)}$
k	thermal conductivity	W/(m K)
$k_{A\to B}$	thermoelectric coefficient over a material transition $A \to B$	µV/K
k_b	Boltzmann constant ($1.380\,649 \cdot 10^{-23}$)	J/K
$K(\lambda)$	luminous efficacy for a wavelength λ	lm/W
L	plate thickness	m
L_{defect}	depth below the surface at which the defect is located	m
L_{diff}	thermal diffusion length	m
L^n_{fft}	diffusion length of the nth frequency in frequency space	$\mathrm{K}/\sqrt{\mathrm{Hz}}$
L_{ROI}	side length of the ROI	m
L_λ	spectral radiance	$\mathrm{W/(m^3\,sr)}$
λ	wavelength	µm
λ_2	strength of the ℓ_2-norm regularizer	-
$\lambda_{2,1}$	strength of the $\ell_{2,1}$-norm regularizer	-
$n_{\mathrm{clustered}}$	number of pixels clustered together to act as a unit	-
n_{dim}	dimensionality of heat flow	-
n_{fft}	nth frequency component	-
n_{iter}	number of iterations	-
n_{m}	number of measurements	-
$n_{\mathrm{pix,on}}$	number of activated pixels per illumination pattern	-
$n_{\mathrm{pix,total}}$	total number of pixels per illumination pattern	-
n_{t}	number of samples in time	-
$n_{\mathrm{x}}, n_{\mathrm{y}}$	number of samples in space	-
$\mathcal{N}_{\mathrm{noise}}$	Gaussian Noise	K
ω_{wave}	angular velocity of the thermal wave	rad/s
Ω	solid angle	$\mathrm{m^2/m^2}$
p	pressure	$\mathrm{N/m^2}$
P	radiant power	W

Symbol	**Description**	**Unit**
ϕ	molar concentration	mol/m^3
ϕ_{fft}^n	phase angle of the nth frequency in frequency space	rad
Φ	radiant flux	W
Φ_λ	spectral flux	W/nm
Φ_v	luminous flux	lm
Φ_{PSF}	(thermal) point spread function	K
q	heat flux density	W/m^2
q_{source}	heat source density	W/m^3
$\dot{Q}$	heat flow	W
$\hat{Q}$	amplitude of the heat flow	W
r_d	measurement grid spacing	m
R	thermal wave reflection coefficient	-
R_{RTD}	temperature dependent resistance	Ω
ρ	mass density	kg/m^3
ρ_{ADMM}	ADMM penalty parameter	-
S_A	Seebeck coefficient of material A	µV/K
σ	Stefan–Boltzmann constant $(5.670\,374\,419 \cdot 10^{-8})$	W/(m^2 K^4)
σ_{noise}	standard deviation of Gaussian noise $\mathcal{N}_{\mathrm{noise}}$	-
t	time	s
t_{diff}	thermal diffusion time	s
T	temperature	K
T_{amb}	ambient temperature	K
T_0	initial temperature	K
T_{diff}	temperature difference to T_0	K
T_{fft}^n	thermal frequency content of the nth frequency	K/$\sqrt{\mathrm{Hz}}$
T_∞	(incoming) fluid temperature	K
Δt	temporal resolution	s
u	general wave amplitude	-
U	voltage	V
v_{wave}	(phase) velocity of the thermal wave	m/s
V	volume	m^3
ζ	defect signal strength	-
ζ_0	spatial frequency cut-off	1/mm
ζ_r	spatial frequency	1/mm
x, y, z	spatial coordinates	m
$\Delta x, \Delta y$	spatial resolution	m

1. Introduction

Nondestructive testing (NDT) comprises a wide field of analytical methods that are used to evaluate the properties of a material, component or system without causing damage to the object under test or alter its properties. Furthermore, NDT methods are used to detect, characterize and localize defects or irregularities in the material or component and are used to ensure the quality of a product, to determine its fitness for use or to monitor its condition during operation. NDT methods are used in a wide range of industries, such as the automotive, aerospace, energy, construction, electronics, medical, and manufacturing industries. The economic importance of NDT is reflected by the fact that the global NDT market is estimated to be sized at multiple billion US-dollars [1, 2].

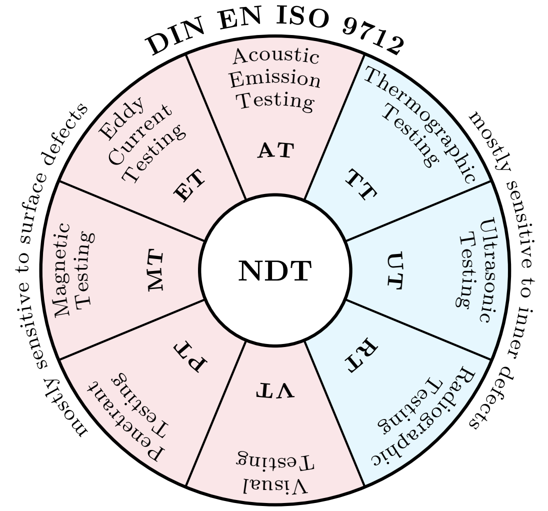

Figure 1.1: Selection of different NDT methods according to DIN EN ISO 9712:2022-09 (Tab. 1) [3]. Commonly, the methods are further differentiated on whether they are sensitive to detecting defects in the bulk (blue background) or to detecting surface defects (red background).

NDT methods can be categorized according to the physical principle they are based on. The most common NDT methods are based on the fundamental physical principles of electromagnetism (eddy current testing, magnetic testing), acoustics (ultrasonic testing, acoustic emission testing) and thermodynamics (thermographic testing) as displayed in Figure 1.1. Each of the presented methods, commonly abbreviated by a two-letter acronym (e.g., thermographic testing: TT), features its own set of individual advantages governing its use in industry. As NDT methods are paramount for product or even public safety, national regulatory bodies are responsible for the certification of NDT methods and the qualification of NDT personnel (cf. the 31 current members of the European Federation for NDT [4]).

The selection of which NDT method should be used for an inspection task is commonly based on the type of defect to be detected, the material to be inspected, the size of the region of interest (ROI) and the required spatial resolution [5]. The latter two are commonly in conflict with each other, as the spatial resolution of NDT methods is commonly limited by the size of the ROI. However, a common trend between methods striving towards higher spatial resolution can be observed. While conventional radiographic testing (RT) methods are more and more supplanted by computed tomography (CT) and in ultrasonic testing (UT) the use of sensor arrays for improving its spatial resolution is on the rise, the field of thermographic testing (TT) experiences a similar trend. Even though TT is still mainly limited by the diffusive nature of heat diffusion, which limits its achievable spatial resolution depending on the size and depth of the defect to be detected, the use of high-resolution infrared cameras and the development of novel data processing methods have led to a significant increase in spatial resolution in recent years [6]. This is especially true for thermographic super resolution techniques, which aim to overcome the inherent spatial resolution limit of TT due to the diffusivity of heat flow. While they are still in their infancy, those methods have already shown potential to become a powerful extension to the TT toolbox in the future. More so, exploiting the increase in available computing power is one of the major driving forces in the development of TT methods apart from the ever-increasing performance and significant price reduction of infrared cameras [7] and high-performance heat sources (e.g., high-power, high-efficiency laser sources).

This thesis is contributing to the development of thermographic super resolution (SR) methods by focusing on the expansion of the photothermal SR reconstruction method, which achieves SR by combining multiple thermographic measurements with varying spatially structured photothermal heating[1]. By introducing novel inversion algorithms to the underlying thermal inverse problem and by extending its experimental implementation to the testing of ROIs containing arbitrarily shaped defects utilizing a laser-coupled DLP-projector, the technology readiness level (TRL) of the method is increased from TRL 3 to TRL 4-5. With the introduction of a fully automated method for performing analytical studies on the achievable reconstruction quality of photothermal SR reconstruction, this thesis enables further exploration of the method for easy adaption to different use-cases. All findings are thoroughly validated on a purpose-made object under test and the now improved reconstruction results are benchmarked quantitatively and qualitatively against the results of conventional TT reference methods. Here it is shown that the proposed method is capable of achieving a significant increase in spatial

---

[1] Photothermal heating is the act of heating an object by exposing it to electromagnetic radiation emitted by a light source (laser, LED, halogen lamp, etc.). For opaque objects, the energy of the absorbed light is subsequently converted to heat near the object's surface, causing a heat flow within the object.

resolution compared to conventional TT methods, while also yielding sparse defect maps as a result which make them inherently easily machine-readable and benefit further automated defect classification.

In the following chapters, first, a theoretical background on the physical principles of TT and thermographic SR methods is given (cf. Chapter 2). Then, the research goals of this thesis are discussed (cf. Chapter 3). After that, the performed numerical expansion of the photothermal SR reconstruction method is presented, as well as the adapted experimental approach and the developed automated method for performing analytical studies on the achievable reconstruction quality (cf. Chapter 4). Then, the proposed extensions to the method and the results from the analytical simulations are validated in laboratory experiments (cf. Chapter 5). Finally, the achieved results are discussed and benchmarked against conventional TT reference methods (cf. Chapter 6). The thesis is concluded by a summary of the achieved results and an outlook on future research topics concerning the further progression of the method's TRL (cf. Chapter 7).

2. State of the Art

In the following chapter the current state of the art for thermographic detection of defects, inhomogeneities and other irregularities is laid out. On top of giving an overview of the theoretical background of heat diffusion and temperature measurements, a special emphasis is placed on the detection of internal defects/inhomogeneities and the state of photothermal super resolution techniques preceding this thesis work.

2.1 Principles and Implementations of Active Thermographic Testing

Thermographic testing (TT) makes it possible to nondestructively get an insight into an object by examining its interaction with heat. This interaction is inextricably influenced by the object's geometry, its thermal properties and the environmental conditions. Any deviations in this interaction from prior expectation signals the presence of defects, inhomogeneities or other irregularities (cf. Figure 2.1). Two TT applications are very common in this context, namely inferring the object's geometry when knowing about its thermal properties under known environmental conditions (e.g., thickness determination) and determining the object's thermal properties when its geometry and the environmental conditions are well-known. Primarily, the

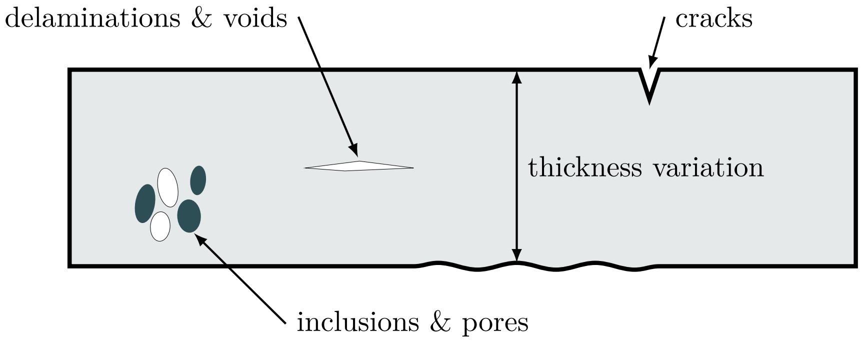

Figure 2.1: Material defects, inhomogeneities and irregularities detectable by thermographic testing.

thermal quantities of interest are the object's thermal diffusivity α and its thermal effusivity e. The thermal diffusivity α – a measure of the object's heat conduction rate – is defined as:

$$\alpha = \frac{k}{c_p \cdot \rho} \; . \tag{2.1}$$

It can be solely described by the object's thermal material properties, namely by the ratio of its thermal conductivity k [W/(m K)] and its volumetric heat capacity $c_p \cdot \rho$ [J/(m^3 K)] given by the product of its mass density ρ [kg/m^3] and its specific heat capacity c_p [J/(kg K)]. The thermal effusivity e – a measure of the object's ability to exchange thermal energy – on the other hand can be calculated from the thermal material properties as follows:

$$e = \sqrt{k \cdot \rho \cdot c_p} \; . \tag{2.2}$$

Similar to the index of refraction governing the propagation of electromagnetic radiation, the thermal effusivity acts as the index value for the propagation of heat. As with electromagnetic radiation, the propagation of heat in a solid body also experiences refraction at an interface where the effusivity of on side of the interface (e_1) mismatches the other (e_2). The fraction of reflected heat is characterized by the thermal reflection coefficient R which can be obtained as:

$$R = \frac{e_1 - e_2}{e_1 + e_2} \; . \tag{2.3}$$

In Table 2.1 the thermal diffusivity and effusivity are shown for a selected set of common materials. From these values it can be observed that while air has a fairly high thermal diffusivity, its thermal effusivity is several orders of magnitude lower than that of most relevant solid materials. As a result, on every interface between most solid bodies and air, the thermal reflection coefficient is very close to $R \approx 1$. This gives TT a high sensitivity for detecting sample boundaries, delaminations, inclusions or air-filled cracks.

Table 2.1: Thermal properties of a selected set of materials at 20 °C sorted by effusivity.

Category	**Material**		**diffusivity**	**effusivity**	
	Name	Remark	$\alpha\left[\text{mm}^2/\text{s}\right]$	$e\left[\text{W}\sqrt{\text{s}}/(\text{m}^2\text{K})\right]$	
Metals	Copper	pure	112.72	37.02	[8]
	Aluminium	3.3206	86.61	22.56	[9]
	Steel	1.0038	14.92	13.98	[10]
	Stainless steel	1.4301	3.80	7.70	[11]
Plastics	POM		0.15	0.80	[12]
	PEEK		0.18	0.59	[13]
Gases	Air	$p = 1013.25\,\text{hPa}$	20.57	$5.60 \cdot 10^{-3}$	[14]

Making use of an instationary heat flow in the first place, measuring the impeded heat flow from changes in thermal effusivity, or analogously the reflected thermal wavefront, is one of the main operating principles of active TT, since thermographically detectable defects mostly manifest themselves as areas with a differing thermal effusivity. Furthermore, by evaluating the timing of the reflected signal, it is possible to determine the depth from which it originated from (cf. Equation (2.13): diffusion length). Figure 2.2 shows the interaction of common defects with a transient heat flow.

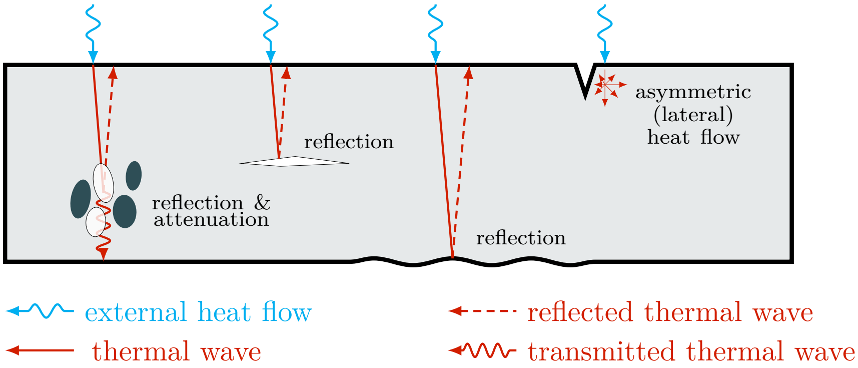

Figure 2.2: Internal defects, inhomogeneities and irregularities impeding heat flow. At every interface of changing thermal effusivity, the incoming thermal wavefront is (partly) reflected. The same object under test as in Figure 2.1 is shown.

2.1.1 Heat Transfer in Solids

In order to understand advantages and limitations of TT it is vital to understand the physics of heat conduction. Every body that is not in internal thermal equilibrium or in thermal equilibrium with its surroundings is subject to an exchange of thermal energy. This energy imbalance is counteracted by a resulting heat flow $\dot{Q}$ [W] and can be facilitated by several mechanisms, mainly via conduction, convection and by a transfer via radiated energy. However, for solid convex bodies and small temperature gradients at adiabatic boundary conditions, thermal conduction is by far the main contributor to the exchange of thermal energy. In 1822, Joseph Fourier laid the foundation to the modern understanding of heat transfer via conduction in his book "*Théorie analytique de la chaleur*" by realizing when examining one dimensional heat flow that the heat flux density $q = \dot{Q}/A$ $[\mathrm{W/m^2}]$ in a solid body is directly proportional to the negative gradient of its temperature field T in space [15]:

$$q \propto -\frac{\partial T}{\partial r} \; . \tag{2.4}$$

The proportionality constant between the heat flux density and the negative temperature gradient has been observed to be the thermal conductivity k $[\mathrm{W/(m\,K)}]$, which is a fundamental material property. The observation that the heat flow in a solid is directly proportional to the spatial derivative of the temperature field directly indicates that the conduction of heat follows the physics of a general diffusion process, which is governed by Fick's first law. This law, stated by Adolf Fick in 1855, initially describing the diffusion process for a chemical concentration differential ϕ, is given in modern form as follows [16, p. 66]:

$$J = -D \cdot \frac{\partial \phi}{\partial x} \ , \tag{2.5}$$

where D [$\mathrm{m^2/s}$] is the general diffusion coefficient, ϕ [$\mathrm{mol/m^3}$] a concentration field and J [$\mathrm{mol/(m^2\,s)}$] the concentration flux. Assuming there is no mass flow in and out of the system and no mass is created within, we can formulate the following equation, which encodes the conservation of mass in the diffusion process (thermal analog: conservation of energy):

$$\frac{\partial \phi}{\partial t} + \frac{\partial J}{\partial r} = 0 \ . \tag{2.6}$$

If Equation (2.5) is inputted into Equation (2.6), we obtain:

$$\frac{\partial \phi}{\partial t} - D \cdot \frac{\partial^2 \phi}{\partial r^2} = 0 \ , \tag{2.7}$$

assuming the coefficient D is not changing in space, i.e., $^{\partial D}/_{\partial r} = 0$. Equation (2.7) is called Fick's second law. In the context of heat conduction, a completely analogous argument can be made to obtain the following homogeneous partial differential equation (PDE) fundamental to all heat conduction processes:

$$\frac{1}{\alpha} \cdot \frac{\partial T}{\partial t} - \frac{\partial^2 T}{\partial r^2} = 0 \ , \tag{2.8}$$

where α is the thermal diffusivity as defined in Equation (2.1).

The diffusive nature of the heat conduction process stands in stark contrast to the propagation behavior of non-diffusive transport processes governed by the general wave equation, as stated in Equation (2.9):

$$\frac{1}{c^2} \cdot \frac{\partial^2 u}{\partial t^2} - \frac{\partial^2 u}{\partial r^2} = 0 \ , \tag{2.9}$$

where u is the wave amplitude/displacement and c is the propagation speed (phase velocity) of the wave. Here, when compared with Equation (2.8), the major difference lies in the second derivative with respect to time of the underlying field, which gives rise to the propagating behavior.

If there are active heat sources in forms of an additional internal or external heat flux density q_{source} [$\mathrm{W/m^3}$] present, Equation (2.8) can be extended by an additional term. This leads to the inhomogeneous representation of the differential equation of heat conduction:

$$\frac{1}{\alpha} \cdot \frac{\partial T}{\partial t} - \frac{\partial^2 T}{\partial r^2} = \frac{c_p \cdot \rho}{\alpha} \cdot q_{\text{source}} \ . \tag{2.10}$$

An important tool to characterize heat flow phenomena is the Fourier number. It is defined as a dimensionless number and resembles the ratio between the diffusive transport rate and the rate of the energy storage in the body. The Fourier number can be calculated for a given thermal diffusivity α and a characteristic length L as follows:

$$F_o(t) = \alpha \cdot \frac{t}{L^2} \ . \tag{2.11}$$

Inputting the Fourier number into Equation (2.8) leads to a dimensionless formulation of the heat PDE. Furthermore, a Fourier number of $F_o = 1$ indicates that the penetration depth of the thermal wavefront is equal to the characteristic length L. Thus, this fact allows defining the thermal diffusion time t_{diff} (the time it takes the thermal wavefront to arrive at a distance L) and the thermal diffusion length L_{diff} (the distance at which the thermal wavefront arrives at after a time t) as:

$$t_{\text{diff}}(L) = \frac{L^2}{\alpha} \tag{2.12}$$

$$L_{\text{diff}}(t) = \sqrt{\alpha \cdot t} \ . \tag{2.13}$$

For practical applications, Equation (2.8) needs to be solved constrained to an initial condition (IC) and proper boundary conditions (BCs). This leads to the following formulation for numerically describing any heat flow problem arising within the domain $r = \{(x, y, z) \,|\, x, y, z \in \mathcal{D}\}$:

$$\begin{cases} \dfrac{\partial^2 T}{\partial r^2} = \dfrac{1}{\alpha} \cdot \dfrac{\partial T}{\partial t} & (x, y, z) \in \mathcal{D},\ t > 0 \\ T(r, t = 0) = T_0(r) & \text{(IC)} \\ T(r, t) \text{ satisfies BCs for all boundaries } \mathcal{B} \in \mathcal{D} & \text{(BCs)} \end{cases} \ . \tag{2.14}$$

Commonly used BC are listed in Table 2.2. Especially noteworthy in this context is the special Neumann BC $\partial T(\mathcal{B},t)/\partial \mathcal{B} = 0$, which defines an adiabatic boundary, as it requires the first derivative in space of the temperature field T to be zero (c.f. Equation (2.4)).

Furthermore, an instationary Neumann BC also allows the introduction of an external heat flow acting on the body as it is a common process in active TT (c.f. Figure 2.3). Special Neumann BCs can also be applied for modelling convective ($q \propto T - T_\infty$) and radiative ($q \propto T^4 - T_{\text{amb}}^4$) energy exchange between an object under test (OuT) and its surroundings.

Table 2.2: Common boundary conditions for PDEs for a spatial boundary $\mathcal{B} \in \mathcal{D} \in \mathbb{R}^3$.

Name	**Boundary condition**
Dirichlet	$T(\mathcal{B},t) = f(\mathcal{B},t)$
Neumann	$\begin{cases} \dfrac{\partial T(\mathcal{B},t)}{\partial \mathcal{B}} = q(\mathcal{B},t) & \text{(general form)} \\ \dfrac{\partial T(\mathcal{B},t)}{\partial \mathcal{B}} = h \cdot (T(\mathcal{B},t) - T_\infty) & \text{(convective transfer)} \\ \dfrac{\partial T(\mathcal{B},t)}{\partial \mathcal{B}} = \varepsilon \cdot \sigma \cdot \left(T^4(\mathcal{B},t) - T^4_{\text{amb}}\right) & \text{(radiative transfer)} \end{cases}$
Periodic	$\left.\begin{aligned} T(\mathcal{B}_1,t) &= T(\mathcal{B}_2,t) \\ \dfrac{\partial T(\mathcal{B}_1,t)}{\partial \mathcal{B}_1} &= \dfrac{\partial T(\mathcal{B}_2,t)}{\partial \mathcal{B}_2} \end{aligned}\right\}$ for $\mathcal{B}_1$ opposing $\mathcal{B}_2$

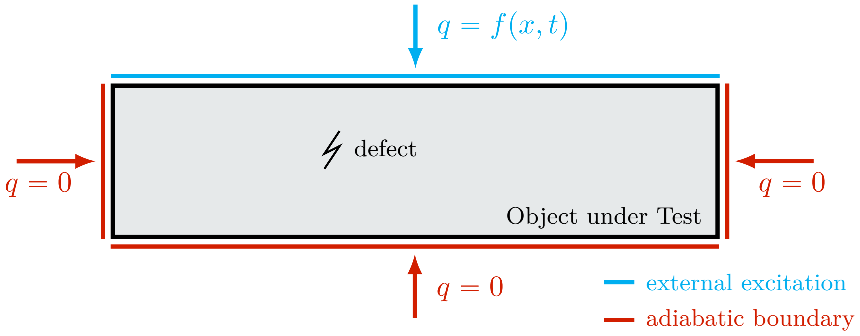

Figure 2.3: OuT with simplified BCs typical for TT. For a small increase in temperature and a large OuT the BCs can be mostly viewed as adiabatic: ${}^{\partial T(\mathcal{B},t)}/_{\partial \mathcal{B}} = 0$.

For finding solutions for the homogeneous heat PDE for instationary Neumann BCs, a Green's function representation of Equation (2.8) can be utilized:

$$T(r,t) = \iint\limits_{\mathcal{D},\ t>0} G(s,\tau) \cdot f(r-s, t-\tau)\, \mathrm{d}s\, \mathrm{d}\tau = G(r,t) *_{r,t} f(r,t) \ , \tag{2.15}$$

where $G(r,t)$ is the Green's function of Equation (2.8), $f(r,t)$ is the boundary condition and $*_{r,t}$ is the convolution operator in space and time. The Green's function essentially is the impulse response of the body to a Dirac-pulse like heat flow in space and time. This means that $G(r,t)$ has to be formulated such that it not only has to be a solution to Equation (2.8) but to the inhomogeneous heat PDE for a localized heating pulse:

$$\begin{gathered} \frac{1}{\alpha} \cdot \frac{\partial G(r-s,t-\tau)}{\partial t} - \frac{\partial^2 G(r-s,t-\tau)}{\partial r^2} = \delta(x-s) \cdot \delta(t-\tau) \ , \\ \text{with } -\infty < s < \infty,\ 0 \leqslant t, \tau \ . \end{gathered} \tag{2.16}$$

For the heat PDE, the following (unique) solution for $G(r,t)$ exists [17]:

$$G_{\text{heat}}(r,t) = \frac{1}{(4\pi \cdot \alpha \cdot t)^{n_{\text{dim}}/2}} \exp\left(-\frac{\|r\|_2^2}{4 \cdot \alpha \cdot t}\right) \ , \tag{2.17}$$

where $n_{\text{dim}} \mathrel{\widehat{=}}$ dimensionality of the heat flow ($n_{\text{dim}} = 1$ for homogeneous heating over the region of interest (ROI), $n_{\text{dim}} = 2$ for line-shaped heating, $n_{\text{dim}} = 3$ for point-like heating).

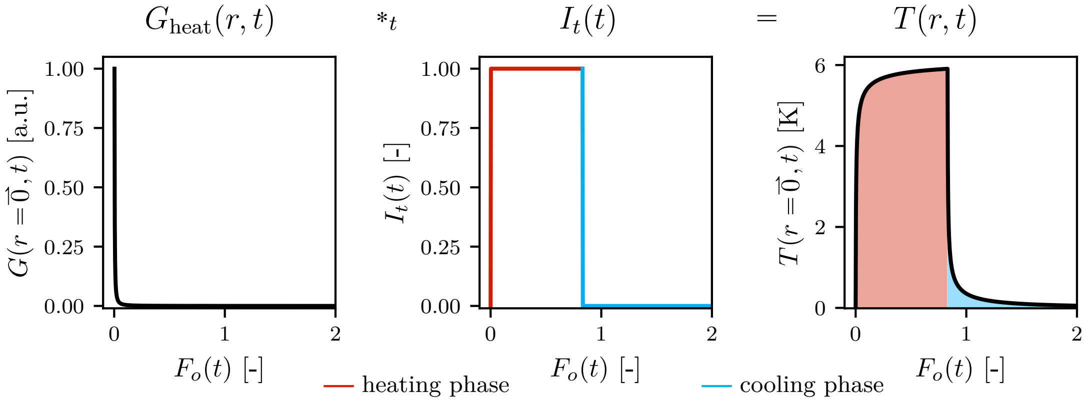

Figure 2.4: Principle of adding instationary BCs via a convolution with the Green's function of the heat PDE: in this example, the thermal response $T(r,t)$ at $r = \vec{0}$ of a thermally thick body to an external intermittent heat flow with shape $I_t(t)$ is evaluated.

With the help of Equation (2.15), it is now possible to express the temperature evolution for any semi-infinite body as the convolution of the Green's function from Equation (2.17) with the temporal structure $I_t(t)$ and the spatial structure $I_r(r)$ of the external heating:

$$T(r,t) = G_{\text{heat}}(r,t) *_t I_t(t) *_r I_r(r) \ , \tag{2.18}$$

as is illustrated in Figure 2.4.

In a similar way, a Green's function representation can also be found for the wave equation as shown in Equation (2.9). Here, the corresponding Green's function is defined as follows [18, Eq. 3.5.11]:

$$G_{\text{wave}}(r,t) = c \cdot \frac{\delta\left(\|r\|_2 - c \cdot t\right)}{4\pi \cdot \|r\|_2} \ . \tag{2.19}$$

2.1.2 Heat Sources

Due to the fact that the basic function principle of TT relies on measuring the response of an OuT to a heat flow, causing/creating a heat flow (i.e., a temperature gradient) is an essential part of any active TT process. Depending on whether the object is deliberately exposed to an external heat flow, because of excess internal heat or whether a thermodynamic imbalance to the environment is exploited, TT can be categorized into *active* and *passive* variants [19]. Exemplary testing scenarios are shown in Figure 2.5. While passive TT proves useful whenever a heat flow is either induced by a change in environmental conditions, in

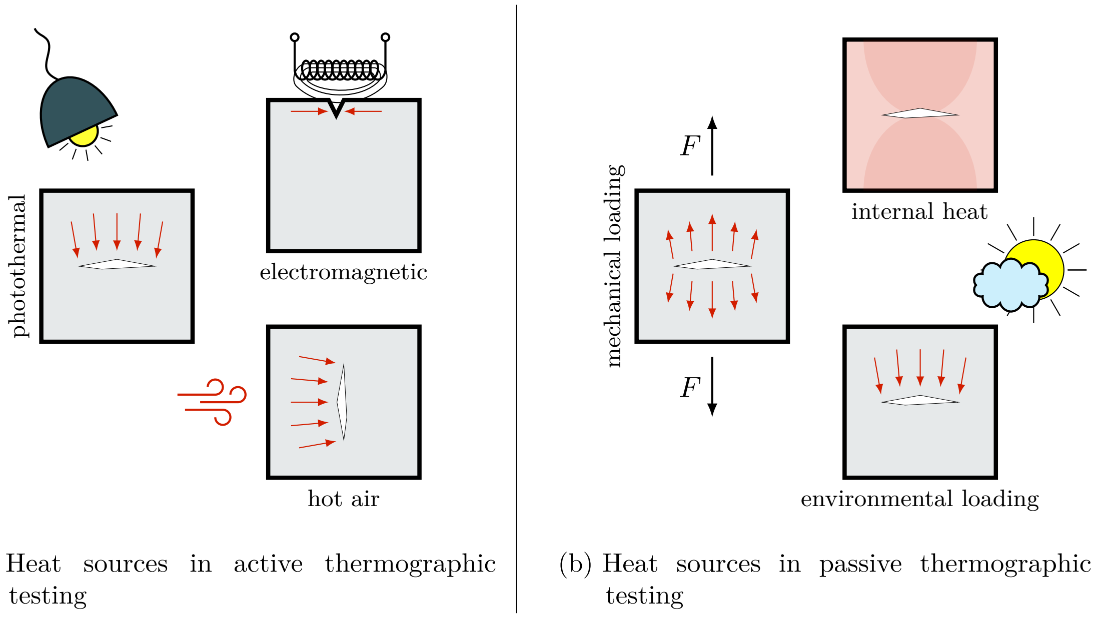

(a) Heat sources in active thermographic testing

(b) Heat sources in passive thermographic testing

Figure 2.5: Active and passive thermographic testing scenarios: while passive TT exploits excess internal heat or thermodynamic imbalance with the environment, active TT is characterized by deliberately inducing an instationary heat flow into the OuT. The red arrows indicate internal heat flow.

the presence of excess internal heat from a previous processing step or chemical process and when actively heating is impractical because of the OuT's size, active TT methods are much more common for component testing due to the higher degrees of freedom the user has to design the testing procedure. Furthermore, active TT allows for a more controlled heating regarding its area of effect and its temporal structure. The relevant standard DIN EN 17119:2018-10 (Tab. A.1) lists a wide variety of suitable heat sources, comprising hot air, eddy current and photothermal excitation methods using polychromatic and monochromatic light sources among others [20]. Polychromatic photothermal heat sources such as flash lamps and halogen lamps have seen heavy use in the past because they are rather inexpensive and easily available. Flash lamps also feature relatively high achievable optical irradiance values of up to $\lessapprox 100\,\mathrm{W/cm^2}$ at sufficiently small object distances at pulse durations of $t_{\mathrm{pulse}} \ll 5\,\mathrm{ms}$ [21, 22]. This combination of high irradiance at low pulse duration allows for a Dirac-pulse like heating, which is also beneficial for subsequent mathematical analysis due to the structure of the heat PDE (cf. Equation (2.16)). Their main disadvantage is that they themselves act as black body radiators at a high temperature and therefore also emit radiation in the same spectrum as the heated OuT. This is especially problematic directly after their activation due to those sources cooling back down to ambient temperature (afterglow effect). This radiation tends to further unwantedly photothermally heat up the OuT. Furthermore, it can also reflect off the OuT and thus, directly affects any radiometric temperature measurement [23]. In practice, the infrared part of the emitted spectrum needs to be filtered out using additional filters in front of the flash lamps. Additionally, due to them emitting polychromatically into a large angular space, focusing and other beamforming becomes a very complex task and is therefore impractical for most applications. This makes flash lamps mostly unsuitable for any testing methods that require spatially structured illumination.

Photothermal excitation using monochromatic laser or narrowband light emitting diode light sources on the other hand does not significantly affect any radiometric temperature measurement as long as the center wavelength is chosen sufficiently far away from the spectral band of the temperature measurement. Furthermore, with the advent of modern high-power laser systems, there is (almost) no limit to the achievable irradiance even at longer pulse durations [24]. The monochromatic and coherent nature of laser radiation allows for application of a wide variety of optical elements for beamforming and focusing. However, this comes at the cost of much higher efforts to be made for assuring operator safety when working with possibly dangerous radiation [25].

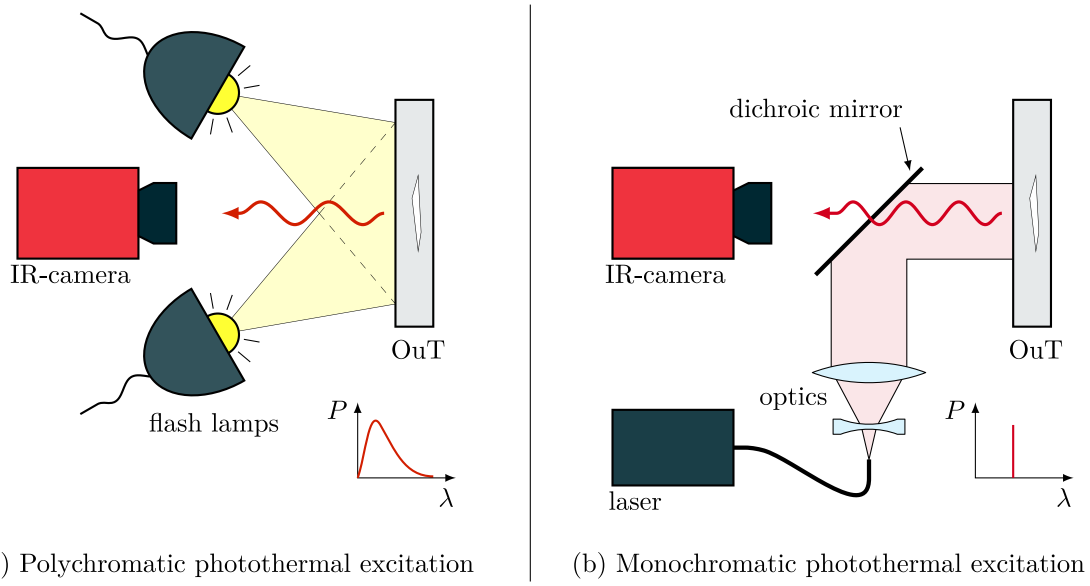

(a) Polychromatic photothermal excitation

(b) Monochromatic photothermal excitation

Figure 2.6: Schematic of a thermographic measurement setup using different types of photothermal excitation. While the use of polychromatic light sources (left; flash lamps, halogen lamps) is the more common and more traditional excitation method, the use of monochromatic laser light sources (right) enjoys increasing popularity due to a reduction in cost and technological advantages.

2.1.3 Measuring Temperature

Measuring temperature is foundational to any TT method. Depending on the requirements, this is either done point-wise or spatially resolved over a larger area. Temperature measurements can be further divided into contacting and contactless methods which are explored in more detail in the following subsections.

2.1.3.1 Contact Measurement

Temperature measurement with contacting sensors are widely used in temperature monitoring applications and offer high-precision measurements at comparably low-cost but are for the most part limited to measuring temperature at a single location. Modern contact thermometers are mostly restricted to exploit either the thermoelectric effect (thermocouple) or the temperature dependency of the electrical resistance of certain materials (resistance thermometer).

Thermocouple

The operating principle of the thermocouple is based on the Seebeck effect. This effect accounts for the fact that along a temperature gradient in a material also a gradient in its internal electrical field is induced, resulting in a measurable voltage across this gradient. This voltage is proportional to the material's Seebeck coefficient S [µV/K]. Since this voltage is very hard to measure alone, in practical applications the relative Seebeck effect over a material junction $A \to B$ with Seebeck coefficients S_A and S_B is determined instead:

$$\begin{aligned} U_{\text{thermo}} &= \int_{T_1}^{T_2} \left(S_B(T) - S_A(T)\right)\, \mathrm{d}T \\ &\approx k_{A\to B} \cdot (T_2 - T_1) \qquad \text{for small } T_2 - T_1 \end{aligned} \tag{2.20}$$

with thermoelectric coefficient $k_{A\to B} = S_B(T_1) - S_A(T_1)$. Typical material combinations used for thermocouples like NiCr → Ni (type K) feature a thermoelectric coefficient $k_{\text{NiCr}\to\text{Ni}} = 39\,\mu\text{V/K}$ [26].

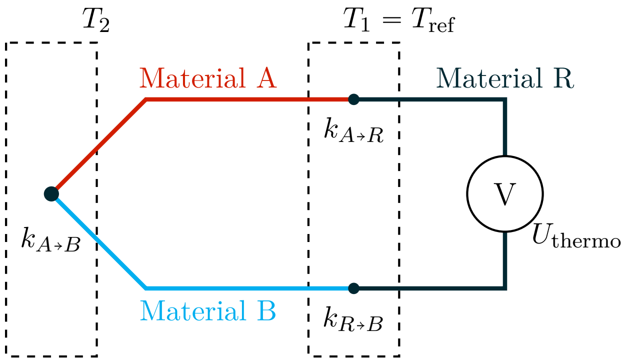

Figure 2.7: Scheme of a temperature measurement using a thermocouple: while T_2 is to be determined, the temperature T_1 at the junction to the voltage measurement has to be precisely known.

When measuring the voltage across the thermocouple, another material transition between the thermocouple constituent materials and the voltage measurement device is inevitably introduced, causing an additional thermoelectric gradient which influences the measurement. In order to compensate for this influence of the additionally introduced material R, the voltage measurement junctions have to be kept at the same temperature T_1:

$$U_{\text{thermo}} = k_{A\to B} \cdot T_2 - k_{A\to R} \cdot T_1 - k_{R\to B} \cdot T_1 = k_{A\to B} \cdot (T_2 - T_1) \ , \tag{2.21}$$

where the contribution of the material junctions $A \to R$ and $R \to B$ introduced by the voltage measurement cancels out as follows:

$$\begin{aligned} -k_{A\to R} - k_{R\to B} &= -S_R(T_1) + S_A(T_1) - S_B(T_1) + S_R(T_1) \\ &= -\left[S_B\left(T_1\right) - S_A\left(T_1\right)\right] = -k_{A\to B} \ . \end{aligned} \tag{2.22}$$

For absolute temperature measurements, the reference temperature T_1 must be known in order to determine the temperature T_2. This could be done by either exposing the material junction to the voltage measurement to a well-know stable temperature ("ice bath" method) or measure T_1 continuously as well and correct for it. Even though this approach adds another temperature measurement to the method, this measurement can be carried out far away from the actual measurement position in a more protected environment using other temperature sensing methods like a semi-conductor based sensor or a resistance thermometer.

Resistance thermometer

Resistance thermometers or resistance temperature detectors (RTDs) measure temperature by determining the absolute value of a resistance with a known temperature dependence. Depending on whether the resistance increases or decreases with increasing temperature, RTDs are differentiated between RTDs with positive temperature coefficient (PTC) and negative temperature coefficient. A typical temperature measurement scheme using a RTD is shown in Figure 2.8. Here, the absolute value of the RTD's resistance is measured applying a small current I_{meas} and simultaneously measuring the voltage drop U_{meas} over the RTD. Any current flowing through the RTD will cause self-heating, which will negatively affect the temperature measurement. Thus, I_{meas} has to be kept small and ideally only intermittently applied during the acquisition of a single temperature measurement. The resistance value can be determined using Ohm's law:

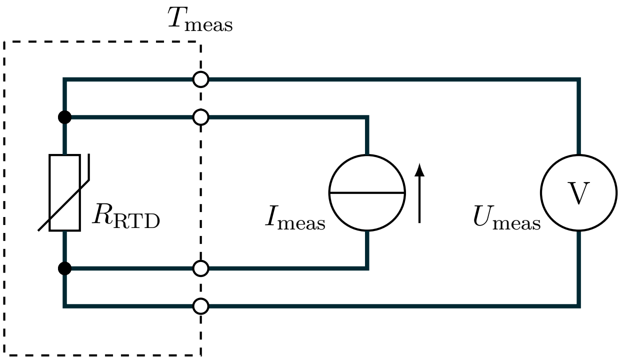

Figure 2.8: Resistance thermometer measurement scheme: the absolute value of a resistor with known temperature dependence is measured by exposing it to a small electrical current while simultaneously measuring the voltage drop over the resistance. Using Ohm's law and the known temperature dependence relationship, the temperature T_{meas} can be determined.

$$R_{\text{RTD}} = \frac{U_{\text{meas}}}{I_{\text{meas}}} . \tag{2.23}$$

Finally, if the current RTD's resistance has been determined, the temperature of the RTD can be calculated using its known temperature dependence:

$$R_{\mathrm{RTD}}(T) = R(T_{\mathrm{ref}}) \cdot \left[1 + A \cdot (T - T_{\mathrm{ref}}) + B \cdot (T - T_{\mathrm{ref}})^2\right] \ , \tag{2.24}$$

with A $[\mathrm{K}^{-1}]$ and B $[\mathrm{K}^{-2}]$ resembling the known temperature characteristics values for the resistor material (second-order approximation) and $R(T_{\mathrm{ref}})$ a known resistance value at $T = T_{\mathrm{ref}}$. A representative example of a RTD-material with PTC characteristics would be platinum, which is very widely applied due to its high linearity and robustness. In the range of $0\,^\circ\mathrm{C}$ to $100\,^\circ\mathrm{C}$, platinum features a linear temperature coefficient of $A = 3.9083 \cdot 10^{-3}\,\mathrm{K}^{-1}$ with commonly available values for $R(T_{\mathrm{ref}} = 0\,^\circ\mathrm{C}) \in \{100\,\Omega,\ 500\,\Omega,\ 1000\,\Omega\}$ [27].

2.1.3.2 Radiometric Measurement

In addition to the widely used contact measurement of an object's temperature, there is a whole family of non-contact measurement methods based on radiometric principles. The following section introduces the radiometric measurement principle, describes different types of detectors and finally relates it to the measurement of an object's true temperature.

According to the Stefan-Boltzmann law, every body that possesses a temperature above $T > 0\,\mathrm{K}$ emits electromagnetic radiation. The total spectral integrated radiated power $P(T)$ $[\mathrm{W}]$ is then proportional to the temperature of the body to the fourth power:

$$P(T) = \varepsilon \cdot \sigma \cdot A \cdot T^4 \ , \tag{2.25}$$

where ε is the emissivity of the body, A its surface area and $\sigma = 5.670\,374\,419 \cdot 10^{-8}\,\mathrm{W/(m^2\,K^4)}$ is the Stefan-Boltzmann constant. The emissivity $\varepsilon \in\,]0, 1]$ is a measure of the body's resemblance of an ideal black body radiator. An ideal black body ($\varepsilon = 1$) is a physical object that absorbs all incoming radiation independent of the incidence angle ($\rightarrow$ absorptivity $\alpha = 1$) and emits the maximum amount of thermal radiative energy possible for its temperature T. Since the emission of thermal energy for opaque materials is mediated by the object's surface, the effective emissivity is also dependent on the surface's overall condition (roughness, flatness, cleanliness). While the emissivity is in general also dependent on the temperature T, the angle to the surface normal at which it is observed and the specific wavelength of the emitted radiation λ, this effect will be left out of consideration within the scope of this work due to the small changes in temperature necessary for thermographic testing.

The spectrum of the emitted radiation has been first famously described by Max Planck in the year 1900 when he found the following expression for the contribution of each wavelength range $\mathrm{d}\lambda$ to the spectral radiance $L_\lambda(\lambda, T)$ $\left[\mathrm{W/(sr\,m^2\,\mu m)}\right]$ of a surface element $\mathrm{d}A$ of a body at temperature T into the space spanned by the solid angle element $\mathrm{d}\Omega$ [28]:

$$L_\lambda(\lambda, T)\,\mathrm{d}A\,\mathrm{d}\lambda\,\mathrm{d}\Omega = \frac{2hc^2}{\lambda^5}\frac{1}{\mathrm{e}^{hc/\lambda k_b T} - 1}\,\mathrm{d}A\,\mathrm{d}\lambda\,\mathrm{d}\Omega\ , \tag{2.26}$$

where $h = 6.626\,070\,15 \cdot 10^{-34}\,\mathrm{J/Hz}$ is the Planck constant, $c = 2.997\,924\,58 \cdot 10^{8}\,\mathrm{m/s}$ is the speed of light in vacuum and $k_b = 1.380\,649 \cdot 10^{-23}\,\mathrm{J/K}$ is the Boltzmann constant. The spectrum of a black body radiator as defined by Equation (2.26) is shown in Figure 2.9. Here, it can be clearly seen that the maximum of the spectral radiance is shifted towards smaller wavelengths and also the total integrated power drastically increases for higher temperature as already predicted by Equation (2.25). The location λ_{peak} of the maximum of the spectral radiance can be deduced using Wien's displacement law, which states that the product of temperature and the wavelength multiplies to a constant value for black body radiators [29]. For the $\lambda_{\mathrm{peak}}(T)$ this evaluates to:

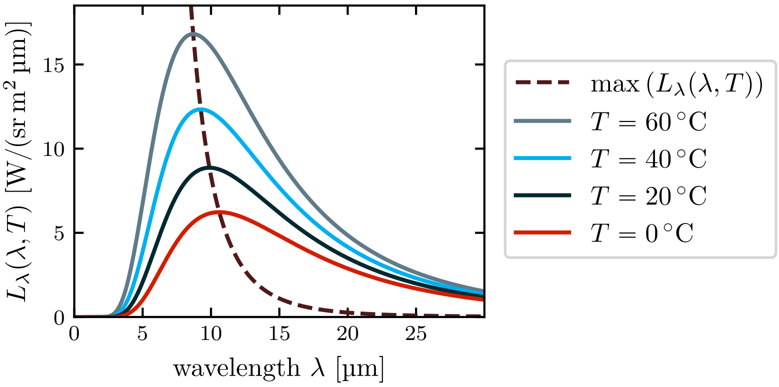

Figure 2.9: Spectral radiance $L_\lambda(\lambda, T)$ of a black body radiator for temperatures close to room temperature. The maximum of the spectral radiance curve for each temperature T can be determined using Wien's displacement law (cf. Equation (2.27)).

$$\begin{aligned} \lambda_{\mathrm{peak}}(T) &= \frac{b_{\mathrm{peak}}}{T} && \text{, with} \\ b_{\mathrm{peak}} &= \frac{hc}{\left[5 + W_0\left(-5\,\mathrm{e}^{-5}\right)\right] \cdot k_b} \approx 2897.8\,\mathrm{µm\,K} && , \end{aligned} \tag{2.27}$$

where W_0 is the Lambert W function [30]. With the use of Equation (2.26) the radiated spectral power per solid angle of a surface element $\mathrm{d}A$ of a black body radiator can be determined.

Since a black body by definition is a perfectly diffusely reflecting and absorbing surface, its radiative behavior obeys Lambert's emission law, which states that the irradiated power has to decrease with the cosine of the viewing angle against the normal of a surface in order to achieve constant luminance over all viewing angles [31, p. 117]. The spectral intensity I_θ [W/(sr nm)] of a black body at a viewing angle θ against the surface normal can thus be calculated as follows:

$$I_\theta(\lambda, T) = \int\limits_A L_\lambda(\lambda, T) \cos\theta \, \mathrm{d}A \; . \tag{2.28}$$

The spectral flux Φ_λ [W/nm] emitted by the surface A into the angular space S can then be determined by integration: Spectral flux :

$$\Phi_\lambda(T) = \iint\limits_S I_\theta(\lambda, T) \, \mathrm{d}\Omega = \iint\limits_S \int\limits_A L_\lambda(\lambda, T) \cos\theta \, \mathrm{d}\Omega \mathrm{d}A \; . \tag{2.29}$$

If S uniformly covers the whole half space, then the Stefan-Boltzmann law (cf. Equation (2.25)) for determining the total radiated power $P(T)$ of the surface A can be acquired by further integrating over all wavelengths $\lambda\Big|_0^\infty$. Since all bodies are constantly exchanging thermal energy with their surroundings via radiative transfer, the individual spectral flux Φ_λ of a singular body is less of interest than the transferred radiated heat flow $\dot{Q}_{1\to2}$ [W] between surfaces A_1 and A_2 with corresponding emissivities and temperatures $\varepsilon_1,\ T_1$ and $\varepsilon_2,\ T_2$:

$$\dot{Q}_{1\to2}(T_1, T_2) = \int\limits_{\lambda_\mathrm{min}}^{\lambda_\mathrm{max}} \varepsilon_1 \cdot F_{1\to2} \cdot \Phi_{\lambda,A_1}(T_1) - \varepsilon_2 \cdot F_{2\to1} \cdot \Phi_{\lambda,A_2}(T_2) \, \mathrm{d}\lambda \; , \tag{2.30}$$

where $F_{1\to2}$ is the view factor between surfaces A_1 and A_2. A schematic representation of two surfaces in thermal radiative contact for the special case of a warm surface to be measured by a detector is shown in Figure 2.10. The view factor $F_{1\to2}$ between surfaces A_1 and A_2 incorporates the relative sizes, distance and orientation of the surfaces between another, as this is relevant

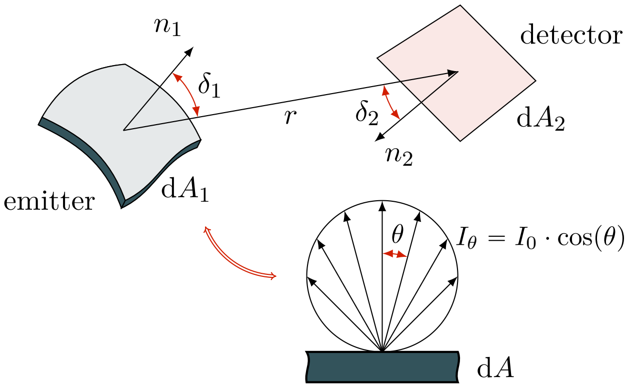

Figure 2.10: Lambertian surface $\mathrm{d}A_1$ emitting thermal radiation onto a detector $\mathrm{d}A_2$ positioned at a distance r. The radiated spectral intensity of the emitter can be described by the Lambert cosine law, as stated in Equation (2.28). The transferred radiated energy can be calculated according to Equation (2.30).

due to the viewing angle dependency of thermal radiation. It can be calculated as follows:

$$F_{1\rightarrow 2} = \frac{1}{A_1} \int\limits_{A_1} \int\limits_{A_2} \frac{\cos(\delta_1)\cos(\delta_2)}{\pi r^2} \, \mathrm{d}A_2 \, \mathrm{d}A_1 \ . \tag{2.31}$$

While view factors are strictly directional, the following equality holds true:

$$A_1 \cdot F_{1\rightarrow 2} = A_2 \cdot F_{2\rightarrow 1} \ , \tag{2.32}$$

which leads to the inverse view factor $F_{2\rightarrow 1}$ by rearranging as follows:

$$F_{2\rightarrow 1} = \frac{A_1}{A_2} \cdot F_{1\rightarrow 2} \ . \tag{2.33}$$

If now the temperature of one surface (i.e., A_2) is known as well as the orientation and surface properties of both surfaces, then the temperature of surface A_1 can be inferred by measuring the radiative heat flow between both surfaces.

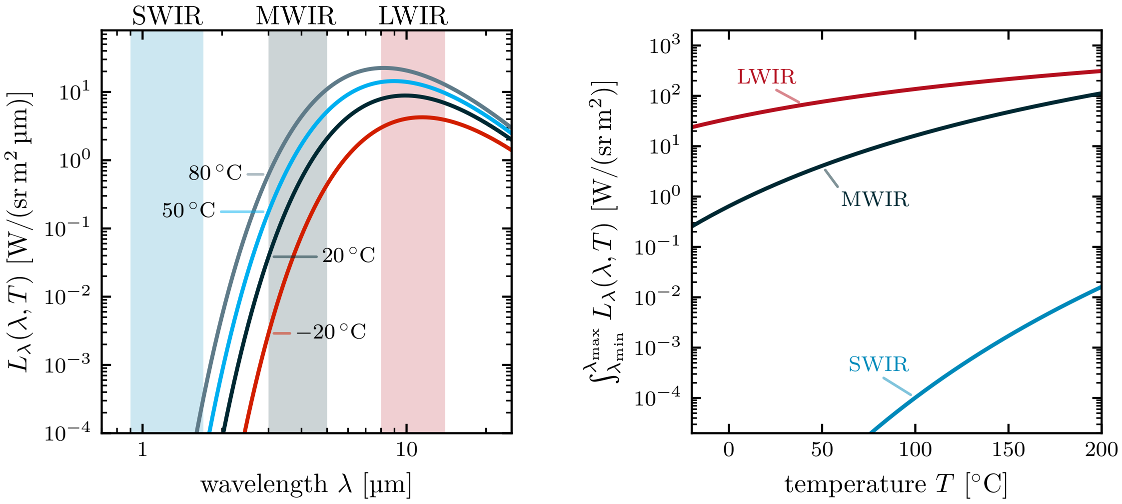

(a) Spectral radiance of black body radiators at different temperatures with indicated frequency bands.

(b) Integrated spectral radiance in different frequency bands over black body temperature.

Figure 2.11: Influence of the spectral sensitivity band of a radiometric detector. Common radiometric detectors only cover certain frequency bands. Common bands comprise the SWIR (0.9 – 1.7 µm), MWIR (3 – 5 µm) and the LWIR (8 – 14 µm) regions (left). Depending on the apparent temperature to be measured, the resulting measurement sensitivity and SNR is highly dependent on the spectral band covered by the measurement (right).

Inverting the relationship $\dot{Q} \propto \int_{\lambda_{\min}}^{\lambda_{\max}} \Phi_\lambda(T)$ for the temperature T lays the foundation to the radiometric measurement of temperature. Special attention must be paid to the spectral response of the detector in use, since the sensitivity and possible measurement ranges of the method are greatly influenced by the specific spectral band $[\lambda_{\text{min}}, \lambda_{\text{max}}]$ the detector is sensitive in, as is shown in Figure 2.11.

Evaluating the radiated heat flow from an OuT is the main working principle for all pyrometers (non-contact thermometers measuring radiant heat flow). One common manifestation of a pyrometer is the bolometer. A single bolometer cell consists of a weakly thermally coupled well-known thermal mass, which is exposed to the radiant heat flow, as described in Equation (2.30). The resulting change in temperature of the thermal mass ΔT_{Bolo} during the exposure time t_{int} can now be measured by an RTD or thermocouple and can subsequently be used to quantify the incoming heat flow $\dot{Q}(T_{\text{bolo}}, T_{\text{meas}})$ and therefore the temperature T_{meas} of the OuT via the following relation:

$$\Delta T_{\text{Bolo}} = \int_0^{t_{\text{int}}} \frac{\dot{Q}(T_{\text{Bolo}}, T_{\text{meas}}, t)}{c_p \cdot \rho \cdot V_{\text{bolo}}} \, \mathrm{d}t \ , \tag{2.34}$$

where $c_p \cdot \rho$ is the specific thermal mass of the bolometer material, V_{bolo} its volume and $\Delta T_{\text{Bolo}} = T_{\text{Bolo}} - T_0$, with T_0 being the starting temperature before the measurement. After each measurement, the thermal mass has to be allowed to relax back to T_0 via the weak thermal connection to the bolometer body (heat sink), which significantly limits the achievable acquisition frequency. A schematic view of a bolometer cell is shown in Figure 2.12.

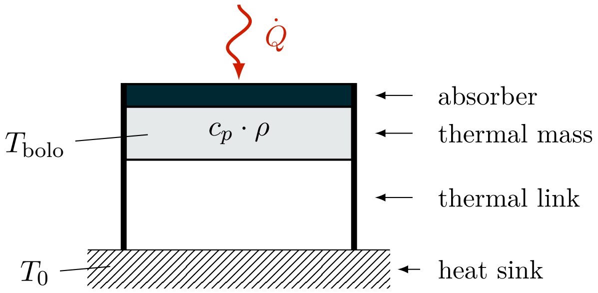

Figure 2.12: Schematic structure of a bolometer: incoming radiative flux is absorbed by a decoupled known thermal mass. With the increase of T_{bolo} of the thermal mass during a fixed integration time t_{int} the incoming radiated heat flow $\dot{Q}$ can be determined using Equation (2.34). After each integration time the thermal mass relaxes its temperature back to T_0 via the thermal link to the heat sink. This substantially limits the achievable acquisition rate.

Another widely used technique to contactlessly measuring temperature is to directly measure the emitted thermal radiation photons using modern charge-coupled device (CCD) or complementary metal-oxide-semiconductor (CMOS)-based detectors. Here, incoming photons charge up the individual pixels over a predefined exposure time, generating a small voltage/current that can be subsequently read out to determine the overall amount of photons that hit the individual pixel. Since the photon flux is proportional to the spectral radiance

$L_q(\lambda, T) = \frac{L_\lambda(\lambda,T)\cdot\lambda}{h\cdot c}$, it is also a direct measure of the temperature of any (gray) body. Because those detectors generally feature a rather low pixel size and high acquisition rates, they are commonly used in present day infrared cameras. CCD and CMOS-based detectors inherently suffer from dark currents even if no signal is present, which offsets the current measurements. Even though the influence of the mean dark current per pixel can be measured and corrected (dark frame correction), its stochastic behavior leads to significant measurement errors when measuring small temperatures (absolute error) or small temperature differentials (relative error). Since the dark current is itself temperature dependent, high-precision infrared cameras feature a cooled detector element, which is cooled down by a cryogenic cooler to temperatures as low as 75 K to 80 K. While this leads to achievable noise equivalent temperature difference (NETD) values of $\leqslant 50\,\mathrm{mK}$, the addition of a cooling element also severely impacts cost and longevity of the camera system, as the cryogenic coolers only feature an operative lifetime of about $\approx 10\,000\,\mathrm{h}$.

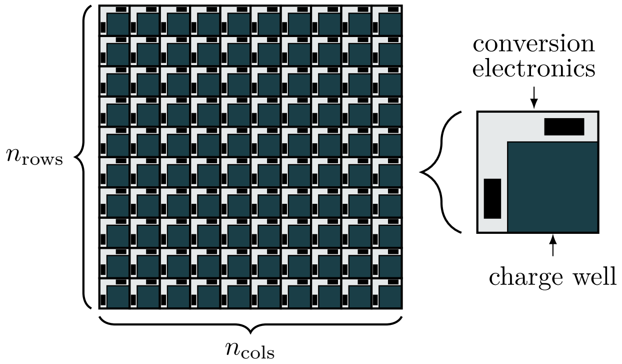

Figure 2.13: Schematic of a CMOS-based detector: each pixel consists of a photoactive semiconductor material converting incoming photons into a small charge. The charge is accumulated for the integration period and subsequently read out via dedicated electronics situated next to each pixel and cleared afterwards. Compared to CCD-detectors, the integrated electronics per pixel allow reading out the pixel values in arbitrary order.

To convert the digital values of a CCD or CMOS based detector measuring the thermal radiated power into true temperature values, several factors need to be taken into account, including the detector's quantum efficiency, its temperature and the temperatures of any object in the path of the measurement. All those parameters are inputted into a mathematical model of the detector's response and the detector is calibrated against radiative references of known emissivity for different temperature. With this calibration process a chart similar to the one presented in Figure 2.11 (b) can be obtained, which, when inverted, directly describes the relationship between measured digital values and the OuT's temperature.

2.1.4 Processing of Active Thermographic Data

While thermographic measurement data can already be interpreted as-is, a sequence of thermographic images in an active TT scenario most often contains a lot more information about the internals of the OuT than is directly accessible in the raw temperature data. As the widespread use of thermographic measurements still mostly relies on the evaluation of a human trained expert and due to the ease of use of applying a homogeneous pulsed illumination to the OuT, conventional post-processing focuses on further increasing the defect contrasts in thermographic images for such homogeneous illumination conditions. Foundational to all hereinafter presented methods is the simplified solution for the one-dimensional heat PDE for a Dirac-like heat pulse acting uniformly over the full front surface ($z = 0$) with area A of a semi-infinite body, which is given as follows [32, p. 53]:

$$T(z,t) = \frac{\dot{Q}/A}{2\rho c_p \sqrt{\alpha \pi t}} \exp\left(-\frac{z^2}{4\alpha t}\right) + T_0 \ , \tag{2.35}$$

where $\dot{Q}$ is the absorbed heat flow and T_0 is the initial temperature of the body at $t = 0\,\mathrm{s}$. Since it is not viable to radiatively measure temperatures inside the body for opaque materials, mostly only the front surface ($z = 0$) is accessible for measurement. Therefore, Equation (2.36) can be reduced as follows:

$$T(z=0,t) = T(t) = \frac{\dot{Q}/A}{2\rho c_p \sqrt{\alpha \pi t}} + T_0 \ . \tag{2.36}$$

Difference Thermography (DT)

One of the easiest ways to increase the defect contrasts is to subtract the mean signal of a known sound sub-area of the ROI or from a golden reference part as follows:

$$T_{DT}(x,y,t) = T(x,y,t) - \sum_{i=1}^{n_{x,sound}} \sum_{j=1}^{n_{y,sound}} \frac{T(i \cdot \Delta x + x_{\mathrm{sound}},\, j \cdot \Delta y + y_{\mathrm{sound}},\, t)}{n_x \cdot n_y} \ , \tag{2.37}$$

where $\Delta x, \Delta y$ is the spatial sampling rate of the measurement, while a sound sub-area within the ROI anchored at $(x_{\mathrm{sound}}, y_{\mathrm{sound}})$ spanning $n_{x,sound}$ pixel in the x-direction and $n_{y,sound}$ pixel in the y-direction is known. Subtracting a known sound area results in a dataset where all sound areas can be identified by a simple thresholding operation. All areas can be considered sound for which $|T_{DT}(x,y,t)| < |\mathcal{N}_{\mathrm{noise}}|$, where $\mathcal{N}_{\mathrm{noise}}$ is the remaining measurement noise. Therefore, this step eliminates all background signals and leaves the operator evaluating the results with a clear indication of defective regions. However, for the method to work, it is necessary to have a known sound region or sound reference part available, both of which must be representative in material and geometry of the ROI/OuT and most likely require another nondestructive testing (NDT)-method to characterize and validate before being used as a reference.

Thermal Signal Reconstruction Method

The thermal signal reconstruction (TSR) method is based on fitting the acquired temperature data to a polynomial of degree n_degree in log-log space [33]:

$$\log(T_\text{diff}) = \sum_{n=0}^{n_\text{degree}} a_n \cdot \log(t)^n \qquad \text{, with} \tag{2.38}$$

$$T_\text{diff}(x,y,t) = T(x,y,t) - T_0(x,y) \ . \tag{2.39}$$

If the one-dimensional solution to the heat PDE for a Dirac-like heating (cf. Equation (2.36)) is fitted in double logarithmic scale with a polynomial as defined in Equation (2.38), the following exact solution is obtained:

$$\log(T_\text{diff,pristine}) = \log\left(\frac{\dot{Q}/A}{2\rho c_p\sqrt{\alpha\pi}}\right) - \frac{1}{2}\log(t) = \log(\text{const.}) - \frac{1}{2}\log(t) \tag{2.40}$$

$$\Rightarrow \qquad a = \{\log(\text{const.})\,,\ -1/2,\ 0,\ \dots,\ 0\}\ , \tag{2.41}$$

which resembles a straight line with slope $a_1 = -1/2$ when plotted on a log-log scale. This behavior can be directly observed in Figure 2.14 where the temperature evolution according to Equation (2.36) is shown on a log-log scale. Any deviation from this straight line behavior clearly indicates that additional effusivity contrasts (i.e., defects) are present. As effusivity boundaries show up as knee points in the log-log plot, the depth of the boundary can be determined via its corresponding diffusion length (cf. Equation (2.13)).

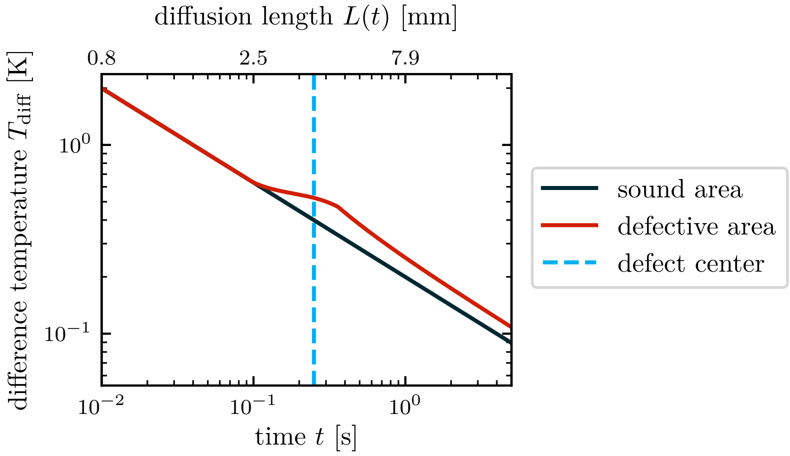

Figure 2.14: Temperature evolution after a Dirac-like heating with one-dimensional heat flow. When plotted on a double logarithmic scale (log-log), the temperature of a sound area follows a straight line with slope $\frac{\mathrm{d}\log(T_\text{diff})}{\mathrm{d}\log(t)} = -1/2$. Defective areas can be clearly distinguished by deviating from this behavior. Effusivity contrasts show up as knees whose positions indicate their depth.

For testing larger ROIs, the temperature evolution $T_{\text{diff}}(x, y, t)$ of every pixel $(i \cdot \Delta x,\ j \cdot \Delta y)$ for $i \in \{1, \ldots, n_x\}$, $j \in \{1, \ldots, n_y\}$ can be fitted with a polynomial in log-log space and the coefficients $a_n(x, y)$ can be plotted as an image. With this imaging approach it is also possible to map out different defect structures [34].

Pulsed Phase Thermography

The pulsed phase thermography (PPT) evaluation method for thermal data makes use of the frequency content of the data [35]. The nth contained frequency T^n_{fft} in the temperature data $T(x, y, t)$ is obtained after applying a discrete Fourier transform (DFT). This can be computationally efficiently implemented using the fast Fourier transform (FFT) to calculate the DFT defined as follows:

$$T^n_{\text{fft}}(x, y) = \Delta t \sum_{l=0}^{n_t-1} T(x, y, l \cdot \Delta t) \exp\left(-2i\pi nl/n_t\right) = \text{Re}^n_{\text{fft}} + i \cdot \text{Im}^n_{\text{fft}} \ , \tag{2.42}$$

where $i = \sqrt{-1}$ is the imaginary unit, n_t is the number of samples in time and Δt the sampling interval. $T^n_{\text{fft}}(x, y) \in \mathbb{C}$ is a complex number whose real part is $\text{Re}^n_{\text{fft}}(x, y) \in \mathbb{R}$ and its imaginary part is $\text{Im}^n_{\text{fft}}(x, y) \in \mathbb{R}$. With the thermal data now transformed into frequency space, amplitude $A^n_{\text{fft}}(x, y)$ and phase $\phi^n_{\text{fft}}(x, y)$ images can be generated as follows:

$$A^n_{\text{fft}}(x, y) = \sqrt{\text{Re}^n_{\text{fft}}(x, y)^2 + \text{Im}^n_{\text{fft}}(x, y)^2} \tag{2.43}$$

$$\phi^n_{\text{fft}}(x, y) = \arg\left(T^n_{\text{fft}}(x, y)\right) \ . \tag{2.44}$$

The resulting amplitude and phase images can now be examined for irregularities hinting towards the presence of a defect. While phase images generally show a deeper probing capability than amplitude data, they are also much more prone to noise. In order to further improve the defect contrast, there is also the possibility to combine this method with difference thermography by directly looking at amplitude and phase contrasts with respect to a known sound subarea [36]:

$$\Delta A^n_{\text{fft}}(x, y) = A^n_{\text{fft}}(x, y) - \sum_{i=1}^{n_{x,sound}} \sum_{j=1}^{n_{y,sound}} A^n_{\text{fft}}(i \cdot \Delta x + x_{\text{sound}}, j \cdot \Delta y + y_{\text{sound}}) \tag{2.45}$$

$$\Delta \phi^n_{\text{fft}}(x, y) = \phi^n_{\text{fft}}(x, y) - \sum_{i=1}^{n_{x,sound}} \sum_{j=1}^{n_{y,sound}} \phi^n_{\text{fft}}(i \cdot \Delta x + x_{\text{sound}}, j \cdot \Delta y + y_{\text{sound}}) \tag{2.46}$$

Additionally, a depth-estimate L^n_{fft} of the observed defects can be generated by looking at the frequency component n at which they have been observed [37, 38]:

$$L^n_{\text{fft}} = \sqrt{\frac{2 \cdot \alpha}{2\pi \cdot n \cdot \Delta f}} \ , \tag{2.47}$$

where the frequency resolution of the measurement is defined as $\Delta f = \frac{1}{n_t \cdot \Delta t}$.

2.2 Defect Resolution in Thermographic Testing

In the field of NDT, the first major step is to detect if there are any defects present. Depending on the method used, this will not necessarily directly yield also sufficient information about the size and shape of the defect, which is necessary to assess its impact with regard to the specifications the OuT has to meet. When an imaging method (as common in TT) is used, the resolution of the defect is bound by the point spread function (PSF) of the measurement setup. The PSF is a concept borrowed from the field of optics and describes the response of the measurement setup to a point-like object (point source). As it is a measure of the system's transmission characteristics, it affects any original undisturbed defect signal I_{original} as follows:

$$I_{\text{transmitted}}(r) = I_{\text{original}}(r) *_r \Phi_{\text{PSF}}(r) \ . \tag{2.48}$$

Here, the transmitted signal $I_{\text{transmitted}}$ is essentially a spatial frequency filtered version of I_{original} due to the convolution operation involved. This can be clearly seen when transforming Equation (2.48) into spatial frequency domain using the Fourier transform:

$$\mathcal{F}\left[I_{\text{transmitted}}\right](\zeta_r) = \mathcal{F}\left[I_{\text{original}}\right](\zeta_r) \cdot \mathcal{F}\left[\Phi_{\text{PSF}}\right](\zeta_r) \ , \tag{2.49}$$

where $\mathcal{F} : \mathbb{R} \to \mathbb{C}$ denotes the Fourier transform that transforms the spatial coordinate r into a spatial frequency ζ_r. The behavior of the filter is completely determined by the spatial frequency content of the PSF, which is multiplied by the frequency content of the original signal. The amplitude spectrum of the frequency content of the PSF is therefore of particular interest. In optics, the Fourier transform of the PSF is called the optical transfer function. Its constituent parts are called the modulation transfer function (MTF) for the amplitude spectrum and phase transfer function for the phase spectrum:

$$\mathcal{F}\left[\Phi_{\text{PSF}}\right](\zeta_r) = \text{OTF}(\zeta_r) = \text{MTF}(\zeta_r) \cdot \exp\left(i\,\text{PhTF}(\zeta_r)\right) \tag{2.50}$$

$$\Rightarrow \qquad \text{MTF}(\zeta_r) = \left|\mathcal{F}\left[\Phi_{\text{PSF}}\right](\zeta_r)\right| \ . \tag{2.51}$$

By convention, the MTF is always shown normalized such that $\text{MTF}(\zeta_r = 0) = 1$.

If the PSF of the measurement setup is known, then also a statement can be made about the total resolution capabilities of the system. As an active TT measurement setup consists of multiple elements that influence the achievable resolution, every element has to be addressed independently. An overview of the elements influencing the achievable resolution of an active TT measurement is shown in Figure 2.15.

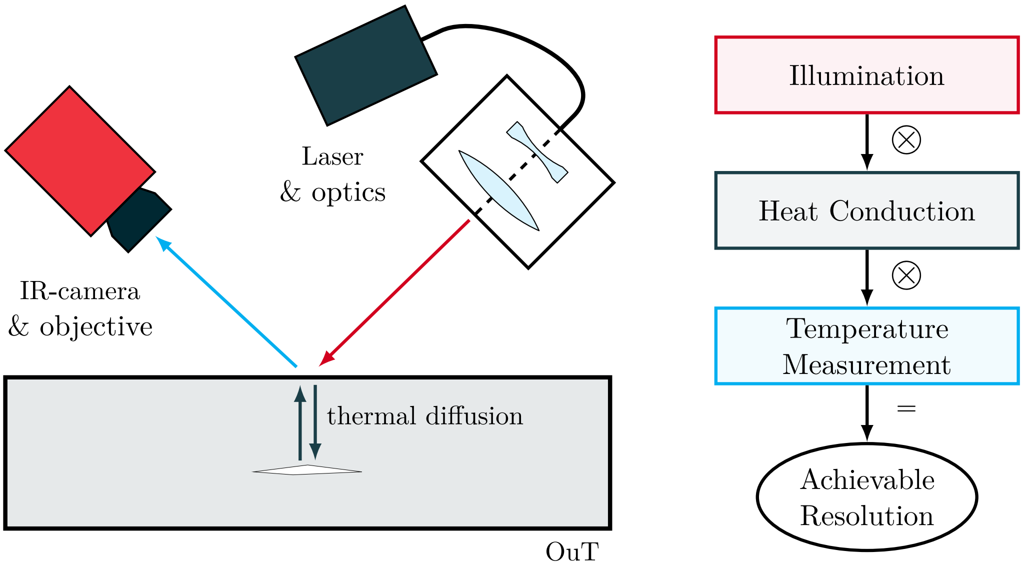

Figure 2.15: Impact factors on the resolution of internal defects using active thermographic testing. The achievable resolution of an active TT measurement is bound by the combined spatial resolution of its individual parts. These can be grouped into the effects of the illumination (cf. Section 2.2.3), the effects of the thermal diffusion (cf. Section 2.2.2) and the effects of the temperature measurement (cf. Section 2.2.1).

Combining multiple MTFs in order to get the transmission characteristics of the whole setup $\mathrm{MTF}_{\mathrm{total}}$ is then achieved using the product of all constituent MTFs represented as $\mathrm{MTF}_{\mathrm{i}}$:

$$\mathrm{MTF}_{\mathrm{total}}(\zeta_r) = \prod_i \mathrm{MTF}_{\mathrm{i}}(\zeta_r) \ . \tag{2.52}$$

Due to the multiplicativity of the MTF, it can be observed that the resolution limit of any system is mainly limited by its worst performing component.

2.2.1 Spatial Resolution of the Temperature Measurement

As within TT a spatially resolved temperature measurement is commonly achieved using an infrared (IR)-camera, the spatial resolution capabilities of the temperature measurement is governed by the MTF of this camera. Since an IR-camera resembles a typical optical imaging system, its MTF is mainly composed of the performance of the detector used, and the objective employed for imaging the OuT. For an ideal lens, the transmission limit of spatial frequencies ζ_0 is given by the Sparrow criterion as follows [39]:

$$\zeta_0 \approx \frac{1}{0.94\lambda \cdot f_\#} \ , \tag{2.53}$$

where the f-number $f_{\#}$ is the quotient between the aperture diameter of the lens D_{optics} and its focal length f_{focal}:

$$f_{\#} = \frac{f_{\text{focal}}}{D_{\text{optics}}} \; . \tag{2.54}$$

As the f-number is (almost) always greater or equal to one, the maximal cut-off frequency will be bound by approximately half of the wavelength λ used for imaging for all practical circumstances.

The Sparrow criterion states that two structures can only be resolved as independent if they are so far apart that their PSFs overlap only enough to leave an observable minimum between them. This criterion is widely used to evaluate the performance of optical systems and is less conservative than the well-known Rayleigh criterion:

$$\zeta_{0,\text{Rayleigh}} \approx \frac{1}{1.22\lambda \cdot f_{\#}} \; , \tag{2.55}$$

which requires that the overlapping PSFs be no closer together than the distance to their first zero. The transmission behavior for frequencies lower than ζ_0 for an ideal lens is given by the following equation [40, p. 121: Eq. 4.10-4.11]:

$$\begin{aligned} \text{MTF}(\zeta_r) &= \frac{2}{\pi}\left|\left(\gamma - \cos(\gamma)\sin(\gamma)\right)\right| && \text{, with} \\ \gamma &= \cos^{-1}\left(\frac{\zeta_r}{\zeta_0}\right) \; , && 0 \leqslant \zeta_r \leqslant \zeta_0 \; . \end{aligned} \tag{2.56}$$

As the cut-off frequency ζ_0 is mainly dependent on the refractive power and diameter of the lens as encoded in the f-number, the overall frequency transmission behavior of the lens is also strongly affected by these factors, as can be seen in Figure 2.16. Even though smaller f-numbers are desirable, those smaller f-number systems are also more prone to optical aberration and distortion influencing the MTF negatively.

In addition to the optical imaging system, the MTF of the IR-camera $\text{MTF}_{\text{camera}}$ is also limited by the MTF of the detector in use $\text{MTF}_{\text{detector}}$:

$$\text{MTF}_{\text{camera}}(\zeta_r) = \text{MTF}_{\text{optics}}(\zeta_r) \cdot \text{MTF}_{\text{detector}}(\zeta_r) \; . \tag{2.57}$$

This circumstance is caused by the fact that every pixel of the detector features only a limited size and therefore also a limited capability of perceiving spatial frequency. As every pixel of the detector can be imagined as a small aperture, the $\text{MTF}_{\text{detector}}$ can be calculated as the Fourier transform of its pixel's aperture function (e.g., a 2D-rectangular function for rectangular pixels) [41]. Since the MTF of apertures is also foundational to the MTF of the illumination, a detailed examination is presented in Section 2.2.3.

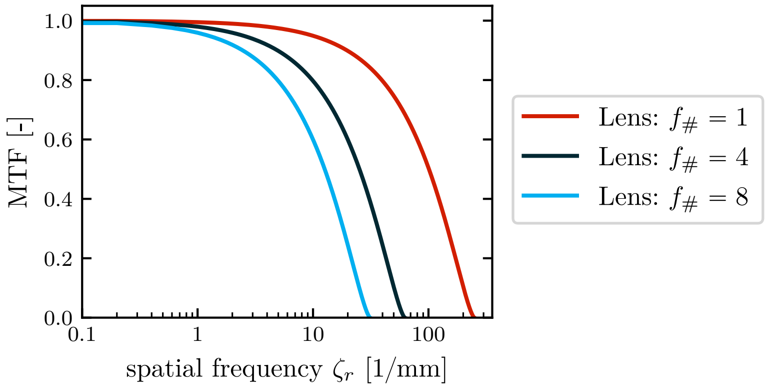

Figure 2.16: MTF of an ideal lens for different f-numbers: with increasing f-number (decreasing refractive power and smaller aperture size) the transmission limit decreases towards lower spatial frequencies lowering the total achievable spatial resolution. All MTFs are calculated for a representative wavelength of $\lambda = 4\,\mu\text{m}$.

2.2.2 Spatial Resolution Limit of Thermal Diffusion

The thermal PSF can be derived from the Green's function solution to the heat PDE for a suitable set of BCs. For a semi-infinite plate and three-dimensional heat flow, the thermal PSF can be calculated as follows:

$$\Phi_{\text{PSF,heat}}(r,t) = G_{\text{heat}}(r,t) *_r \; I_r(r) *_t \; I_t(t) \;, \tag{2.58}$$

where $G_{\text{heat}}(r,t)$ is the Green's function solution as obtained in Equation (2.17), I_r is the spatial structure of the illumination and I_t its temporal structure. The MTF of the thermal diffusion process can then be derived from the Fourier transform of the thermal PSF:

$$\begin{aligned}\text{MTF}_{\text{heat}}(\zeta_r,t) &= \left|\mathcal{F}\left[G_{\text{heat}}\right](\zeta_r,t)\right| \cdot \left|\mathcal{F}\left[I_r\right](\zeta_r)\right| \\ &= \text{MTF}_{\text{diffusion}}(\zeta_r,t) \cdot \text{MTF}_{\text{illumination}}(\zeta_r)\end{aligned} \tag{2.59}$$

Evaluating $\text{MTF}_{\text{diffusion}}(\zeta_r,t)$ at the time corresponding to the diffusion length of L_{diff} (i.e., the structure to be resolved is located at a distance of L_{diff} to the surface of the OuT), leads to the following equation:

$$\mathcal{F}\left[G_{\text{heat}}(r, {}^{L_{\text{diff}}^2}\!/\!_{\alpha})\right](\zeta_r) = \frac{1}{2\pi L_{\text{diff}}} \cdot \exp\left(-4\pi^2 L_{\text{diff}}^2 \zeta_r^2\right) \tag{2.60}$$

A detailed derivation of Equation (2.60) can be found in Appendix A1. Plotting $\text{MTF}_{\text{diffusion}}(r, {}^{L_{\text{diff}}^2}\!/\!_{\alpha})$ (i.e., the thermal MTF for a point-like heating) for different depths together with the MTFs for ideal lenses for reference as shown in Figure 2.16 results in the plot shown in Figure 2.17.

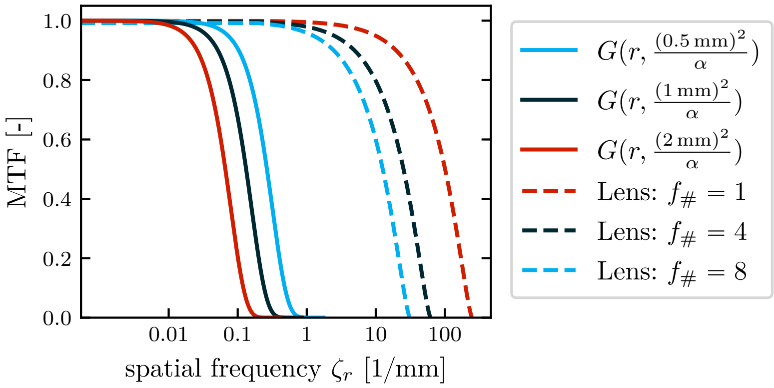

Figure 2.17: MTF of the thermal diffusion $\mathrm{MTF}_{\mathrm{diffusion}}$ evaluated at different depths: the spatial frequency transmission characteristic of thermal diffusion is shown for depths of $L_{\mathrm{diff}} = \{0.5,\ 1,\ 2\}\,\mathrm{mm}$. For further reference, the MTFs for an ideal lens with different f-numbers are shown in addition. As can be clearly observed, the spatial cut-off frequency is substantially lower for thermal processes than for optical systems.

In Figure 2.17 it can be clearly observed that the spatial cut-off frequency is orders of magnitude lower for the thermal MTF even for shallow depths than for optical imaging with a lens. As further discussed in Section 3.1, this poses one of the substantial challenges of classical TT methods. An important observation to make from Equation (2.60) is that the MTF (and therefore the spatial resolution limit) is not dependent on any material parameters and is only dependent on the depth L_{diff} at which it is evaluated at. However, the material dependence comes back into play when performing real world measurements as the diffusion time corresponding to the depth L is influenced by the thermal diffusivity α of the OuT.

It has to be noted that all previously shown derivations for the transmission behavior of the thermal diffusion are only valid for heat diffusion due to photothermal excitation using illumination patterns which are not entirely uniform over the ROI, as the diffusion process has to be sufficiently three-dimensional such that the solution to the heat PDE presented in Equation (2.17) is applicable. While for solutions with lower dimensional heat flow a similar argument can be made regarding its MTF, this thesis restricts itself to the three-dimensional heat flow case because internal defects are mostly small and scarce and therefore their thermographic signal is mostly three-dimensional, since they resemble quasi “point-like” objects.

2.2.3 Resolution Limits imposed by the Illumination

As well as the temperature measurement and the thermal diffusion, the shape of the illumination $I_r(r)$ is also influencing the spatial resolution of the thermographic measurement as it is an integral part of the thermal PSF (cf. Equation (2.58)). The spatial structure of the illumination acts like an aperture limiting the area of effect of the imposed heat flow on the OuT. Therefore, its size and spatial structure strongly influences the spatial frequency content of the thermographic measurement and the range of detectable spatial frequencies. Of all the possible patterns, there are two which will be the focus of the following discussion, as they are most commonly used within active TT, namely focused Gaussian beams and flat-top profiles.

Focused Gaussian Beam

Gaussian beam profiles are typically observed with using a laser as the illumination source. Focusing a laser with Gaussian beam profile onto a surface results in a circular illumination spot, where d_{spot} denotes its $^1/_{\mathrm{e}^2}$ diameter. The resulting intensity profile, photothermally heating the OuT, can then be described by:

$$I_{\text{r,Gaussian}}(r, z = 0) = I_0 \cdot \exp\left(-\frac{2r^2}{d_{\text{spot}}^2}\right) , \tag{2.61}$$

with I_0 being the intensity measured at $I(r = 0, z = 0)$. Its effective MTF can then be derived as follows:

$$\begin{aligned} \mathrm{MTF}_{\text{Gaussian}}(\zeta_r) &= |\mathcal{F}[I_{\text{r,Gaussian}}](\zeta_r)| \\ &= \frac{I_0}{2}\sqrt{\frac{\pi d_{\text{spot}}^2}{2}} \cdot \exp\left(-\frac{d_{\text{spot}}^2 \zeta_r^2}{2}\right) . \end{aligned} \tag{2.62}$$

A detailed derivation of Equation (2.62) can be found in Appendix A2. In Figure 2.18, $\mathrm{MTF}_{\text{Gaussian}}$ is shown for a representative set of typical spot sizes. While it can be observed that the maximum transmissible spatial frequency is decreasing with increasing spot sizes and therefore smaller spot sizes are beneficial for resolving smaller or more detailed structures, there exists also a lower bound for the spot size. On the one hand, this bound is set by the refractive power of the lens system used to project the laser beam onto the OuT. While increasing the refractive power has its limits due to material and geometrical constraints, also the working distance decreases with smaller spot size further limiting the range of practical values. On the other hand, by decreasing the spot size and keeping the intensity constant, the irradiance onto the OuT increases. Therefore, to stay within permissible limits for the irradiance for nondestructive testing also constrains the spot size.

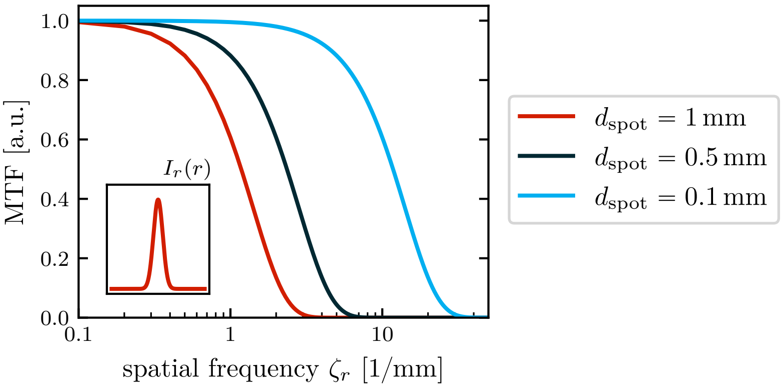

Figure 2.18: MTF of the Gaussian beam profile for different spot sizes d_{spot}: for $d_{\mathrm{spot}} \in \{0.1,\, 0.5,\, 1\}$ mm the transmission behavior of spatial frequencies is shown. While larger spot sizes lead to significantly lower maximum transmissible spatial frequencies, the frequency cut-off is still about 10× higher than that shown in Figure 2.17 for thermal diffusion.

Flat-Top Profile

The spatial structure $I_r(r)$ of a flat-top profiled beam resembles a rectangular function. For a rotational symmetric profile with diameter d_{spot}, it can be defined as follows:

$$I_{\mathrm{r,flat\text{-}top}}(r) = I_0 \cdot \mathrm{rect}\left(\frac{2r}{d_{\mathrm{spot}}}\right) \tag{2.63}$$

$$\begin{aligned} \Rightarrow \qquad \mathrm{MTF}_{\mathrm{flat\text{-}top}}(\zeta_r) &= |\mathcal{F}[I_{\mathrm{r,flat\text{-}top}}](\zeta_r)| \\ &= \left|\frac{d_{\mathrm{spot}}}{2} \cdot \mathrm{sinc}\left(\frac{d_{\mathrm{spot}} \cdot \zeta_r}{2}\right)\right| \ , \end{aligned} \tag{2.64}$$

with $\mathrm{sinc}(x) = {}^{\sin(\pi x)}/_{\pi x}$. Compared to the MTF of the Gaussian beam, the MTF of the flat-top profile features multiple zeros at $\zeta_r = \frac{2n}{d_{\mathrm{spot}}}\ \forall n \in \mathbb{N}^+$, while the enveloping amplitude of the MTF decreases with $\mathrm{MTF}_{\mathrm{flat\text{-}top}} \propto {}^1/_{\zeta_r}$ slower than the MTF of the Gaussian beam profile ($\mathrm{MTF}_{\mathrm{Gaussian}} \propto \exp(-\zeta_r)$). However, despite those differences the overall spatial frequency transmission characteristics in the context of TT is qualitatively similar. In Figure 2.19, $\mathrm{MTF}_{\mathrm{flat\text{-}top}}(\zeta_r)$ is shown for several spot diameters. If the flat-top profile is confined to a rectangular spot with as size of $d_{\mathrm{spot,x}} \times d_{\mathrm{spot,y}}$ instead of a rotational symmetric spot, the intensity profile can be described analogous as follows:

$$I_{\mathrm{xy,flat\text{-}top}}(x, y) = I_0 \cdot \mathrm{rect}\left(\frac{2x}{d_{\mathrm{spot,x}}}\right) \mathrm{rect}\left(\frac{2y}{d_{\mathrm{spot,y}}}\right) \ , \tag{2.65}$$

with an analogously defined MTF. As mentioned in Section 2.2.1, the MTF of the pixelated detector of an infrared camera can also be modelled by the MTF of a rectangular aperture (with

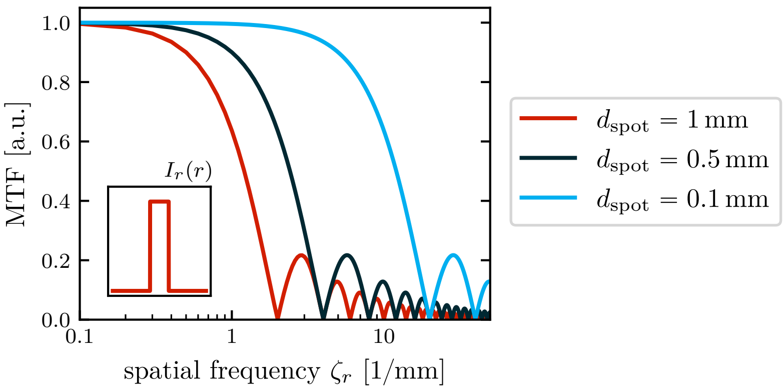

Figure 2.19: MTF of the flat-top profile for different spot sizes d_{spot}: for $d_{\mathrm{spot}} \in \{0.1, 0.5, 1\}$ mm the transmission behavior of spatial frequencies is shown. While the shown MTF for the flat-top profile features several pronounced zeros, the overall transmission performance in the context of TT is very similar to the MTF of a Gaussian beam with similar spot size. Additionally, the MTF of pixelated detectors is very well approximated by the MTF of a flat-top profile with a width equal to the pixel size.

homogeneous/flat-top profile), as laid out in Equation (2.65), with a spot size corresponding to the pixel size of the detector.

2.3 Resolution Enhancement beyond Classical Limits

Even though the resolution of any thermographic measurement is limited by the combined MTFs of the measurement setup, it is still possible to surpass this limit and achieve so-called *super resolution* (*SR*). SR methods overcome the otherwise insurmountable restrictions caused by the MTF to the achievable resolution by combining multiple different measurements. Even though each independent measurement has to still obey the classical resolution limit, carefully designing each measurement such that a different part of the desired information is captured, leads to an overall increase in resolution. While performing the same measurement n_m times already helps to increase the achievable signal-to-noise ratio (SNR) by $\mathrm{SNR} \propto \sqrt{n_m}$ as the expected value for Gaussian measurement noise $\mathrm{E}\left[\mathcal{N}_{\text{noise}}\right] = 0$, only varying parts of the measurement setup (i.e, the illumination, temperature measurement, etc.) can overcome the limits imposed by the MTF of the measurement setup. However, all SR methods have to compromise between resolution gain and experimental complexity.

2.3.1 Geometric Super Resolution

Overcoming the resolution limit imposed by the discretization of the image to be measured by a detector made up of discrete pixels (cf. Section 2.2.1) is the goal of geometric SR methods. This can be achieved by combining a set of n_m different measurements. For each of the measurements, the sensor has to be moved relative to the OuT in order to create a unique discretization of the signal to be measured in each case. The working principle of geometrical SR is displayed in Figure 2.20.

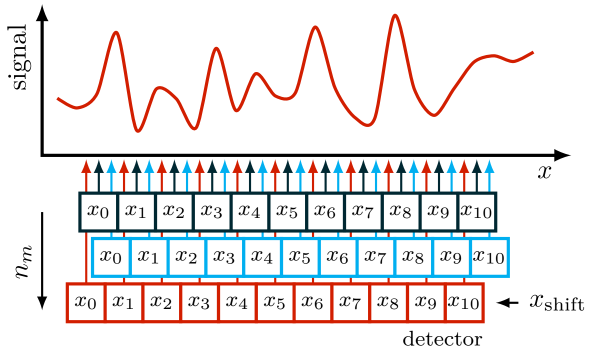

Figure 2.20: Principle of geometric SR: by combining a total of n_m measurements with a shifted detector position by x_{shift} a denser measurement grid can be constructed, allowing for the signal to be reconstructed from interpolating all measurements. As the spatial cut-off frequency is dependent on the pixel size, the now reduced effective pixel size after reconstruction allows for the recording of higher spatial frequencies.

The relative movement between sensor and OuT can be achieved in a variety of ways, e.g., by deliberately moving the sensor between consecutive captured frames [42], by exploiting vibration within the measurement setup [43] or by moving the OuT between frames [44]. In addition, there also exist commercially available modern IR-cameras that directly include a geometrical SR feature by optically deflecting the captured image to multiple positions onto the internal sensor [45].

Furthermore, there also exist machine learning based geometrical SR methods that are trained to extrapolate to a higher resolution from even a single measurement [46]. While this significantly decreases the experimental complexity as only a single measurement is necessary, the resulting high-resolution data will only approximate the real signal and no guarantee for its correctness is given, which makes those methods inadequate for quantitative measurements.

2.3.2 Optical Super Resolution

With the help of optical SR methods, it is possible to overcome the resolution limit of optical imaging (cf. Section 2.2.1). The limitations imposed by the MTF of optical systems causes that no structure which is significantly larger than half of the wavelength of light used for imaging can be resolved (cf. Equation (2.53) as $f_\# \gtrapprox 1$). Depending on the exact field of application, there exists a wide variety of optical SR methods to overcome this limit based on exploiting different physical effects, such as stimulated emission depletion microscopy, whose creator Stefan W. Hell was awarded the Nobel Prize in Chemistry in 2014 for its invention [47]. Another prominent and illustrative representative within the field of optical SR methods is structured light microscopy (SIM) [48]. Here, the signal to be measured is superimposed by a spatially structured illumination pattern and multiple measurements with varying patterns are performed. Even though each individual measurement is limited by the pass-band of the MTF of the optical system (and illumination), the patterns are chosen such that for each measurement the frequency content of the signal is phase-shifted partly into the pass-band of the optical MTF [49]. Multiple different measurements then allow reconstructing the signal's spatial frequency content at much higher resolution. The working principle of optical SR is illustrated in Figure 2.21. Phenomenologically, this can be described similarly to the formation of Moiré patterns. When bringing two different frequencies f_1 and f_2 to interference, beat frequencies $f_b = |f_2 - f_1|$ will appear. As those are much smaller than any of the two constituent frequencies, they can be measured much more easily. Furthermore, if one of the constituent frequencies (i.e., the spatially structured illumination pattern) and the beat frequency is known (i.e., is measured), the remaining frequency can be calculated. Due to the limited bandwidth of the MTF, multiple measurements with varying illumination pattern are then necessary to reconstruct the original signal as every measurement only gives insight into a part of its true frequency content.

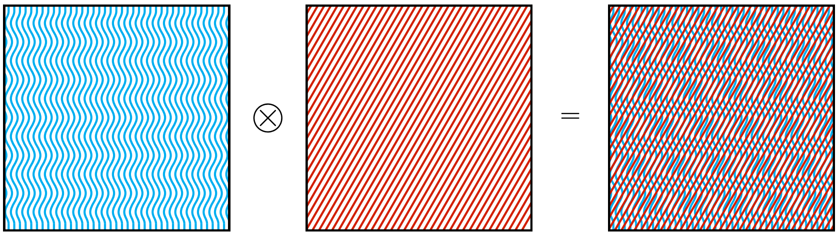

Signal

Illumination Structure

Interfered Signal

Figure 2.21: Principle of optical SR: if a signal (left) is brought to interference with a pattern with known frequency content (middle), the resulting interfered signal (right) will show beat tones at a lower frequency than present in the signal to be measured (cf. Moiré patterns). This allow shifting the frequency content of the signal into the MTF pass-band of the detector. However, multiple measurements with different illumination structures are necessary to reconstruct the initial signal.

While SIM-based SR methods are widely applied in conjunction with fluorescence in microscopy, there are also applications within thermographic testing of thin biofilms [50, 51]. However, the method is mostly confined to imaging structures which lie on the surface of the OuT or closely to it.

2.3.3 Photothermal Super Resolution

In Section 2.2, the influence of the illumination, thermal diffusion and the temperature measurement has been analyzed, and thermal diffusion has been shown to be the worst offender when it comes to limiting the resolution of TT of internal defects. Therefore, the application of SR methods targeting the improvement of this shortcoming shows arguably the highest potential (cf. Section 2.2.2). An important representative of an SR method to overcome the limits of thermal diffusion is called *photothermal super resolution*. Initially conceived by an Austrian researcher group around Burgholzer et al. [52], the method is based on subjecting the OuT to a set of different illumination patterns photothermally heating the OuT. In an additional reconstruction step, taking the thermal PSF of the OuT into account, the internal structure of the OuT is reconstructed iteratively solving a suitably regularized inverse-problem. While initially flash lamps with exchangeable intensity mask were utilized as a heat source for the method, Ahmadi et al. [53, 54] developed the method further by using one-dimensional laser heating (laser line and line patterns), making the method more suitable for detecting defects deep within the OuT.

As this thesis heavily builds upon the photothermal SR method and its technological advancement, the method, its underlying modelling of internal defects and the mathematical reconstruction approach is set out below.

Defect Model

The temperature evolution for an OuT with unknown defects can be approximated by the superposition of the temperature evolution for a sound OuT $T_{\text{diff,sound}}$ and the thermal signal caused by the defects $T_{\text{diff,defect}}$:

$$T_{\text{diff}}(r,t) = T_{\text{diff,sound}}(r,t) + T_{\text{diff,defect}}(r,t) \tag{2.66}$$

For a sound OuT, the increase in temperature from T_0 caused by an external heat flow can be expressed as the convolution of the thermal PSF $\Phi_{\text{PSF,sound}}$, as described in Equation (2.58), with a heat source distribution function a_{ext}:

$$T_{\text{diff,sound}}(r,t) = \Phi_{\text{PSF,sound}}(r,t) *_r \; a_{\text{ext}}(r) \; . \tag{2.67}$$

If a single illumination consists of a set of locations $a_{\text{illum}} = \{(x,y) \in \mathbb{R} \times \mathbb{R} \,|\, \text{illumination with structure } I_r \text{ is centered at } (x,y)\}$ at which an individual photothermal heating with structure I_r takes place (e.g., a_{illum} contains the center points of all lines for a line pattern or the center of the ROI for a homogeneous illumination), then a_{ext} forms a set of unit impulses placed at those locations:

$$a_{\text{ext}}(r) = \begin{cases} 1 & \text{if } r \in a_{\text{illum}} \\ 0 & \text{otherwise} \end{cases} \; . \tag{2.68}$$

With the help of the shifting property of the convolution operator and thanks to the linearity of the heat PDE, this formulation of $T_{\text{diff,sound}}$ allows the description of illumination patterns that consists of illumination primitives (spots, squares, lines), since in practice more complex patterns can be only feasibly constructed by composing easily generatable illumination primitives.

For the description of the influence of a defect on the temperature difference, a similar approach can be chosen. For each particular defect, a corresponding PSF $\Phi_{\text{PSF,defect}}$ can be found that approximates its thermal response. By also introducing a distribution function a_{int} by which the defect's PSF is convolved, the location and distribution of similar defects can be encoded:

$$T_{\text{diff,defect}}(r,t) = \Phi_{\text{PSF,defect}}(r,t) *_r \; a_{\text{int}}(r) \; . \tag{2.69}$$

The internal defect distribution can be suitably defined as follows:

$$a_{\text{int}}(r) = \begin{cases} \zeta_i & \text{if a defect is present at } r \\ 0 & \text{otherwise} \end{cases} \; , \tag{2.70}$$

where $\zeta_i \in [0, 1[$ is the defect contrast of the ith defect. Due to the fact that defects show in thermographic measurements as hot-spots in the temperature profile as they impede the heat flow (due to the positive effusivity contrast), their contribution to the differential temperature profile appears phenomenologically as if there were an internal heat source at the defect location. The duality of defects acting as *apparent* heat sources also shows in the similarity of Equation (2.69) and Equation (2.67). This connection is further visualized in Figure 2.22. As the defect signal depends on the energy transfer due to the illumination, it always holds true that $\zeta_i < 1$ due to energy conservation, as a higher value would indicate that additional heat energy is introduced by the defect.

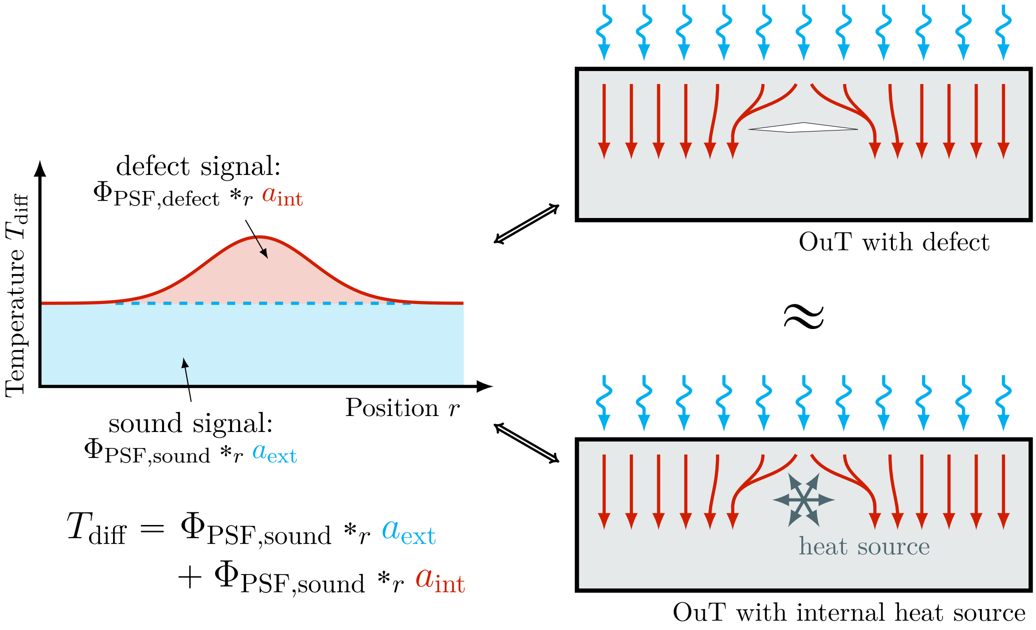

Figure 2.22: Defect model within photothermal SR: The temperature differential caused by externally heating of a defective OuT can be modelled by the superposition of the response of a sound OuT and the thermal influence of the defect. Because defects impede heat flow by presenting a contrast in effusivity, they appear as hot spots in the temperature difference signal, similar to the influence of a fictitious internal active heat source at the same location.

However, determining $\Phi_{\text{PSF,defect}}$ is far from trivial, as every defect features its own individual $\Phi_{\text{PSF,defect}}$ depending on its size, depth and effusivity contrast. Since the nature of NDT is to determine whether an OuT contains a previously unknown set of defects, coming up with a representative $\Phi_{\text{PSF,defect}}$ is only possible, if at all, with prior knowledge of very characteristic defects. Therefore, in order to simplify the problem, a common PSF for the illumination and the defect signal is chosen and this PSF is defined to be the PSF of the illumination $\Phi_{\text{PSF}} := \Phi_{\text{PSF,sound}}$ by making use of the analogy expressed in Figure 2.22. This leads to the following simplification:

$$
\begin{aligned}
T_{\text{diff}}(r,t) &= T_{\text{diff,sound}}(r,t) + T_{\text{diff,defect}}(r,t) \\
&= \Phi_{\text{PSF}}(r,t) *_r \, (a_{\text{ext}}(r) + a_{\text{int}}(r)) \qquad (2.71) \\
&= \Phi_{\text{PSF}}(r,t) *_r \, a(r) \ , \qquad (2.72)
\end{aligned}
$$

where $a(r) = a_{\text{ext}}(r) + a_{\text{int}}(r)$ is the combined heat source distribution.

Crucially, while this modelling approach offers a straightforward analytical representation of the surface temperature evolution of an OuT with internal defects subjected to external heating, one has to be aware that the following greatly simplifying assumptions are made:

- All defects are modelled as active internal heat sources.
- The PSF of the defect signals $\Phi_{\text{PSF,defect}}$ is defined to be equal to the PSF of the external heating $\Phi_{\text{PSF,sound}}$.
- Defects are sparsely distributed within the ROI.

Mathematical Formulation of the SR Problem

As the information of multiple measurements $m \in [1, \ldots, n_m]$ has to be combined in order to achieve SR capabilities, Equation (2.72) extends to the following:

$$T^m_{\text{diff}}(r,t) = \Phi_{\text{PSF}}(r,t) *_r \, a^m(r) \ , \qquad (2.73)$$

where a superscript of m indicates the mth measurement. Every measurement m contains a subset of information about the internal heat source distribution a_{int} and therefore the internal defect structure, thus, summing over all measurements fuses this information together. Since summing also entails the summation of the external heat source distributions for all measurements a^m_{ext}, the following condition in form of a homogeneity constraint for the sum of all illumination patterns has to be met:

$$\Phi_{\text{PSF}}(r,t) *_r \sum_{m=1}^{n_m} a^m_{\text{ext}}(r) \approx \text{const.} \ . \qquad (2.74)$$

Only this necessary condition stated in Equation (2.74) allows inverting the photothermal SR problem and being able to extract the internal heat source distribution part from the combined heat source distribution a in a blind reconstruction context. Blind reconstruction means here, that at no point the external heat source distribution is used as input for the model and only the homogeneity constraint is enforced. This approach has the advantage that any errors in the experimental implementation of the illumination pattern projection does not propagate to the end result. Even though mathematically the weaker condition $\sum_{m=1}^{n_m} a^m_{\text{ext}}(r) \approx \text{const.}$ would suffice for blind reconstruction, this is not enough in practice, as a_{int}^m is not independent of a_{ext}^m as the defects are not truly heat sources themselves but only appear accordingly. Therefore, including the PSF into the condition makes sure that every location r is in total exposed to equal amounts of heating. On the other hand, to guarantee separability the supposedly trivial condition of $1/n_m \sum_{m=1}^{n_m} a_{\text{int}}^m(r) = a_{\text{int}}(r) \not\approx \text{const.}$ has to be fulfilled, which is a direct consequence of the sparsity requirement for the presence of defects, as deviating from this requirement would mean that the ROI either is fully made up of defective area or there is no defect at all (trivial case).

By obeying the stated homogeneity constraints, it can be observed that if it is possible to invert Equation (2.73) to obtain a^m for every measurement m, then a summation over all measurements leads to the separation of the internal heat source distribution a_{int}:

$$
\begin{aligned}
& \sum_{m=1}^{n_m} a^m(r) = \sum_{m=1}^{n_m} a_{\text{int}}^m(r) + \sum_{m=1}^{n_m} a_{\text{ext}}^m(r) \\
\Rightarrow \quad & \Phi_{\text{PSF}}(r,t) *_r \sum_{m=1}^{n_m} a^m(r) = \Phi_{\text{PSF}}(r,t) *_r \sum_{m=1}^{n_m} a_{\text{int}}^m(r) + \Phi_{\text{PSF}}(r,t) *_r \sum_{m=1}^{n_m} a_{\text{ext}}^m(r) \\
\overset{\text{Eq. (2.74)}}{\Rightarrow} \quad & \Phi_{\text{PSF}}(r,t) *_r \sum_{m=1}^{n_m} a^m(r) = n_m \cdot \Phi_{\text{PSF}}(r,t) *_r \; a_{\text{int}}(r) + \text{const.} \\
\Rightarrow \quad & a(r) = \sum_{m=1}^{n_m} a^m(r) = n_m \cdot a_{\text{int}}(r) + \text{const.} \; .
\end{aligned}
\tag{2.75}
$$

The constant offset and the scaling by n_m can then easily be removed. As a_{int} is a direct representation of the internal defect pattern, finding a_{int} when Φ_{PSF} is known as a prior is the main task within photothermal SR reconstruction.

As commonly most OuTs resemble some kind of plate like structure with known thickness L and material parameters α, c_p and ρ, for the scope of this thesis the following PSF considering multiple reflections of the thermal wave from the back wall will be used for all SR reconstruction problems [17, 55]:

$$
\Phi_{\text{PSF}}(r,t) = \left[\frac{2\,\hat{\text{Q}}}{c_p \rho (4\pi\alpha t)^{n_{\text{dim}}/2}} \cdot \exp\left(-\frac{(r-\bar{r})^2}{4\alpha t} \right) \cdot \sum_{n=-\infty}^{\infty} R^{2n+1} \cdot \exp\left(-\frac{(2nL)^2}{4\alpha t} \right) \right] *_r \; I_r(r) *_t \; I_t(t) \; , \tag{2.76}
$$

where $\hat{Q}$ is the amplitude of the absorbed heat flow $\dot{Q}(t) = \hat{Q} \cdot I_t(t)$ imposed by the illumination, which already takes the emissivity/absorptivity of the OuT into account. For more complex parts or anisotropic materials, Φ_{PSF} has to be determined accordingly either by solving the heat PDE with suitable BCs or by finite-element modelling.

Numerical Inversion

Trying to solve the severely ill-posed problem stated in Equation (2.73) for a_{int}^{m} for all individual measurements m leads to the following minimization problem:

$$\underset{a_{\mathrm{rec}}^{m}}{\mathrm{minimize:}} \quad \frac{1}{2} \cdot \|\Phi_{\mathrm{PSF}} *_{r} a_{\mathrm{rec}}^{m} - T_{\mathrm{diff}}^{m}\|_{2}^{2} \quad \forall m \; . \tag{2.77}$$

Due to the involved ill-posedness, solving the minimization problem results only in a reconstruction a_{rec}^{m} of a_{int}^{m} for which ideally a_{rec}^{m} converges to a_{int}^{m} for $n_m \to \infty$. In order to improve the reconstruction quality dramatically, regularization is applied. As a_{int} is rather sparse (defects are rare events) and the underlying physics is constrained by heat conduction, a $\ell_{2,1} + \ell_2$ regularization scheme has proven to yield the best results [56]:

$$\underset{a_{\mathrm{rec}}}{\mathrm{minimize:}} \quad \frac{1}{2} \cdot \|\Phi_{\mathrm{PSF}} *_{r} a_{\mathrm{rec}}^{m} - T_{\mathrm{diff}}^{m}\|_{2}^{2} + \lambda_{2,1} \cdot \|a_{\mathrm{rec}}\|_{2,1} + \frac{\lambda_2}{2} \cdot \|a_{\mathrm{rec}}^{m}\|_{2}^{2} \; , \tag{2.78}$$

where $\lambda_{2,1} \in \mathbb{R}$ and $\lambda_2 \in \mathbb{R}$ are scalar parameters for tuning the strength of each individual regularizer. The operator $\|\cdot\|_{2,1}$ is the 2,1-norm, defined as:

$$\|a_{\mathrm{rec}}\|_{2,1} = \sum_{r} \sqrt{\sum_{m} |a_{\mathrm{rec}}^{m}|^{2}} \; . \tag{2.79}$$

The core idea of regularization is to add additional terms to the minimization problem which are meant to be minimized simultaneously in order to promote certain properties of the desired solution. The ℓ_2-regularization, or Tikhonov regularization as it is called, adds the Euclidean norm of the result to the minimization and thus promotes results containing only small numbers, preventing the minimization from blowing up. As most physical energy transport processes tend towards minimization of energy, this is a reasonable addition to make. $\ell_{2,1}$-regularization on the other hand adds the 2,1-norm of the result, which consists of taking the 1-norm in space and the 2-norm over all measurements m for every individual location r. This so-called block-sparsity norm promotes sparse results and connects the information of all individual measurements together by processing the information gathered about a location r for all measurements into a single output value [57]. As a_{int} does not change over the measurements m as the internal defect structure is fixed, the information from multiple measurements about a single location r only gets complemented by the addition of this regularizer. How to efficiently solve Equation (2.78) for large two-dimensional ROIs and a large number of measurements n_m is laid out in Section 4.1 and is integral part of this thesis.

Elimination of the Time Dimension

As solving the photothermal SR problem stated in Equation (2.73) is quite computationally expensive, the problem complexity can be drastically reduced by eliminating the time dependency of the equation. As the time evolution mostly conveys information about the depth at which a possible defect is detected to exist at (cf. Equation (2.13): diffusion length), by choosing a particular time step $t = t_{\text{eval}}$ the detection can be restricted to a certain depth range up to $L_{\text{eval}} = \sqrt{\alpha \cdot t_{\text{eval}}}$. A suitable value for t_{eval} can be derived either from a conventional thermographic measurement by determining the depth of defect structures of interest first, from SNR-considerations, from the OuT's functional specification or from prior knowledge about the origin and nature of the defects ought to be detected. As the photothermal SR problem is decoupled in time (i.e., it can be solved for every time step independently as no temporal history is taken into account), it is further possible to solve it for a set of time steps in order to achieve a three-dimensional representation of the defect. However, as SR is only achieved in space (x, y), the depth resolution of the method is identical to conventional TT.

While the simplistic approach of choosing one particular time step has proven to already yield satisfying results [A4], it is also possible to eliminate the time dimension by preprocessing the measured temperature data first. In general, every preprocessing that condenses the information conveyed by the time dimension into a smaller dataset is suitable. For example, this can either be implemented by performing a PPT-evaluation and processing only phase or amplitude images of certain frequencies or by previous TSR-analysis and subsequent processing of certain coefficient images (cf. Section 2.1.4).

Moreover, Ahmadi et al. achieved an elimination of the time dimension by finding the maximum contrast frame after a virtual wave (VW) transformation of the measured data [A5]. The VW transformation solves an additional ill-posed inverse problem that converts the diffusive heat signal into an equivalent propagating wave signal. As this transformation is suitable for increasing the depth resolution of the measurement and already filters out the influence of thermal diffusion in time, VW transformation is a noteworthy candidate for augmenting photothermal-SR reconstruction. However, solving the underlying additional ill-posed inverse problem comes at a significant computational cost.

3. Motivation and Research Objectives

This chapter focuses on the motivations and goals for the enhancement and further development of photothermal SR reconstruction as a technique for resolving deeply buried internal defects. The discussion encompasses the limitations of conventional testing methods (cf. Section 2.1.4), the limitations encountered with state-of-the-art photothermal SR reconstruction prior to the advances made during the work of this thesis, and the overarching research objective.

3.1 Limitations of Conventional Testing Methods

While the different conventional TT methods available all aim to maximize the detection and resolution power of active thermographic measurements, they mostly still fall short of defeating the adverse effects of thermal diffusion on the defect response signal. Commonly, this is expressed by the fact that all conventional detection methods are limited by the thermal aspect ratio of the defect γ_{defect}, which is defined as the ratio between the spatial (spherical) width of the defect d_{defect} and the depth L_{defect} at which it occurs [58]:

$$\gamma_{\text{defect}} = \frac{d_{\text{defect}}}{L_{\text{defect}}} \ . \tag{3.1}$$

A schematic depiction of all the involved parameters can be found in Figure 3.1.

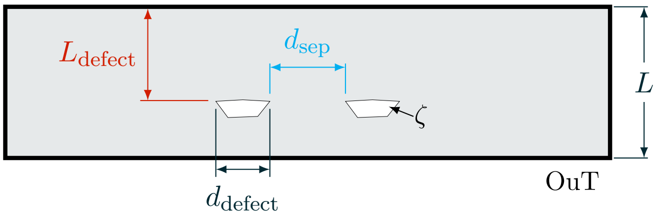

Figure 3.1: Defect aspect ratio as defined within the context of thermographic testing: for evaluating the detectability of defects, the ratio between the defect size and its depth needs to be sufficiently high. A similar argument can be made for evaluating the separability of neighboring defects, where a separation distance to defect depth ratio can be consulted. Additionally, also the effusivity contrast ζ of each defect has to be taken into account.

As a generally accepted rule of thumb for TT, the aspect ratio should be $\gamma_{\text{defect}} \gtrapprox 1$ for a defect to be detectable [59]. While this is a very simplifying rule and more in-depth limits for the detectability of defects by their aspect ratio exist [60], it already gives a good approximation of the capabilities of conventional TT. Furthermore, the detectability of defects is also dependent on the achievable SNR of the temperature measurement [61], as the defect signal has to be significantly larger than the measurement noise to be detectable. This can either be influenced by lowering the measurement noise (e.g., by using an IR-camera with lower NETD or by performing multiple identical measurements) or by increasing the thermal signal. As the thermal signal, and the thermal defect signal in turn, is mainly dependent on the emissivity of the OuT and the heat flow imposed by the illumination, blackening the OuT's surface or increasing the irradiance of the illumination can also help to increase the SNR. Furthermore, the defect signal is also dependent on the effusivity contrast ζ with respect to the bulk material. While this contrast inherently is predetermined and immutable, it still limits the detectability of only minute flaws (e.g., impurities) in the OuT.

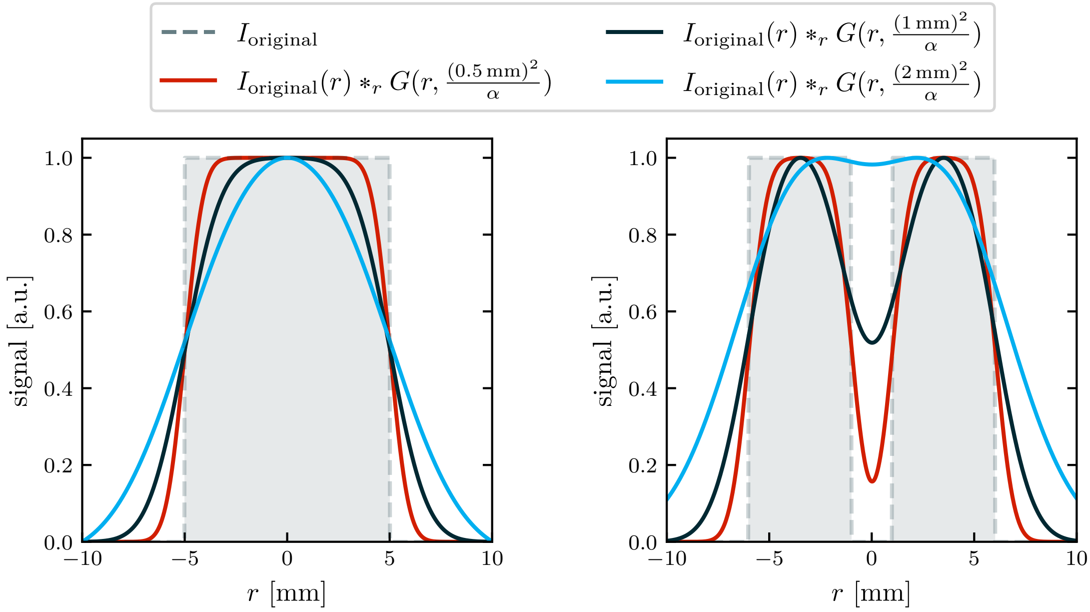

(a) Signal of a single defect structure with $d_{\text{defect}} = 10\,\text{mm}$.

(b) Signal of two closely-spaced defect structures with $d_{\text{defect}} = 5\,\text{mm}$ at a separation distance of $d_{\text{sep}} = 2\,\text{mm}$.

Figure 3.2: Thermographic defect signals distorted by thermal diffusion: as all thermographic defect signals are affected by the MTF of thermal diffusion, the defect signal is severely disfigured depending on the defect depth. While for mere detection of defects this effect has only a minor influence on the detectability (left), for resolving the defect signal it is a major issue (right). As can be seen in the right-hand plot, the separability of closely-spaced defects in particular decreases drastically as the defect depth increases. In both plots, all signal amplitudes are normalized to a maximum of 1.

However, while the detection of defects is already a major step within TT and NDT in general, the exact resolution of the defect shape is an important aspect as well, as the exact size and particular shape of defects can have a strong influence on the tolerability of the defect according to the OuT's functional specification. Since thermal diffusion acts as a spatial frequency filter for the defect signal (cf. thermal MTF in Section 2.2.2), the resolution of the size and shape of deeply buried defects is heavily compromised. This is especially visible when trying to resolve two closely-spaced defects, as with increasing depth both defect signals overlap so far that they are no longer separable (cf. Sparrow limit in Section 2.2).

This effect is illustrated in Figure 3.2, where the influence of the thermal MTF on the defect signal for a single defect is juxtaposed with the effect on a closely-spaced defect pair with a separation distance of $d_{\text{sep}} = 2\,\text{mm}$. For the resolution of closely spaced defects, an aspect ratio γ_{sep} similar to γ_{defect} can be defined:

$$\gamma_{\text{sep}} = \frac{d_{\text{sep}}}{L_{\text{defect}}} \ , \tag{3.2}$$

where $\gamma_{\text{sep}} \cong \gamma_{\text{defect}}$ can be considered congruent regarding their validity for evaluating resolvability. In Figure 3.2 it can be observed that for a depth of $L_{\text{defect}} = 2\,\text{mm}$ (i.e., $\gamma_{\text{sep}} = 1$) almost no observable minimum between the two defect signals is present anymore.

As active TT with a sufficiently short heating of an internal defect can be considered probing the defect by sending out a (diffusive) thermal wave and recording the reflected signal, the resolving power of the method is strongly correlated to the properties of the thermal PSF for three-dimensional heat flow. By looking at its spatial width quantified by the full width at half maximum (FWHM), the resolution limit at which certain defect structure sizes can be resolved can be approximated. The FWHM of the thermal PSF approximated by G_{heat} (cf. Equation (2.17)) shows the following dependency:

$$\text{FWHM}\left(G_{\text{heat}}\right) = 4\sqrt{\ln(2)} \cdot \sqrt{\alpha \cdot t} \tag{3.3}$$

$$\begin{cases} \text{FWHM}\left(G_{\text{heat}}\right) \propto \sqrt{\alpha} \\ \text{FWHM}\left(G_{\text{heat}}\right) \propto \sqrt{t} \\ \text{FWHM}\left(G_{\text{heat}}\right) \propto L_{\text{diff}} \end{cases} . \tag{3.4}$$

The proportionalities of the FWHM shown in Equation (3.4) demonstrate that the width of the thermal PSF increases with increasing thermal diffusivity and evaluation time. Consequently, it is also linearly increasing by diffusion length (detection depth). This effect can be rediscovered in the depth dependency of the thermal MTF (cf. Section 2.2.2). All this aforementioned degradation of the resolution can be at its core attributed to the diffusive nature of the PDE, as methods based on the physics of propagating waves (i.e., ultrasonic testing (UT), radiographic testing (RT), etc.) do not suffer from this specific issue. Amongst other reasons, this is prominently rooted in the phase velocity dispersion of thermal waves ($v_{\text{wave}} \propto \sqrt{2\alpha\,\omega_{\text{wave}}}$) and the high inherent dispersive attenuation, as any thermal wave is attenuated to an amplitude fraction of $1/e$ after a penetration depth of $\mu = \sqrt{2\alpha/\omega_{\text{wave}}}$ [62]. Both effects are material dependent (α) and frequency dependent ω_{wave}. A qualitative side-by-side comparison between the evolution of a diffusive and a propagating wave characterized by their Green's functions is displayed in Figure 3.3, where the difference of propagating and diffusive energy transport can be clearly distinguished.

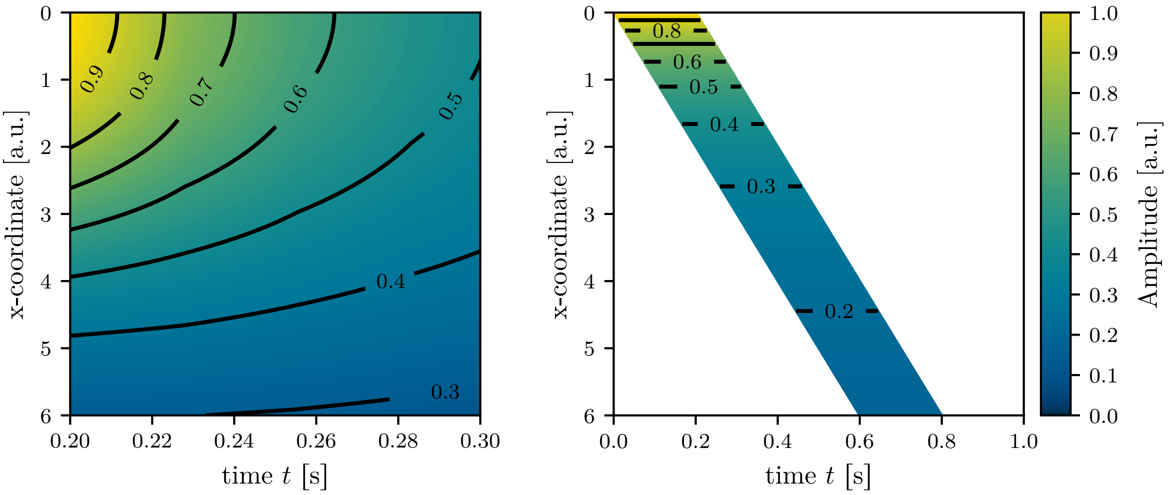

(a) Heat diffusion: $G_{\text{heat}}(r,t) *_t I_t(t)$; cf. Equation (2.17)

(b) Propagating wave: $G_{\text{wave}}(r,t) *_t I_t(t)$; cf. Equation (2.19)

Figure 3.3: Difference between propagating (right) and diffusive (left) energy transport. I_t resembles a rectangular pulse with a pulse length of $t_{\text{pulse}} = 0.2\,\text{s}$ in both cases. For the propagating wave a (dimensionless) wave speed of $c = 10$ has been chosen. It can be clearly observed that for the propagating transport process the transmitted wave stays compact over time, whereas in the diffusive process the wave spreads out thinly in all directions.

Overcoming the resolution barrier imposed by the thermal diffusion is the task of thermal SR methods. While the resolution limit of thermal SR methods is still SNR-dependent due to entropy considerations [63], for the case of photothermal SR reconstruction, the limits imposed by the thermal MTF can be significantly improved up to a resolution of defects with at least $\gamma_{\text{defect}} \gtrapprox \frac{1}{8}$ [54].

3.2 Challenges for Super Resolution Defect Reconstruction

Photothermal SR reconstruction, whose history and working principle have been introduced in Section 2.3.3, while still a niche method, has already been examined in multiple publications [52–54, A4, A5, 64, 65]. While it has already proven to be a powerful method that is able to expand the capabilities of detecting and resolving deeply-buried defects very significantly, it still suffers in its current state from several shortcomings, which can mostly be attributed to its recency.

As the method was first conceived, the necessary changing illumination patterns were generated using a flash lamp with slit masks as a heat source. For the projection of every individual pattern, a different slit mask had to be used, or a single slit mask had to be moved in several positions [52], making the experimental implementation very tedious and not very practical. Furthermore, the theoretical description of the method was limited to detecting emissivity changes within the ROI, which fell short of describing the interaction with deeply-buried defects. Later, the technique has been experimentally refined by introducing laser line heating [64]. This allowed to increase the irradiance within the ROI significantly such that it was now possible to also expand the method to the resolution of internal defects [A4]. However, the use of flash lamps with slit masks and laser lines as an illumination source only generates a two-dimensional heat flow within the OuT, since along the direction of the line the illumination does not change. Even though this limitation still allows a reconstruction of two-dimensional structures when also changing the orientation of the line pattern for each measurement, it is far from ideal to exploit the capabilities of the method fully. Due to this issue, research has been limited to the detection of one-dimensional defects. While this circumvents the problem, one-dimensional defect structures are not very common in most practical applications, further restricting the practicality of the method.

For solving the underlying inverse problem, several different inversion methods have been examined for the simplified problem of two-dimensional heat flow (line heating) [65]. However, those examinations fall short in the case of three-dimensional heat flow and two-dimensional defect structures, which are most common in practical applications. Furthermore, prior to the advances made in this thesis, the state of the art required that the user-provided parameters for the regularized inversion be determined empirically in all cases, making the inversion very slow and labor-intensive.

3.3 Research Objectives

In order to advance the method of photothermal SR reconstruction and increase its technology readiness level (TRL) [66] up to the point where it starts to become viable for practical use in demanding industrial NDT applications, the following research objectives are addressed within this thesis:

- **Determine** an efficient **numerical reconstruction algorithm** tailored for detecting and resolving arbitrarily shaped defects within two-dimensional ROIs for arbitrary illumination patterns (three-dimensional heat flow).
- **Implement** a practical **experimental setup/procedure** that enables the SR reconstruction of internal defects for two-dimensional ROIs.
- **Deal with** the **complexity explosion** that comes with two-dimensional ROIs, both numerically and experimentally.
- Find a method to **analytically simulate** the measurement process and numerical inversion step of photothermal SR reconstruction and **make predictions** about the influence of the key **experimental parameters**.
- **Experimentally validate all findings** and compare the achieved reconstructions with the results of state-of-the-art conventional thermographic detection methods **on an** exemplary **OuT**.

4. Approach and Implementation

To achieve the objectives of this thesis laid out in Section 3.3, the following approach was followed. First, suitable numerical inversion techniques of the ill-posed inverse photothermal SR reconstruction problem have been studied in order to find a functioning and performant algorithm with true two-dimensional SR capabilities. Secondly, the experimental approach behind the method has been refined in line with the requirements of the numerical inversion dealing with the disproportionately gained complexity by the dimensional expansion. Finally, a forward problem of the method is developed in conjunction with a method for automatically determining the necessary inputs to the numerical inversion of the inverse problem for known ROIs in furtherance of allowing to conduct parameter studies numerically, which are subsequently carried out to gain insights into the influence of various experimental parameters.

4.1 Expanding the Numerical Inversion of the Photothermal SR Problem

When dealing with any linear mapping A acting on a set of inputs x causing an effect b, then obtaining an unknown set of inputs x from a known result b can be achieved by finding the inverse mapping to the problem as follows:

$$Ax = b \qquad \text{, with } A \in \mathbb{R}^{m\times n},\ x \in \mathbb{R}^{n},\ b \in \mathbb{R}^{m} \tag{4.1}$$

$$\begin{aligned} &\overset{A \text{ invertible}}{\Rightarrow} && x = A^{-1}b \\ &\overset{A \text{ non-invertible}}{\Rightarrow} && x = A^{+}b\ , \end{aligned} \tag{4.2}$$

where A^{+} is the Moore-Penrose inverse or pseudoinverse of A. As long as the problem is well-defined/invertible (A is square and has full rank), finding the inverse mapping A^{-1} can be uniquely algorithmically obtained with comparably low effort. On the contrary, for ill-posed problems there exists an infinite set of solutions. While this makes the problem not uniquely solvable as it is highly unclear which of the possible solutions is actually of interest in the context of the stated problem, at least $A^{+}b$ as the solution with the smallest 2-norm stands out. However, in the context of photothermal SR reconstruction an equation of the following form has to be inverted:

$$A *_{m,n} x = b \qquad , \text{ with } A, x, b \in \mathbb{R}^{m \times n} \ . \tag{4.3}$$

Here, the matrix A is (linearly) convolved with the unknown matrix x instead of performing a matrix-vector multiplication like in Equation (4.1). Transforming Equation (4.3) into frequency space leads to a possible and unique inversion for the special case of circular convolution (indicated as $\circledast_{m,n}$) as follows:

$$\begin{aligned}
& & \mathcal{F}[A \circledast_{m,n} x] &= \mathcal{F}[b] \\
&\Rightarrow & \mathcal{F}[A] \odot \mathcal{F}[x] &= \mathcal{F}[b] \\
&\overset{\mathcal{F}[A]^{i,j} \neq 0}{\Rightarrow} & \mathcal{F}[x] &= \frac{\mathcal{F}[b]}{\mathcal{F}[A]} \\
&\Rightarrow & x &= \mathcal{F}^{-1}\left[\frac{\mathcal{F}[b]}{\mathcal{F}[A]}\right] \ ,
\end{aligned} \tag{4.4}$$

where $\odot$ indicates element-wise multiplication (Hadamard product). Circular convolution, as a special case of the convolution operation, can be transformed into the necessary linear convolution by suitably rearranging/padding the input data (cf. Section 4.1.2). However, this naïve frequency space inversion approach unfortunately is not very well suited to real world problems, as it requires $\mathcal{F}[A]$ to be free of zeros and as it is very sensitive to noise. While the frequency space inversion can be augmented with additional regularizers (cf. TV-regularization [67]) or additional noise estimation and filtering (cf. Wiener filter [68]), deconvolution as the operation is colloquially called, is a highly non-trivial task.

In the past, solving the regularized convolutional minimization problem stated in Equation (2.78) has been mainly carried out iteratively using the fast iterative shrinkage-thresholding algorithm (FISTA) or derivatives thereof in frequency space [54, 69]. While FISTA is very performant and easy to implement, within the scope of this thesis it has proven unsuitable due to its specificity regarding the selection of regularization parameters $\lambda_{2,1}$ and λ_2, as it tends to converge rather quickly towards the trivial solution $a(r) = 0$ when the regularization parameters are too far off from ideal. Instead, for the scope of this thesis, the alternating direction method of multipliers (ADMM) algorithm has been utilized [70].

The ADMM algorithm is an iterative algorithm for solving multiplicative minimization problems of the following structure:

$$\begin{aligned}
\text{minimize:} \quad & f(x) + g(z) \\
\text{subject to} \quad & Ax + Bz = c
\end{aligned} \ , \tag{4.5}$$

with vectors $x \in \mathbb{R}^n$, $z \in \mathbb{R}^m$ and matrices $A \in \mathbb{R}^{p\times n}$, $B \in \mathbb{R}^{p\times m}$ and vector $c \in \mathbb{R}^p$. The photothermal SR reconstruction problem stated in Equation (2.78) can be split up accordingly into solving the least-squares minimization $f(a^m_{\text{rec}})$ and the regularization term $g_\lambda(a^m_{\text{rec}})$ as follows:

$$f(a^m_{\text{rec}}) = \frac{1}{2} \cdot \|\Phi_{\text{PSF}} *_r a^m_{\text{rec}} - T^m_{\text{diff}}\|_2^2 \tag{4.6}$$

$$g_\lambda(a^m_{\text{rec}}) = \lambda_{2,1} \cdot \|a^m_{\text{rec}}\|_{2,1} + \frac{\lambda_2}{2} \cdot \|a^m_{\text{rec}}\|_2^2 \ . \tag{4.7}$$

In conjunction with choosing $A = I$, $B = -I$ and $c = \vec{0}$ where I is the identity matrix this leads to the following special case of the ADMM algorithm:

$$\begin{aligned} \text{minimize:} \quad & f(x) + g_\lambda(z) \\ \text{subject to} \quad & x = z \end{aligned} \quad , \tag{4.8}$$

which directly resembles the photothermal SR minimization problem at hand. However, as the ADMM algorithm is defined for multiplicative minimization problems only, Equation (4.6) has to be transformed to a multiplicative form first. This can be achieved in several ways.

Within the scope of this thesis, two methods have been developed and are examined in detail. First, a special convolution matrix can be introduced into the problem in order to transform the necessary convolution into a matrix-vector multiplication (cf. Section 4.1.1). Second, a frequency-space based method making use of the FFT is explored (cf. Section 4.1.2). After the transformation to a multiplicative problem, the general problem $Ax = b$ is solved by applying the ADMM algorithm by performing the steps shown in Algorithm 4.1 over n_{iter} iterations.

Algorithm 4.1: Basic ADMM algorithm for solving regularized multiplicative minimization problems.

```
Input: $A \in \mathbb{R}^{p\times n}$, $b \in \mathbb{R}^p$, $\rho_{\text{ADMM}}$, $\lambda_{2,1}$, $\lambda_2$, $n_{\text{iter}} \in \mathbb{R}$
Output: $z \in \mathbb{R}^n$
begin
    $x_{(0)}, z_{(0)}, u_{(0)} \in \mathbb{R}^n \leftarrow$ initialize randomly
    for $k \leftarrow 1$ to $n_{iter}$ do
        $x_{(k+1)} \leftarrow \left(A^T A + \rho I\right)^{-1} \left(A^T b + \rho_{\text{ADMM}} \left(z_{(k)} - u_{(k)}\right)\right)$
        $z_{(k+1)} \leftarrow \text{prox}_{\lambda_{2,1}/\rho_{\text{ADMM}}, \lambda_2/\rho_{\text{ADMM}}} \left(x_{(k+1)} + u_{(k)}\right)$
        $u_{(k+1)} \leftarrow u_{(k)} + x_{(k+1)} - z_{(k+1)}$
return $z_{(k+1)}$
```

The ADMM algorithm requires as further user input a scalar penalty parameter $\rho_{\text{ADMM}} \in \mathbb{R}$. This penalty parameter makes a trade-off between the influence of the minimization of $f(x)$ and the regularizers $g_\lambda(z)$ within the ADMM algorithm. While a suitable value for ρ_{ADMM} has to be provided by the user for every inversion problem, there exist ways of determining ρ_{ADMM} from the measured data directly (e.g., the L-curve method [71, 72]).

Within the ADMM algorithm, three main steps are performed at each iteration:

- $f(x)$ is minimized using Tikhonov-regularization with ρ_{ADMM} as the regularization parameter (x-update).
- $g_\lambda(z)$ is minimized using its proximal operator prox_λ (z-update).
- A minimization step u is computed from the new x and z to advance the algorithm.

Table 4.1: Proximal operators for a set of common regularization tasks: in order to minimize a regularized function, the corresponding proximal operator for the regularization used has to be minimized as well [73].

Regularization		**Proximal Operator**
Name	Norm	$\text{prox}_\lambda\left(x(r)\right)$
ℓ_1 (Lasso)	$\lambda_1 \|x\|_1$	$\text{sign}\left(x(r)\right) \cdot \max\left\{0,\ \lvert x(r)\rvert - \lambda_1\right\}$
ℓ_2 (Tikhonov)	$\frac{\lambda_2}{2}\|x\|_2^2$	$\left(1 - \frac{\lambda_2}{\max\{\|x(r)\|_2, \lambda_2\}}\right) x(r)$
$\ell_{2,1}$ (Block Sparsity)	$\lambda_{2,1}\|x\|_{2,1}$	$\max\left\{0,\ 1 - \frac{\lambda_{2,1}}{\sqrt{\sum_{m=1}^{n_m} \lvert x^m(r)\rvert^2}}\right\}$
$\ell_1 + \ell_2$ (Elastic Net)	$\lambda_1\|x\|_1 + \frac{\lambda_2}{2}\|x\|_2^2$	$\frac{1}{1+\lambda_1\lambda_2} \cdot \text{prox}_{\lambda_1\|\cdot\|_1}\left(x(r)\right)$

While the minimization of $f(x)$ is quite straightforward as it boils down to solving a set of linear equations, $g(z)$ must be solved using its proximal operator. A proximal operator is a functional approximation of the regularizer that, when evaluated iteratively, converges to a solution that satisfies the constraints imposed by the regularizer itself. A collection of proximal operators for common regularizers can be found in Table 4.1. Serendipitously, proximal operators feature the useful property that their effect can be combined by composition. This means that the proximal operator of the 2,1-norm $\text{prox}_{\|\cdot\|_{2,1}}$ can be calculated by $\text{prox}_{\|\cdot\|_1}\left(\text{prox}_{\|\cdot\|_2}\right)$ [74].

4.1.1 Sparse Matrix Stacking

In order to deal with the discrete nature of the spatial resolution of thermographic temperature measurements, the ROI has to be considered in discrete coordinates. This can be achieved by the following discretization:

$$r = \{(i \cdot \Delta x, j \cdot \Delta y) \in \mathbb{R}^{n_x \times n_y} \qquad \forall\, i \in \{0, \ldots, n_x - 1\}, j \in \{0, \ldots, n_y - 1\}\} , \tag{4.9}$$

where Δx, and Δy respectively, is the spatial sampling period. In total, this leads to a set of discrete two-dimensional coordinates containing $|r| = n_x \times n_x = n_r$ elements. Crucial in this context is the fact that this discretization into a single coordinate r allows reducing the dimensionality of the underlying problem, as it acts as a vectorization operation where all spatially resolved quantities are reduced from two-dimensions (x, y-matrix) into a single dimension (r-vector).

By reducing the dimensionality, it is now possible to perform linear convolution for solving the photothermal SR reconstruction problem utilizing a convolution matrix $h(\Phi_{\text{PSF}})$. As linear convolution can be considered as a linear mapping, $h(\Phi_{\text{PSF}})$ can be directly inferred by discretizing the specific convolution operation with Φ_{PSF} at hand as follows:

$$\begin{aligned}
& & \Phi_{\text{PSF}}(r) *_r \ a^m(r) &= T^m_{\text{diff}}(r) \\
&\overset{\text{def.}}{\Rightarrow} & \int_r \Phi_{\text{PSF}}(\rho) \cdot a^m(r - \rho)\, \mathrm{d}\rho &= T^m_{\text{diff}}(r) \\
&\overset{\text{discretize}}{\Rightarrow} & \sum_{k=-\infty}^{\infty} a^m[k] \cdot \Phi_{\text{PSF}}[r - k] &= T^m_{\text{diff}}[r]
\end{aligned}$$

$$\Rightarrow \underbrace{\begin{bmatrix}
\Phi_{\text{PSF}}[0] & 0 & \cdots & 0 & 0 \\
 & \Phi_{\text{PSF}}[0] & & \vdots & \vdots \\
\vdots & & \ddots & 0 & \\
 & & & \Phi_{\text{PSF}}[0] & 0 \\
 & \vdots & & & \Phi_{\text{PSF}}[0] \\
\Phi_{\text{PSF}}[n_r-1] & & \ddots & & \\
0 & \Phi_{\text{PSF}}[n_r-1] & & \vdots & \\
\vdots & 0 & \ddots & & \vdots \\
 & \vdots & & \Phi_{\text{PSF}}[n_r-1] & \\
0 & 0 & \cdots & 0 & \Phi_{\text{PSF}}[n_r-1]
\end{bmatrix}}_{h(\Phi_{\text{PSF}})[s,r]} \underset{\cdot}{\cdot} \underbrace{\begin{bmatrix} a^m[0] \\ \vdots \\ a^m[n_r-1] \end{bmatrix}}_{a^m[r]} \underset{=}{=} \underbrace{\begin{bmatrix} 0 \\ \vdots \\ T^m_{\text{diff}}[0] \\ \vdots \\ T^m_{\text{diff}}[n_r-1] \\ \vdots \\ 0 \end{bmatrix}}_{T^m_r[s]} , \tag{4.10}$$

with $h : \mathbb{R}^{n_r} \to \mathbb{R}^{2n_r-1}$, $T^m_r \in \mathbb{R}^{2n_r-1}$ and $s \in \{0, \ldots, 2n_r - 2\}$, where T^m_r is T^m_{diff} symmetrically padded with zeros. $h(\Phi_{\text{PSF}})$ forms a Toeplitz matrix with a high degree of sparsity (only 50% of its values are non-zero for $n_r \to \infty$). In short, making use of the convolution matrix $h(\Phi_{\text{PSF}})$ constitutes the following transformation:

$$\Phi_{\text{PSF}}(r) *_r \ a^m(r) = T^m_{\text{diff}}(r) \quad \Rightarrow \quad h(\Phi_{\text{PSF}})[s, r] \cdot a^m[r] = T^m_r[s] , \tag{4.11}$$

which transforms the original linear convolution problem into a multiplicative form suitable to be solved by the ADMM algorithm. However, Equation (4.11) only solves the photothermal

SR problem for a single measurement m. In order to interconnect the information provided by the individual measurements and to make use of the joint-sparsity exploited by the $\ell_{2,1}$-regularization, all measurements have to be solved in unison. As the problem has been reduced to solving a linear set of equations, a combination can be achieved by stacking all measurement as follows:

$$H \cdot A = \begin{bmatrix} \boxed{h(\Phi_{\mathrm{PSF}})} & \cdots & \vec{0} \\ \vdots & \boxed{h(\Phi_{\mathrm{PSF}})} & \vdots \\ \vec{0} & \cdots & \boxed{h(\Phi_{\mathrm{PSF}})} \end{bmatrix} \cdot \begin{bmatrix} a^0 \\ \vdots \\ a^{n_m - 1} \end{bmatrix} = \begin{bmatrix} T_r^0 \\ \vdots \\ T_r^{n_m - 1} \end{bmatrix} = T_R \ , \tag{4.12}$$

where $H \in \mathbb{R}^{(2n_r - 1)\cdot n_m \times n_r \cdot n_m}$, $A \in \mathbb{R}^{n_r \cdot n_m}$ and $T_r \in \mathbb{R}^{(2n_r-1)\cdot n_m}$. The matrix H is a block-diagonal matrix with blocks of $h(\Phi_{\mathrm{PSF}})$ on its main diagonal. This makes it even sparser than $h(\Phi_{\mathrm{PSF}})$ itself, as only $^1/_{2n_m}$ elements of the matrix are non-zero for $n_r \to \infty$. While compared to the initial problem the dimensionality of H, which features in total $n_m^2 \cdot (2n_r^2 - n_r)$ elements compared to n_r elements initially, is by far larger, its pronounced sparsity keeps it still manageable with reasonable hardware. Its properties can be exploited by utilizing the sparsity to significantly improve the algorithmic complexity of the matrix-vector multiplication problem stated in Equation (4.12), which naïvely would be determined as $\mathcal{O}\left((2n_r - 1)^2 \cdot n_r \cdot n_m^3\right)$. However, quantifying the performance gain by exploiting the sparsity is not trivially possible as it depends heavily on the details of the implementation [75].

In summary, the sparse matrix stacking approach solves the photothermal SR reconstruction problem via solving the following adapted minimization problem:

$$\text{minimize:} \quad ^1/_2 \cdot \|H \cdot A - T_R\|_2^2 + \lambda_{2,1} \cdot \|A\|_{2,1} + \lambda_2 \cdot \|A\|_2^2 \ . \tag{4.13}$$

For solving Equation (4.13) using the ADMM algorithm, the specific algorithm presented in Algorithm 4.2 has been developed. While overall this algorithm follows the presented scheme from Algorithm 4.1, applying the regularization by means of the corresponding proximal operator is not as straightforward, since the stacking operation has introduced discontinuities in the data representation. In order to properly apply the proximal operator, the data needs to be reshaped into its original form ($\mathbb{R}^{n_r \cdot n_m} \to \mathbb{R}^{n_r \times n_m}$) beforehand. After applying the proximal operator, the data has to be reshaped back.

One of the major advantages of the sparse matrix stacking approach lies in the fact that while solving Equation (4.13) can be quite computationally expensive for large n_r, it is quite easy to dissect the problem by splitting the matrix-vector multiplication row-wise into smaller parts. As the computational complexity of the algorithm scales with $\propto {n_r}^3$, this can lead to a major improvement in processing time. Splitting the problem row-wise into parts resembles reconstructing multiple sub-ROIs. However, to not interfere with the joint-sparse nature of the problem, the data needs to be split such that for every coordinate r contained in the subproblem, all data from the corresponding measurements n_m is included within. After applying the algorithm presented in Algorithm 4.2, the reconstruction of the internal defect structure can be obtained by summing over all measurements. Finally, in order to get rid of any offsets and to make different reconstructions comparable to each other, the reconstruction result is normalized by applying a normalization function $\psi : \vec{x} \in \mathbb{R}^{n_r} \rightarrow [0,1]^{n_r}$ as follows:

Algorithm 4.2: Sparse Matrix Stacking Reconstruction.

```
Input: $H \in \mathbb{R}^{(2n_r-1)\cdot n_m \times n_r\cdot n_m}$, $T_R \in \mathbb{R}^{(2n_r-1)\cdot n_m}$
       $\rho_{\text{ADMM}},\ \lambda_{2,1},\ \lambda_2,\ n_{\text{iter}} \in \mathbb{R}$
Output: $z \in \mathbb{R}^{n_r\cdot n_m}$

function $\text{prox}_{\ell_{21}+\ell_2}(l,\ \lambda_{2,1},\ \lambda_2)$:
    $p[r,m] \leftarrow \max\left(0, 1 - \frac{\lambda_{2,1}}{\sqrt{\sum_{m=1}^{n_m} |l[r,m]|^2}}\right)\frac{l[r,m]}{1+\lambda_2}$
    return $p$
begin
    $x_{(0)}, z_{(0)}, u_{(0)} \in \mathbb{R}^{n_r\cdot n_m} \leftarrow$ initialize randomly
    for $k \leftarrow 1$ to $n_{iter}$ do
        $x_{(k+1)} \leftarrow \left(H^T H + \rho I\right)^{-1}\left(H^T T_R + \rho(z_{(k)} - u_{(k)})\right)$
        $l_{(k+1)} \leftarrow$ reshape $x_{(k+1)} + u_{(k)}$ to $\mathbb{R}^{n_r \times n_m}$
        $p_{(k+1)} \leftarrow \text{prox}_{\ell_{21}+\ell_2}(l_{(k+1)},\ \lambda_{2,1}/\rho_{\text{ADMM}},\ \lambda_2/\rho_{\text{ADMM}})$
        $z_{(k+1)} \leftarrow$ reshape $p_{(k+1)}$ to $\mathbb{R}^{n_r\cdot n_m}$
        $u_{(k+1)} \leftarrow u_{(k)} + x_{(k+1)} - z_{(k+1)}$
    return reshape $z_{(k+1)}$ to $\mathbb{R}^{n_r \times n_m}$
```

$$a_{\text{rec}}(r) = \psi\left(\sum_{m=1}^{n_m} z^{m}_{(n_{\text{iter}})}(r)\right) \qquad \text{, with} \tag{4.14}$$

$$\psi(\vec{x}) = \frac{\vec{x} - \min(\vec{x})}{\max(\vec{x}) - \min(\vec{x})} \ . \tag{4.15}$$

The reconstruction $a_{\text{rec}}(r)$ then resembles a map of all internal defects/inhomogeneities. All coordinates r where $a_{\text{rec}}(r) > 0$ are detected defective by the algorithm. The absolute value of r indicates the relative contrast of the defects.

4.1.2 Inversion in Frequency Space

While the previously shown sparse matrix approach already leads to good reconstruction results (cf. Section 5.2.2), its high computational complexity has proven to be a major bottleneck for performing photothermal SR reconstruction. Therefore, a more performant method has been developed in the course of the thesis, which makes use of linear convolution in frequency space. As has already been shown in Equation (4.4), circular convolution can be achieved by element-wise multiplication in the frequency domain. However, photothermal SR reconstruction requires linear convolution, which can be achieved by reordering the data first. A refined numerical way to perform linear convolution by multiplication in frequency space is as follows:

$$\Phi_{\mathrm{PSF}}(r) \ *_r \ a^m(r) = T^m_{\mathrm{diff}}(r) \ \Rightarrow \ \mathrm{ifft}\left(\overline{\mathrm{fft}\left(\mathrm{ifftshift}\left(\Phi_{\mathrm{PSF}}[r]\right)\right)} \odot \mathrm{fft}\left(a^m[r]\right) = T^m_{\mathrm{diff}}[r]\right) \ , \tag{4.16}$$

where fft$(\cdot)$ is the FFT function in r, ifft$(\cdot)$ its inverse and the overline indicates complex conjugation. The additionally applied shifting function ifftshift : $\mathbb{R}^{m,n} \to \mathbb{R}^{m,n}$ rearranges its input data such that it swaps the first quadrant with the third, and the second quadrant with the fourth.

Since the ADMM algorithm expects a matrix-vector multiplication problem instead of an element-wise multiplication, Equation (4.16) has to be further transformed by diagonalizing it as follows:

$$\begin{aligned} &\mathrm{ifft}\left(\overline{\mathrm{fft}\left(\mathrm{ifftshift}\left(\Phi_{\mathrm{PSF}}[r]\right)\right)} \odot \mathrm{fft}\left(a^m[r]\right)\right) \Rightarrow \\ &\qquad\qquad \mathrm{ifft}\left(\mathrm{diag}\left(\overline{\mathrm{fft}\left(\mathrm{ifftshift}\left(\Phi_{\mathrm{PSF}}[r]\right)\right)}\right) \cdot \mathrm{fft}\left(a^m[r]\right)\right) \ . \end{aligned} \tag{4.17}$$

The resulting matrix $\mathrm{diag}\left(\overline{\mathrm{fft}\left(\mathrm{ifftshift}\left(\Phi_{\mathrm{PSF}}[r]\right)\right)}\right) \in \mathbb{R}^{n_r \times n_r}$ is a diagonal matrix with elements only on the main diagonal. While this property makes it efficient to store and invert, as the inverse can be obtained by element-wise taking the reciprocal value, it also leads to significantly altered matrix properties (singular values, eigenvectors, rank etc.) compared to the non-diagonalized version, which certainly affect the convergence of the later applied optimization step to solve the photothermal SR problem. As with the sparse matrix stacking approach discussed in the previous section, in order to take all the measurements into account and exploit common features within them, the measurements are stacked on top of each other to be solved in unison.

An important aspect to note when performing the necessary convolution operation in frequency space is that while the minimization algorithm can be performed fully in frequency space for the most part, applying the regularizers by means of their proximal operator is not feasible in frequency space. Since the main use of the regularizers is to promote certain properties of the solution (sparsity, small 2-norm), these properties do not persist the transformation into frequency space. This can be clearly visualized by taking a look at a single Dirac-pulse, which features a very high sparsity. However, after transforming it into frequency space, the resulting function has overall constant value, which is quite the opposite of sparse. Therefore, it is only really valid to apply any regularization outside the frequency space adding an additional fft and ifft operation to the algorithm. In total, this leads to the algorithm presented in Algorithm 4.3. The resulting complexity of the frequency space inversion is given by $\mathcal{O}\left(n_r \cdot n_m \cdot \log(n_r \cdot n_m)\right)$.

Algorithm 4.3: Frequency Domain Reconstruction.

```
Input: $\Phi_{\text{PSF}}, T_{\text{diff}} \in \mathbb{R}^{n_r \times n_m}$,    $\rho_{\text{ADMM}}, \lambda_{2,1}, \lambda_2, n_{\text{iter}} \in \mathbb{R}$
Output: $z \in \mathbb{R}^{n_r \times n_m}$

function $\text{prox}_{\ell_{21}+\ell_2}(l,\ \lambda_{2,1},\ \lambda_2)$:
    $p[r,m] \leftarrow \max(0, 1 - \frac{\lambda_{2,1}}{\sqrt{\sum_{m=1}^{n_m} |l[r,m]|^2}}) \frac{l[r,m]}{1+\lambda_2}$
    return $p$

begin
    $A \leftarrow \text{diag}\left(\text{reshape}\ \overline{\text{fft}\,(\text{ifftshift}\,(\Phi_{\text{PSF}}))}\ \textbf{to}\ \mathbb{R}^{n_r \cdot n_m}\right)$
    $b \leftarrow \text{reshape}\ \text{fft}(T_{\text{diff}})\ \textbf{to}\ \mathbb{R}^{n_r \cdot n_m}$
    $x_{(0)}, z_{(0)}, u_{(0)} \in \mathbb{R}^{n_r \cdot n_m} \leftarrow$ initialize randomly
    for $k \leftarrow 1$ to $n_{iter}$ do
        $x_{(k+1)} \leftarrow (A^T A + \rho I)^{-1}(A^T b + \rho(z_{(k)} - u_{(k)}))$
        $l_{(k+1)} \leftarrow \text{ifft}\left(\text{reshape}\ x_{(k+1)} + u_{(k)}\ \textbf{to}\ \mathbb{R}^{n_r \times n_m}\right)$
        $p_{(k+1)} \leftarrow \text{prox}_{\ell_{21}+\ell_2}(l_{(k+1)},\ \lambda_{2,1}/\rho_{\text{ADMM}},\ \lambda_2/\rho_{\text{ADMM}})$
        $z_{(k+1)} \leftarrow \text{reshape}\ \text{fft}(p_{(k+1)})\ \textbf{to}\ \mathbb{R}^{n_r \cdot n_m}$
        $u_{(k+1)} \leftarrow u_{(k)} + x_{(k+1)} - z_{(k+1)}$
    return $\text{ifft}\left(\text{reshape}\, z_{(k+1)}\ \textbf{to}\ \mathbb{R}^{n_r \times n_m}\right)$
```

After applying the frequency space inversion algorithm, as shown in Algorithm 4.3, the reconstruction result $a_{\text{rec}}(r)$ can be obtained by summing over all measurements and subsequent normalization as already laid out before in Equation (4.14).

4.2 Experimental Implementation

In order to make use of the two-dimensional SR capabilities of the two inversion algorithms introduced in Section 4.1, the experimental approach of photothermal SR reconstruction has to be adapted accordingly. In the following sections, two different adaptations of the experimental approach are discussed.

4.2.1 Sequential Laser Scanning

The first experimental approach designed within the scope of this thesis is based on the extension of the already existing laser step-scanning approach for the one-dimensional subproblem introduced by Ahmadi et al. [64]. In the one-dimensional case, the most accurate illumination strategy has proven to be the step-wise subsequent illumination of the ROI with a laser line or an array of lines [A4]. In order to transform this approach so that it is capable of achieving SR in two dimensions, the line-wise illumination has to be interchanged with a spot-wise heating of the ROI as shown in Figure 4.1.

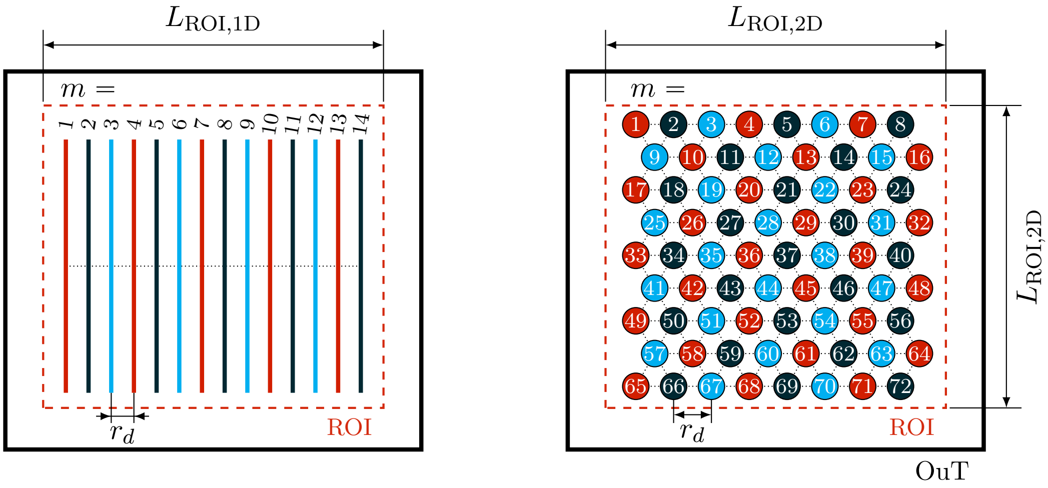

(a) Line-wise illumination of a one-dimensional ROI. Only the resolution of vertically oriented defects is improved.

(b) Point-wise illumination of a two-dimensional ROI using an equidistant measurement grid.

Figure 4.1: Necessary transformation of the illumination strategy for sequential laser scanning: the well-established step scanning with a laser line (left) provides only one-dimensional SR capabilities for defects parallel to the laser lines. In order to achieve a fully two-dimensional SR reconstruction, also the illumination pattern needs to be structured in two dimensions. This can be achieved by point-wise illumination with an equidistant measurement grid (right).

Illumination Strategy

If for the one-dimensional SR reconstruction case an ROI with a length of $L_{\mathrm{ROI,1D}}$ has to be investigated, then the number of measurements necessary to cover the ROI with an equidistant measurement grid with a grid spacing r_d can be calculated as follows:

$$n_{m,\mathrm{1D}} = \left\lfloor \frac{L_{\mathrm{ROI,1D}}}{r_d} \right\rfloor \tag{4.18}$$

If now the method is expanded to yield fully two-dimensional SR capabilities, then instead of a linearly arranged grid of line illuminations an equidistantly two-dimensional grid of point-like illuminations has to be chosen. In total, this leads to a grid arrangement forming equilateral triangles between the different measurement positions. The number of measurements necessary to span a square ROI with side length $L_{\mathrm{ROI,2D}}$ can then be calculated as follows:

$$n_{m,\mathrm{2D}} = \left\lfloor \frac{\sqrt{3}}{2} \cdot \frac{L^2_{\mathrm{ROI,2D}}}{r_d^2} \right\rfloor \tag{4.19}$$

As can be directly observed from Equation (4.18) and Equation (4.19), the number of measurements necessary scales with the size of the ROI. While there is a linear relationship in the one-dimensional case with $n_{m,\mathrm{1D}} \propto L_{\mathrm{ROI,1D}}$, in the two-dimensional n_{m} scales quadratically with the side length of the ROI with $n_{m,\mathrm{2D}} \propto L^2_{\mathrm{ROI,2D}}$. This means that when a similar ROI is to be investigated using two-dimensional SR reconstruction compared to the established one-dimensional variant, the necessary number of measurements (and therefore also the measurement effort/complexity) increases quadratically:

$$\frac{n_{m,\mathrm{2D}}}{n_{m,\mathrm{1D}}} \approx \frac{\sqrt{3}}{2} \cdot \frac{L^2_{\mathrm{ROI,2D}}}{L_{\mathrm{ROI,1D}} \cdot r_d} \tag{4.20}$$

$$\overset{L_{\mathrm{ROI,1D}} \approx L_{\mathrm{ROI,2D}}}{\Rightarrow} \quad n_{m,\mathrm{2D}} \approx \frac{\sqrt{3}}{2} \cdot n^2_{m,\mathrm{1D}} \ . \tag{4.21}$$

In practice this means that if an ROI has been measured using $n_{m,\mathrm{1D}} = 200$ one-dimensional illuminations with a laser line, in order to achieve a two-dimensional reconstruction of the same square ROI, $n_{m,\mathrm{2D}} \approx 34641$ point-wise illuminations are necessary, if the grid spacing r_d is kept constant. As this is an exorbitant number, it should be clear that for two-dimensional reconstruction, a coarser measurement grid must be adopted. In turn this also leads to a presumably worse maximum possible reconstruction quality in the two-dimensional case.

Nevertheless, in order to keep the resulting measurement efforts manageable, the other leverage that exists on the resulting number of measurements to be performed – namely increasing the grid spacing – has to be made use of. However, in order to also fulfill the homogeneity requirement for photothermal SR reconstruction as stated in Equation (2.74), there exists an upper limit for the maximum grid spacing. Fortunately, as the PSFs of the individual illuminations have to overlap and not only the measurement positions themselves, the homogeneity of the illumination pattern in total is also dependent on the evaluation time t_eval, as the width of the thermal PSF is time-dependent. This leads to the following requirement for the grid spacing r_d:

$$r_d \leqslant 2\sqrt{2\alpha}\cdot\sqrt{t_\text{eval}} \qquad \Leftrightarrow \qquad r_d \leqslant 2\sqrt{2}\cdot L_\text{diff}\ . \tag{4.22}$$

For a detailed derivation of Equation (4.22) see Appendix A3. Equation (4.22) shows that the necessary grid spacing can be increased (and therefore the necessary number of measurements decreased) by evaluating the acquired thermographic data at a later time step. While this sounds promising for decreasing the experimental complexity, one has to keep in mind that the recorded temperature signal drops off over time with $T_\text{diff} \propto t_\text{eval}^{-3/2}$ for three-dimensional heat flow and therefore also the achievable SNR. As a result, this effect sets a hard limit to the evaluation time and therefore the maximum reasonable grid spacing. The trade-off necessary is further illustrated in Figure 4.2.

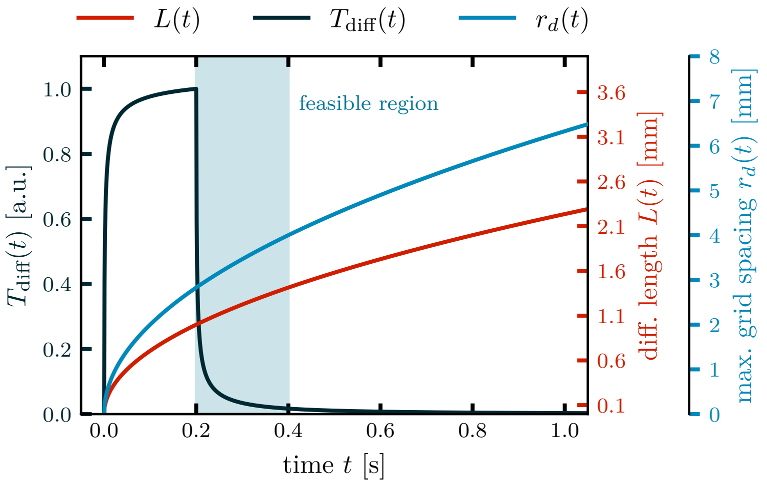

Figure 4.2: Selection of the optimal measurement grid spacing. While ideally the grid spacing r_d should be as small as possible in order to achieve the best reconstruction results, small values severely increase the necessary experimental efforts. Therefore, one has to make a trade-off between the penetration depth (diffusion length L) and the measurement's SNR (T_diff) by choosing a suitable evaluation time t_eval. The temperature evolution shown has been calculated for $\alpha = 5\,\text{mm}^2/\text{s}$ and $t_\text{pulse} = 0.2\,\text{s}$.

4.2.2 Two-dimensional Pattern Projection

While the previously discussed experimental method of sequentially illuminating an ROI using n_m different point-wise illumination patterns already leads to good results, its experimental complexity and therefore the necessary measurement times are very high, making the method impractical for most industrial applications. In order to eliminate this shortcoming, a different illumination approach has been developed during the course of this thesis.

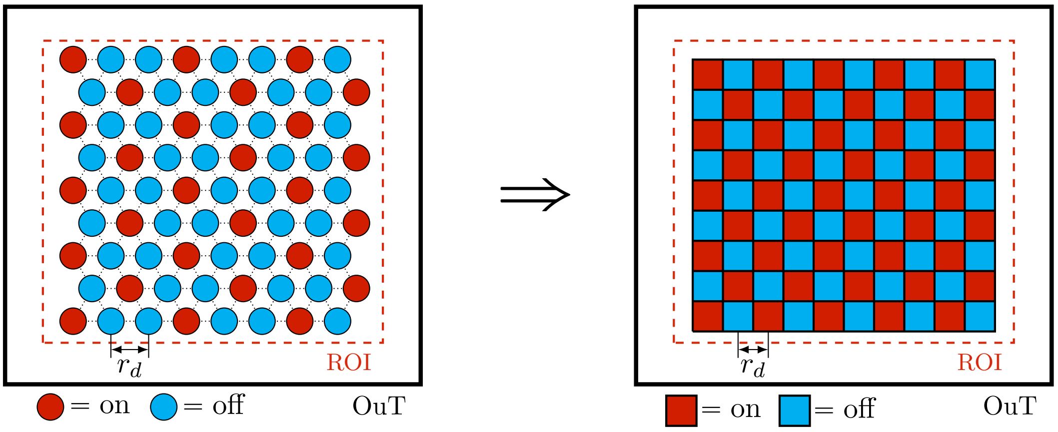

(a) Point-wise illumination with multiple laser spots. All red colored positions are illuminated simultaneously.

(b) Abstraction of the multiple spot illumination onto a regular rectangular grid leading to a binary pixelated pattern of measurement positions.

Figure 4.3: Multiple simultaneous illuminations and measurement grid abstraction: the sequential scanning experimental approach can be accelerated by illuminating multiple positions at once (left). As generating multiple individually steerable laser spots is non-trivial, the overall process can be abstracted onto a regular rectangular grid allowing the use of projector technology to generate binary pixelated patterns instead.

From the sequential point-wise illumination of the ROI can be observed that each single illumination only affects a small region of the ROI while the rest of the ROI is not affected. This can be utilized, as multiple illuminations can be performed simultaneously as long as they are far enough apart to not influence each other ($\gg \text{FWHM}(\Phi_{\text{PSF}})$). In the limit, combining multiple point-wise illuminations into a single measurement leads to the projection of a binary pixelated pattern where every measurement position that is illuminated can be considered activated (photothermally active or boolean `1`), or deactivated (photothermally inactive or boolean `0`). As combining multiple illumination spots that are independently steerable is experimentally non-trivial, the resulting binary measurement grid can be transformed into a regular rectangular grid. This allows using modern projector technology to experimentally implement the projection of such patterns as is discussed in detail in Section 5.3.1. The experimental approach is further illustrated in Figure 4.3.

For photothermal SR reconstruction to work, still multiple of those illumination patterns have to be projected. However, as every individual measurement already contains information over a large fraction of the ROI, the amount of measurements necessary is drastically reduced. While for the sequential laser scanning an full matrix capture (FMC) approach needs to be followed, meaning that every measurement position has to be measured individually, for the pattern projection not all possible pattern combinations have to be investigated in order to achieve a suitable reconstruction result. In this regard, the method follows a compressed sensing (CS) approach in order to minimize the experimental efforts, while still trying to achieve reasonable reconstruction results. The exact amount of measurements necessary is not easily determinable as it depends on a multitude of factors. A numerical assessment of the necessary amount of different patterns projected is laid out in Section 4.3.3.2.

Properties of Binary Illumination Patterns

The proposed illumination strategy to address the disadvantages of the sequential laser scanning approach consists of sequentially projecting a set of binary pixelated patterns. Each pattern forms a regular rectangular grid containing in total $n_{\text{pix,total}}$ individual addressable pixels. Within each pattern, $n_{\text{pix,on}}$ pixels out of the total $n_{\text{pix,total}}$ pixels are turned on (photothermally active). Therefore, for every pattern a fill factor $\beta \in [0, 1]$ can be specified, which describes the fraction of activated pixels over the total amount of pixels in the pattern:

$$\beta = \frac{n_{\text{pix,on}}}{n_{\text{pix,total}}} \,. \tag{4.23}$$

This fill factor is kept constant over all measurements n_m, while the exact set of activated pixels is altered with every measurement.

Each individual pixel is considered to be square with a side length of d_{pix}. However, it has proven useful to be able to artificially increase the pixel size by combining multiple neighboring pixels into a square pixel cluster in which every constituent pixel is activated in unison. This clustering has the effect that with the pixel size the conveyed optical power is increased, as mostly the total optical power delivered by the pattern is fixed, but it then distributes over a smaller number of clusters. When clustering $n_{\text{clustered}} \times n_{\text{clustered}}$ pixels together, the resulting pixel cluster has a size of $d_{\text{spix}} = n_{\text{clustered}} \cdot d_{\text{pix}}$. As a result, the conveyed power per pixel increases from $\hat{Q}_{\text{total}}/n_{\text{pix,total}}$ to $\hat{Q}_{\text{total}} \cdot n^2_{\text{clustered}}/n_{\text{pix,total}}$, while the total number of individual addressable pixels decreases by a factor of $1/n^2_{\text{clustered}}$. As all constituent pixels of any pixel cluster act in unison, the fill factor β is not affected by the clustering. Conversely, clustering too many pixels together has also adverse effects on the reconstruction quality. If the pixels become too large there will be no three-dimensional heat flow at their projected center, thus invalidating the PSF assumed for the reconstruction step. This effect is further studied in Section 4.3.3.1.

A visual representation of the different properties of a binary pixelated illumination pattern, as described before, can be found in Figure 4.4.

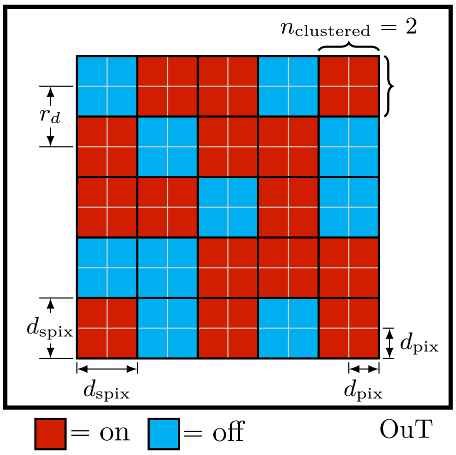

Figure 4.4: Schematic depiction of a binary pixelated illumination pattern and its properties: the shown pattern features a 10 × 10 grid pattern of individual pixels. Neighboring pixels are clustered together ($n_{\text{clustered}} = 2$) to form a 5 × 5 grid of pixel clusters increasing the conveyed optical power per pixel cluster by a factor of 4. The pattern features a fill factor of $\beta = 0.6$.

Illumination Pattern Generation

In order to generate a suitable set of n_m binary pixelated patterns a^m_{pattern}, within the scope of this thesis, a pseudo-random generation approach has been developed. In general, the illumination patterns need to fulfill two requirements. Firstly, summing over the set of patterns has to lead to a constant uniform value as it is fundamentally required for photothermal SR reconstruction (cf. Equation (2.74)), and secondly, the projection of those patterns should generate the maximum amount of information about the internals of the OuT without introducing any artifacts. While the homogeneity constraint can be fulfilled by a vast amount of possible pattern generation methods, the amount of added information content about the OuT per individual pattern projection is not trivially determinable. However, one can make use of the experience gained within the field of CS, which shows that it is beneficial to minimize the coherence of the measurement matrix (here the illumination patterns) to achieve the best possible reconstruction results for sparse signals. For a fixed fill factor β, generating a set of patterns containing $\beta \cdot n_{\text{pix,total}}$ randomly distributed activated pixels each will already minimize the coherence of the individual patterns. However, the homogeneity constraint is only fulfilled for such patterns if the number of projected patterns n_m is large, as due to the randomness involved homogeneity can only be guaranteed asymptotically. This property stands in stark contrast to the initial goal of the pattern projection approach to reduce the number of measurements necessary to a manageable minimum.

Algorithm 4.4: Pseudo-random pattern generation.

```
Input: $\beta \in \mathbb{Q}$, $n_{\text{pix,total}}$, $n_m \in \mathbb{N}$
Output: $a^m_{\text{pattern}} \in \{0,1\}^{n_{\text{pix,total}} \times n_m}$

function fill($x \in \{0\}^{n_{pix,total}}$, $n_{fill}$):
    $x \leftarrow x$ filled uniformly at random with at most $n_{\text{fill}}$ ones
    return $x$

begin
    $n_{\text{target}} \leftarrow \lceil \beta \cdot n_{\text{pix,total}} \rceil$
    $a^0_{\text{pattern}} \leftarrow [0, \ldots, 0]$
    $a^0_{\text{pattern}} \leftarrow$ fill$\left(a^0_{\text{pattern}},\ n_{\text{target}}\right)$
    for $m \leftarrow 1$ to $n_m - 1$ do
        $a^m_{\text{pattern}} \leftarrow [0, \ldots, 0]$
        $\text{share}_{\text{on}} \leftarrow 1/m \sum_{i=0}^{m} a^i_{\text{pattern}}$
        $\text{share}_{\text{on,low}} \leftarrow \arg\text{where}\,(\text{share}_{\text{on}} < \beta)$
        $a^m_{\text{pattern}}[\text{share}_{\text{on,low}}] \leftarrow$ fill$\left(a^m_{\text{pattern}}[\text{share}_{\text{on,low}}],\ n_{\text{target}}\right)$
        $n^m_{\text{pix,on}} \leftarrow \sum_{i=0}^{n_{\text{pix,total}}-1} a^m_{\text{pattern}}[i]$
        if $n^m_{pix,on} < n_{target}$ then
            $n_{\text{target,left}} \leftarrow n_{\text{target}} - n^m_{\text{pix,on}}$
            $a^m_{\text{pattern}}[\neg\text{share}_{\text{on,low}}] \leftarrow$ fill$\left(a^m_{\text{pattern}}[\neg\text{share}_{\text{on,low}}], n_{\text{target,left}}\right)$

    return $a^m_{\text{pattern}}$
```

Fulfilling the homogeneity constraint, even for a small number of measurements, requires a modified approach. For a fixed fill factor β and a fixed number of measurements n_m, a corresponding set of illumination patterns a^m_{pattern} is generated as follows. The first pattern is generated at random by randomly activating pixels until the desired fill factor is exactly reached. For the second pattern onwards, it is first checked which pixels need to be activated in order to fulfill the homogeneity requirement for the patterns generated so far. These pixels are then prioritized when randomly choosing which pixels to activate for this pattern. If no prioritized pixels are left, then the remaining pixels will be activated at random from the remaining deactivated subset of pixels for this pattern. This is repeated until all patterns are appropriately generated. The described algorithm can be considered an adaption of Bresenham's algorithm, which is a fundamental contribution to the field of drawing rasterized lines in computer graphics [76]. The described pattern generation approach is laid out algorithmically in Algorithm 4.4.

4.3 Numerical Modelling

The expansion of the photothermal SR reconstruction technique towards making use of fully two-dimensionally structured illumination patterns, either experimentally implemented with sequential scanning or pattern projection, introduces a vast space of experimental parameters to set up before performing any measurement. A non-exhaustive list of possible parameters influencing the method is given in Table 4.2. As the method relies on multiple measurements per reconstruction, experimental testing of a new set of parameters is quite costly. Therefore, it would be a significant step to be able to simulate the effects of the different parameters without performing any real-world measurements. This can be achieved by finding a forward solution to the inverse photothermal SR problem, which allows the user to create synthetic measurement data for a given set of experimental parameters. Furthermore, in order to judge if a given set of parameters results in an improvement of the method, automation of the reconstruction step is necessary to eliminate the need for manual tweaking of the regularization parameters necessary. Additionally, a suitable metric has to be found allowing the quantitative comparison of reconstructed defect maps in the first place in order even to be able to define what improvement in this context means.

Table 4.2: Experimental parameters of the presented photothermal SR reconstruction approach: each parameter can be varied to optimize the method and achieve the best results.

Category	Parameter	Symbol
Illumination	grid spacing	r_d
	number of measurements	n_m
	fill factor	β
	cluster size	d_{spix}
Defects	shape	d_{defect}
	separation distance	d_{sep}
	depth	L_{defect}
	contrast	ζ
OuT/PSF	material parameters	α, c_p, ρ
	evaluation time	t_{eval}
IR-camera	spatial resolution	$\Delta x, \Delta y$
	NETD	$\mathcal{N}_{\text{noise}}$

In the following chapter, these points are addressed by formulating a forward solution to the inverse reconstruction problem, defining a cost function that quantifies the reconstruction quality of defect maps and laying out an automation strategy for finding the (optimal) set of regularization parameters for a known reconstruction problem. Secondly, this then allows studying the influence of any experimental parameter on the method, which is used to exemplarily investigate the impact of the cluster size and number of measurements for random pattern excitation based photothermal SR reconstruction.

4.3.1 Forward Solution

The photothermal SR reconstruction problem constitutes a severely ill-posed inverse problem. As inverse problems deal with predicting the causal factors (here $a^m(r)$) that lead to a set of observations ($T^m_{\text{diff}}(r)$ in this context), finding a solution is a highly non-trivial task since the causing effects tend to be non-orthogonal/non-linearly independent and are therefore hard to separate. The inverse of the inverse problem, the so-called forward problem, on the other hand, takes a set of causal factors and calculates their effect. Thus, in order to formulate a forward solution to the photothermal SR reconstruction problem, the causal effects that cause a change in temperature of the OuT in the given context need to be modeled. Within the photothermal SR reconstruction context, two distinct effects have to be described: the effect of the external heating of a sound OuT and the deviations from that caused by the defects. For the case of the fundamental model of the photothermal SR reconstruction stated in Equation (2.71), this is done by appropriately defining the heat source distributions a^m_{ext} for the external heating and a^m_{int} for the defect interaction.

For the effect of the external heating on the sound OuT, the corresponding heat source distribution can be trivially generated as it is equivalent to the distribution of the external illumination itself:

$$a^m_{\text{ext}}(r) = a^m_{\text{illum}}(r) \; . \tag{4.24}$$

a^m_{illum} resembles either a single Dirac-pulse in r for the sequential laser scanning approach and a set of Dirac-pulses for the pattern projection approach, where every activated pixel is designated as a single impulse. Additionally, the spatial structure I_r of the heating primitive used (dot for sequential scanning; square for pattern projection) has to be considered within the PSF Φ_{PSF}.

For determining the contribution of the internal defects, finding a suitable heat source distribution function is not as easily possible. As already mentioned in Section 2.3.3, the effect of the internal defects on the temperature evolution of the OuT is tightly coupled to the external illumination as internal defects are no real heat sources themselves and only interfere with the internal heat flow in such a way that they can be treated as heat sources due to their apparent resemblance. Naïvely, the internal heat source distribution a_{int} can be modelled as the product of a known defect map $D(r) \in \{0,\, 1\}^{n_r}$, which indicates all coordinates where a defect is present by a value larger than zero, and a contrast factor $\zeta \in [0, 1[$, which models the strength of the effusivity contrast the defects introduce. Additionally, to model the dependency on the external heating, this now weighted defect map is combined with a normalized factor of $\psi\left(\Phi_{\text{PSF}}(r) *_r \; a^m_{\text{ext}}(r)\right)$ by element-wise multiplication:

$$a^m_{\text{int}}(r) = \zeta \cdot D(r) \odot \psi\left(\Phi_{\text{PSF}}(r) *_r \; a^m_{\text{ext}}(r)\right) \;, \tag{4.25}$$

where $\psi(\cdot)$ is the normalization function as defined in Equation (4.15). This additional factor acts as a spatial filter that attenuates the defect signal according to its distance to the actually heated area of the ROI. This is necessary, since the defects can only influence areas that are actually heated due to their sole ability of interfering with existing heat flows. The width of this spatial filter is chosen to be the PSF of the OuT, as it also governs the size of the thermal imprint the illumination generates. It has to be noted that adding this dependency on the external heat source distribution adds also a dependency on the exact measurement m as a^m_{ext} varies accordingly. This stands in stark contrast to the nature of the defects themselves as they are an inherent property of the OuT and therefore are unchanging. Combining the external and internal heat source distributions as described and inputting them into the basic model of photothermal SR reconstruction, leads to the following equation for generating synthetic measurement data $T^m_{\text{meas,sim}}(r, t)$:

$$\begin{aligned} T^m_{\text{meas,sim}}(r, t) = \Phi_{\text{PSF}}(r, t) *_r \; \Big[& a^m_{\text{ext}}(r) \\ & + \zeta \cdot D(r) \odot \psi\big(\Phi_{\text{PSF}}(r) *_r \; a^m_{\text{ext}}(r)\big)\Big] \\ & + T^m_0(r) + \mathcal{N}^m_{\text{noise}}(r) \;, \end{aligned} \tag{4.26}$$

where $T^m_0(r)$ is the temperature distribution at time $t = 0\,\text{s}$ and $\mathcal{N}^m_{\text{noise}}(r)$ is the measurement noise governed by the NETD of the simulated IR-camera. With Equation (4.26) it is now possible to generate arbitrary sets of measurement data for variations of the experimental parameters applicable as stated in Table 4.2. An experimental validation of the proposed forward solution can be found in Section 5.3.3.

4.3.2 Automatic Inversion Parameter Determination

While with the proposed forward solution, as stated in Equation (4.26), arbitrary measurement data can be generated with low computational effort in an analytical way, in order to fully automate the exploration of the parameter space for photothermal SR reconstruction also an automatic way to find the best set of regularization parameters needs to be found. Currently, the state-of-the-art process for finding the regularization parameters is still to determine them manually by trial and error. While with some prior training the time expenditure of this process can be reduced to a reasonable amount, it is still by far too slow to test larger parameter spaces.

The manual trial and error approach follows in principle two steps. First, a set of regularization parameters is guessed to serve as a candidate for the potential optimal set of regularization parameters leading to the optimal reconstruction result. Second, a reconstruction using these candidate values is obtained, and its quality is assessed qualitatively in comparison to previously obtained results. This process is repeated feeding back the information gained from previous iterations for guessing the next set of parameters until a satisfactory reconstruction result is obtained or no increase in reconstruction quality can be observed anymore. To automate the process in its entirety, the two sub-tasks of educated guessing an improved set of regularization parameters as well as judging the reconstruction quality in a quantitative way have to be automated.

Table 4.3: Candidate metrics for quantitatively comparing photothermal SR reconstruction results.

Name	**Description**	**Range**	**Ref.**
Normalized Mean Square Error (NMSE)	Pixel wise distance determination (ℓ_2-norm). Smaller values indicate higher similarity.	$[0, \infty[$	Eq. (4.27)
Intersection Over Union (IoU)	Fraction of correctly identified defective area and union of a_{rec} and D. Larger values indicate higher similarity.	$[0, 1]$	[77]
Structural Similarity (SSIM)	Perception based comparison based on statistical moments (amplitude, contrast, correlation). Larger values indicate higher similarity.	$]-\infty, 1]$	[78]
Custom Implementation	Weighted NMSE with included penalty function for false-positive detection depending on the distance to the next true positive defect. Smaller values indicate higher similarity.	$[0, \infty[$	Eq. (4.28)

Various strategies can be employed to quantitatively compare two reconstruction results. In this specific use case, the optimal result is known beforehand (ideally, the reconstructed image a_{rec} should directly resemble the defect map D). Hence, an assessment scheme that grades each reconstruction based on its similarity to the underlying defect map D is suitable. However, defining similarity in this context is challenging. Several metrics can be used to quantify the similarity between two different reconstruction results. A curated set is listed in Table 4.3.

The probably simplest metric to assess the quality of a reconstruction result is the normalized mean square error (NMSE) with respect to the known defect map. The NMSE calculates the ℓ_2-distance vectorially between the reconstruction and the defect map in a point-wise fashion as follows:

$$\mathrm{NMSE}\big(a_{\mathrm{rec}}(r),\, D(r)\big) = \frac{\|D(r) - a_{\mathrm{rec}}(r)\|_2^2}{\left\|D(r) - \overline{D(r)}\right\|_2^2} \; . \tag{4.27}$$

While the NMSE is widely used and easy to evaluate, it has limitations in evaluating photothermal SR reconstruction results. Specifically, it neglects any underlying structure in the defect map and performs poorly on sparse defect maps. Another commonly used metric is the intersection over union (IoU), which measures the fraction of correctly identified defective area over the total unified area spanned by the defects in the defect map and the reconstruction result [77]. However, like the NMSE, the IoU struggles to judge the convergence of reconstruction quality when starting with non-optimal guess values.

As the reconstruction result and the defect map can be interpreted as images, several image similarity metrics can be possibly applied. One popular metric is the structural similarity (SSIM), which compares pixel, contrast, and correlation values analytically [78]. Moreover, recent advancements in artificial intelligence (AI)-based methods for image similarity recognition can also be applied in this context [79]. These methods (SSIM and AI-based) focus more on detecting the underlying structure in the defect map and are less sensitive to minor disturbances. However, they may not be suitable for accurately quantifying reconstruction quality as they rely on a hardly quantifiable perception-based approach, which is similar to the manual qualitative comparison process performed by a human operator.

Knowing the advantages and disadvantages of the presented methods, for the scope of this thesis a custom metric has been developed. The proposed custom metric $C : a_{\mathrm{rec}} \to \mathbb{R} \in [0, \infty[$ assigns every reconstruction result a single number ranging from 0 to ∞, where a smaller number indicates a better reconstruction quality (i.e., a higher similarity with the underlying defect map D). It works by combining the NMSE between any reconstruction result a_{rec} and the defect map D with a location dependent penalty function that is used to improve convergence behavior. This metric is given as:

$$C\left(a_{\mathrm{rec}}(r)\right) = \mathrm{NMSE}\left(D(r), a_{\mathrm{rec}}(r)\right) + \left\|\left(1 - \psi\left(\eta(r)\right)\right) \odot a_{\mathrm{rec}}(r)\right\|_2 \; , \tag{4.28}$$

where $\psi(\cdot)$ is the normalization function as defined in Equation (4.15) and $1 - \psi\left(\eta(r)\right)$ is the penalization mask, which is added to the metric by element-wise multiplication with the reconstruction result a_{rec}. This penalization mask is used to continuously penalize false positive signals more that are further away from the true defect positions leading to a smoother metric function what the NMSE provides. The locality of this penalization is governed by the transition function $\eta(r)$, which makes again use of the thermal PSF Φ_{PSF} to incorporate the thermal properties into this metric. $\eta(r)$ is defined as follows:

$$\eta(r) = D(r) *_r \Phi_{\mathrm{PSF}}(r) \ . \tag{4.29}$$

With the custom metric defined in Equation (4.28) it is now possible to quantitatively compare reconstruction results. However, while the stated cost function has a clearly defined optimal value of $C(D) = 0$, it is hard to reason about the scaling of the metric (how much better is a reconstruction with $C(a_{\mathrm{rec}}) = 0.1$ compared to one with $C(a_{\mathrm{rec}}) = 1$?), as its absolute value is dependent on multiple factors. Therefore, the metric is best suited for relative comparisons only, which fits the proposed use case for the automated inversion of the photothermal SR reconstruction problem.

Now being able to quantify progress in determining the optimal set of regularization parameters for a given reconstruction problem, the missing part is still to automate searching through the parameter space. Finding the optimal set of regularization parameters Λ_{best} boils down to minimizing the applied comparison metric for a reconstruction obtained taking those parameters into account. This process can be formulated as the following minimization problem:

$$\Lambda_{\mathrm{best}} = \left\{\lambda_{2,1}^{\mathrm{best}},\ \lambda_2^{\mathrm{best}}\right\} = \underset{\lambda_{2,1},\,\lambda_2}{\arg\min}\ C\left(a_{\mathrm{rec}}(r)\right) \ . \tag{4.30}$$

For every guess value for Λ_{best}, the inverse photothermal SR reconstruction problem as defined in Equation (2.78) has to be solved in order to obtain a reconstruction result a_{rec}, making solving for the optimal set of regularization parameters exceptionally computationally expensive. Any method applied to solve it should therefore only take a very limited amount of trials in order to keep the computation time within feasible limits. In contrast, as the parameter space is quite large, non-linear and not necessarily convex with an unknown local derivative, these boundary conditions have to be considered as well.

For solving the minimization problem stated in Equation (4.30) the use of the differential evolution (DE) algorithm is proposed [80]. This heuristic search algorithm is well-suited for searching through vast parameter spaces and does not require a differentiable or even continuous search space.

The DE algorithm works by maintaining a population of candidate solutions, which are represented as vectors in a search space. Within DE, each candidate solution is updated using a differential operator, which generates new candidate solutions based on the differences between a set of randomly selected solutions. The algorithm then evaluates the solutions based on the provided comparison metric to evaluate the quality of each candidate solution and selects the best ones to generate new solutions in the next iteration. The key to the effectiveness of the DE algorithm is the differential operator, which generates new candidate solutions that are likely to be better than the current ones. This is achieved by creating new candidate solutions for the next generation by evaluating for each new candidate solution a scaled difference between two randomly selected solutions from the previous generation. This scaling factor controls the step-size for the iteration, and it is constantly adjusted during the search process to explore the search space more effectively. While this process shows good convergence behavior, it does not strictly guarantee reaching the global minimum (optimal solution). Therefore, it has to be ensured that the generation size is appropriately large such that convergence is likely [81, 82].

4.3.3 Photothermal Super Resolution Parameter Studies

With the previously discussed automatic inversion method for photothermal SR reconstruction problems with known defect map D it is now possible to gain insights into the dependency of the achievable reconstruction quality when different parameters of the experimental implementation are varied. For the case of two-dimensional random pattern illumination, the influence of clustering multiple pixels into larger pixel clusters with size d_{spix} as well as the influence of the conducted number of measurements n_m is simulated in the following sections. While in general the influence of most if not all experimental parameters as stated in Table 4.2 can be examined via numerical simulation, these two parameters have been chosen due to their direct significance on the main objective of this thesis, namely to minimize the experimental efforts necessary to perform a fully two-dimensional photothermal SR reconstruction of any ROI. Therefore, exactly knowing the minimum amount of measurements necessary (n_m) for a certain minimum reconstruction quality as well as getting an insight into the behavior of the pixelized pattern illumination approach (d_{spix}) is key and the scope of this thesis will be limited to the examination of those parameters only.

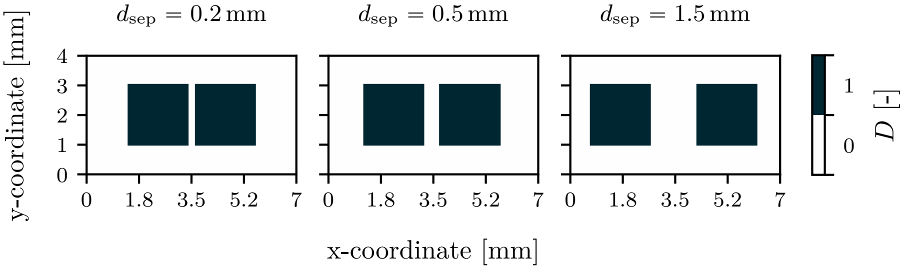

Figure 4.5: Defect map D to be used within the subsequent parameter studies on photothermal SR reconstruction with projected pixel patterns as illumination: three different defect maps containing a pair of $2\,\text{mm} \times 2\,\text{mm}$ wide defects with varying separation distances $d_{\text{sep}} \in \{0.2, 0.5, 1.5\}$ mm are investigated.

For both parameter studies, three different ROIs as shown in Figure 4.5 have been taken into account. Every ROI contains a pair of $2\,\text{mm} \times 2\,\text{mm}$ square defects at a separation distance d_{sep} of 0.2 mm, 0.5 mm and 1.5 mm respectively, featuring an even effusivity contrast of $\zeta = 0.3$.

The remaining experimental parameters shared for both parameter studies can be found in Table 4.4.

Table 4.4: Shared experimental parameters assumed for the subsequent parameter studies on photothermal SR reconstruction with pixel pattern illumination.

Category	Parameter	Value
OuT/PSF	thermal diffusivity	$\alpha = 3.76\,\mathrm{mm^2/s}$
	density	$\rho = 7950\,\mathrm{kg/m^3}$
	specific heat capacity	$c_p = 502\,\mathrm{J/(kg\,K)}$
	heating pulse duration	$t_{\text{pulse}} = 0.5\,\mathrm{s}$
Defects	shape	$d_{\text{defect}} = 2\,\mathrm{mm} \times 2\,\mathrm{mm}$
	separation distance	$d_{\text{sep}} \in \{0.2,\, 0.5,\, 1.5\}\,\mathrm{mm}$
	contrast	$\zeta = 0.3$
IR-camera	spatial resolution	$\Delta x, \Delta y = 0.1\,\mathrm{mm}$
	evaluation time	$t_{\text{eval}} = 0.5\,\mathrm{s}$
	NETD	$\mathcal{N}_{\text{noise}} = 5\% \cdot \max(T_{\text{diff}})$
Illumination	total pixels (x-direction)	$n_{\text{pix,x}} = 1280$
	total pixels (y-direction)	$n_{\text{pix,y}} = 800$
	pixel size on ROI	$d_{\text{pix}} = 20\,\mathrm{\mu m}$
ADMM	penalty parameter	$\rho_{\text{ADMM}} = 9900$
	$\ell_{2,1}$-regularization	$\lambda_{2,1} \in \,]0, 1000]$
	ℓ_2-regularization	$\lambda_2 \in \,]0, 2000]$
	iterations	$n_{\text{iter}} = 100$

4.3.3.1 Pixel Cluster Size

In order to determine the influence of the pixel size with two-dimensional pixel pattern illumination, the three ROIs presented in Figure 4.5 are investigated with patterns with varying square pixel cluster size of $d_{\text{spix}} \in \{0.02, 0.04, 0.08, 0.1, 0.16, 0.2, 0.32, 0.4, 0.64, 0.8, 1.6, 3.2\}$ mm performing $n_m = 50$ independent measurements each. This leads to a total of 36 photothermal SR problems to be solved for the three ROIs at 12 different pixel sizes. For each of the 36 photothermal SR problems, an optimal set of regularization parameters has been determined using the DE heuristic search algorithm and the quality metric as presented in Section 4.3.2. The specific parameters used can be found in Table 4.5.

As a result, the graph shown in Figure 4.6 has been obtained. Figure 4.6 shows the achieved reconstruction quality over the pixel cluster size d_{spix} in fractions of the defect size $d_{\text{defect}} = 2\,\mathrm{mm}$ for the three different ROIs. While it can be clearly observed that for larger separation distances the reconstruction quality increases, as can be expected since the aspect ratio γ_{sep} increases, the reconstructions in total show hardly any influence of the pixel size at all. However, the reconstruction quality suddenly increases when the pixel size matches the defect size and strongly decreases when the pixel size exceeds the defect size. From these results it can be concluded that clustering pixels can be used as a tool to increase the contained optical power per pixel for sufficiently heating materials with higher thermal diffusivity as long as the pixel cluster size does not exceed the minimum defect size to be resolved.

Table 4.5: Illumination parameters used for studying the influence of the number of pixels clustered together ($n_{\text{clustered}}$) on the reconstruction quality of photothermal SR reconstruction with pixel pattern illumination.

	Parameter	**Value**
Illumination Parameters	fill grade	$\beta = 0.5$
	number of measurements	$n_m = 50$
	separation distance	$d_{\text{sep}} \in \{0.2,\ 0.5,\ 1.5\}\,\text{mm}$
	cluster size	$n_{\text{clustered}} \in \{1,\ 2,\ 4,\ 5,\ 8,\ 10,\ 16,\ 20,\ 32,\ 40,\ 80,\ 160\}$
	pixel size	$d_{\text{spix}} \in \{0.02,\ 0.04,\ 0.08,\ 0.1,\ 0.16,\ 0.2,\ 0.32,\ 0.4,\ 0.64,\ 0.8,\ 1.6,\ 3.2\}\,\text{mm}$

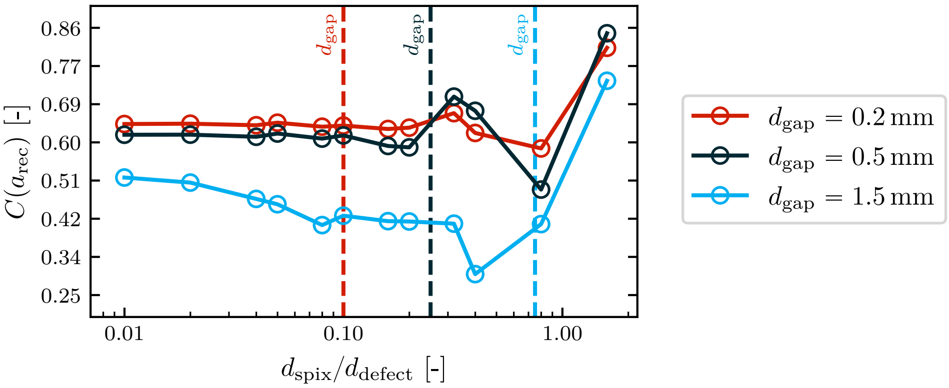

Figure 4.6: Study results on the dependence of the pixel cluster size on the reconstruction quality as measured by the quality metric $C(a_{\text{rec}})$ proposed in Equation (4.28) for three different defect separation distances. It can be observed that the reconstruction quality is not significantly affected by the cluster size as long as it stays below the defect size. A similar plot has already been published in [C4].

However, it has to be considered that for the underlying forward solution, which generated the synthetic measurement data in the first place, to be valid, the resulting heat flow induced by the illumination has to be three-dimensional. Therefore, there exists a physical limit to the maximum amount of clustered pixels to be sensible to still achieve an SR reconstruction, as is experimentally validated in Figure 5.3.3. Yet, this effect will not show in the numerical simulations conducted here, as the validity of the used PSF is assumed as a prior. This circumstance emphasizes the importance of experimental validation of any numerical simulation conducted.

In order to bring the loss of reconstruction quality that can be observed for cluster sizes larger than the defect size into perspective, Figure 4.7 shows three different reconstruction results for a separation distance of $d_{\mathrm{sep}} = 0.5\,\mathrm{mm}$ and cluster sizes of $d_{\mathrm{spix}} \in \{0.02,\ 0.32,\ 3.20\}$ mm. As can be seen, for the two smaller cluster sizes, which do not exceed the defect size of $d_{\mathrm{defect}} = 2\,\mathrm{mm}$, the reconstructions are equally satisfactory. In contrast, for a cluster size of $d_{\mathrm{spix}} = 3.2\,\mathrm{mm}$ the reconstruction is only of poor quality.

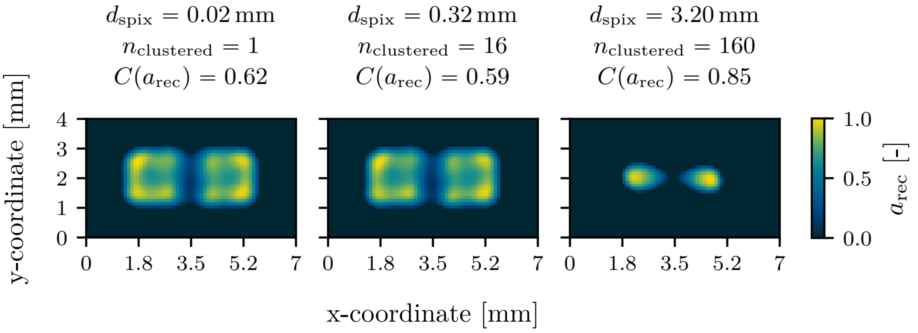

Figure 4.7: Reconstructed defect pairs for a separation distance of $d_{\mathrm{sep}} = 0.5\,\mathrm{mm}$ and cluster sizes of $d_{\mathrm{spix}} \in \{0.02,\ 0.32,\ 3.2\}$ mm. The three reconstructions each form a data point in Figure 4.6. While for the left two reconstructions with cluster sizes smaller than the defect size of $d_{\mathrm{defect}} = 2\,\mathrm{mm}$ the reconstruction quality is almost identical, the right reconstruction with a cluster size of $d_{\mathrm{spix}} = 3.2\,\mathrm{mm}$ shows a drastic decline in reconstruction quality.

4.3.3.2 Number of Projected Patterns

Another very valuable information to know upfront before performing any real-world experiments is the dependency of the achievable reconstruction quality on the amount of patterns projected (n_m). It can be expected that the reconstruction quality increases with the amount of performed measurements as any additional measurement adds some information about the internal structure of the OuT. However, this effect should taper off when n_m gets larger, as there is a physical upper limit to the reconstruction quality imposed by the joint effect of all experimental parameters considered. While photothermal SR is applied to overcome the limits set by the effects of thermal diffusion, the remaining parameters still more or less fully affect the achievable reconstruction quality. Therefore, for $n_m \to \infty$ the corresponding reconstruction $a_{\mathrm{rec}}^{\infty}$ should be optimal with respect to the other experimental parameters at play and accordingly, $C(a_{\mathrm{rec}}^{\infty})$ should reach a minimum. In order to explore this behavior, the three ROIs from Figure 4.5 have been reconstructed by projecting

$n_m \in \{2, 4, 6, 8, 10, 16, 20, 32, 40, 50, 80, 100\}$ patterns with a pixel size of $d_{\text{spix}} = 0.4\,\text{mm}$. The illumination parameters are summarized in Table 4.6. In total, projecting pixelated illumination patterns with 12 different number of measurements over the three ROI and subsequent SR reconstruction leads to 36 data points. For finding the optimal regularization parameters for each data point, 25 000 SR reconstruction problems (cf. Equation (2.78)) at a rate of ≈ 8 - 30 seconds per inversion on modern high-performance hardware have been performed, resulting in the graph shown in Figure 4.8.

Table 4.6: Illumination parameters used for studying the influence of the number of different measurements performed (n_m) on the reconstruction quality of photothermal SR reconstruction with pixel pattern illumination.

	Parameter	**Value**
Illumination Parameters	fill grade	$\beta = 0.5$
	number of measurements	$n_m \in \{2, 4, 6, 8, 10, 16, 20, 32, 40, 50, 80, 100\}$
	separation distance	$d_{\text{sep}} \in \{0.2, 0.5, 1.5\}\,\text{mm}$
	cluster size	$n_{\text{clustered}} = 20$
	pixel size	$d_{\text{spix}} = 0.4\,\text{mm}$

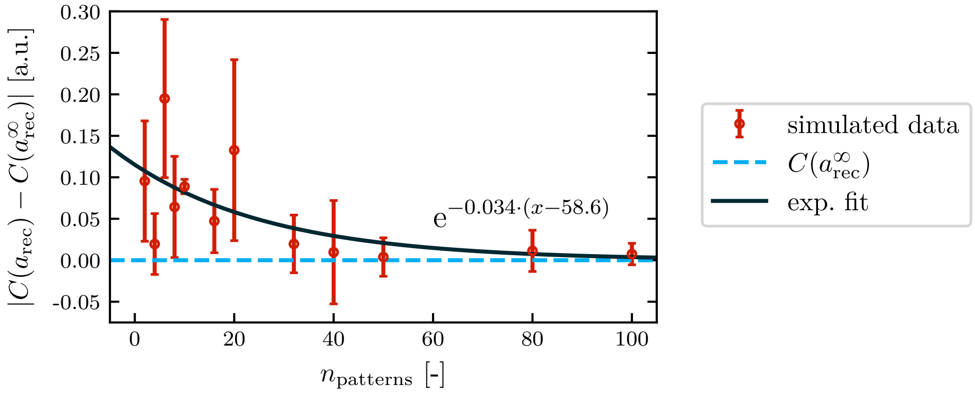

Figure 4.8: Study results on the dependence of the number of measurements performed on the reconstruction quality as measured by the quality metric $C(a_{\text{rec}})$ proposed in Equation (4.28) for three different defect separation distances. It can be observed that the reconstruction quality is exponentially approaching a limit $C(a_{\text{rec}}^{\infty})$ when $n_m \to \infty$. Each data point shows the mean and $\pm 1\sigma$ standard deviation for the reconstruction of all investigated separation distances combined. A similar plot has already been published in [A1].

In Figure 4.8 it can be observed that the data seems to follow the predicted progression, namely it seems to converge to a maximal reconstruction quality $C(a_{\text{rec}}^{\infty})$ in an exponential fashion. To further illustrate this behavior, the data is fitted with the following general exponential decay function:

$$C\left(a_{\text{rec}}^{n_{\text{patterns}}}\right) = A \cdot \exp\big(-\alpha \cdot (m - b)\big) + C\left(a_{\text{rec}}^{\infty}\right) \ , \tag{4.31}$$

where A, α, b, $C\left(a_{\text{rec}}^{\infty}\right) \in \mathbb{R}$. While for each individual data point the achievable reconstruction quality shows a large variation (large standard deviation), the standard deviation of the data points globally decreases with larger n_m, showcasing the effect of additionally added information on the ambiguity of the best reconstruction result. To better illustrate the exponential behavior of reconstruction quality, the data can be plotted in a semi-log graph as shown in Figure 4.9. As in log-space exponential functions describe straight lines, it can be visually verified that the data points approximate a line with negative slope and the deviation from this behavior is uncorrelated. As can be seen, this is fulfilled for the presented data.

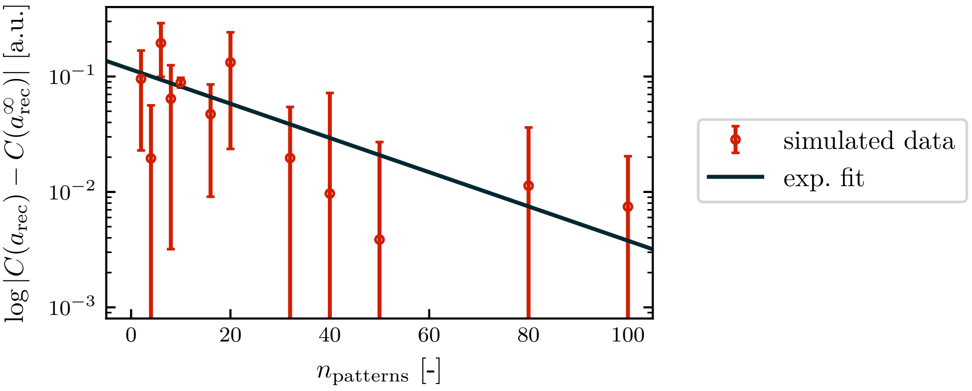

Figure 4.9: Data points as shown in Figure 4.8 plotted with logarithmic y-scale. As the reconstruction quality is approximately exponentially converging to a maximum reconstruction quality limit, the used comparison metric should decrease linearly in a semi-log scale, which can be observed for the presented data. A similar plot has already been published in [A1].

As the study shown in Figure 4.8 is only able to generate a relative comparison between the data points, the overall achievable reconstruction quality over the number of measurements $C\left(a_{\text{rec}}^{n_{\text{patterns}}}\right)$ is of lesser interest than its overall progression when n_m gets larger. Thus, the relative progress in achieving the best reconstruction quality $C\left(a_{\text{rec}}^{\infty}\right)$ should be examined, which can be calculated as follows:

$$1 - \frac{C\left(a_{\text{rec}}^{n_{\text{patterns}}}\right)}{C\left(a_{\text{rec}}^{1}\right)} = 1 - \exp\big(-\alpha \cdot (n_{\text{patterns}} - 1)\big) \ , \qquad \text{for } n_{\text{patterns}} \geqslant 1 \ . \tag{4.32}$$

For the presented data, a best fit coefficient of $\alpha = 0.034$ has been determined. This means that, according to Equation (4.32), after $n_m = 50$ measurements performed, the maximal reconstruction quality is already reached by 81%. Further increasing n_m only leads to a diminishing return, making $n_m = 50$ a well-rounded starting value for any experimental measurement according to the findings of this study.

The effect of this diminishing return at higher number of measurements can be further emphasized by looking at actual reconstructions for a separation distance of $d_{\text{sep}} = 0.5\,\text{mm}$ at three different $n_m \in \{2, 50, 100\}$, as presented in Figure 4.10. While for a very low number of measurements of $n_m = 2$ the reconstruction is still lacking, as can be seen in the first image on the left, for an increase from $n_m = 50$ (middle image) to $n_m = 100$ (right image) hardly any improvement is made.

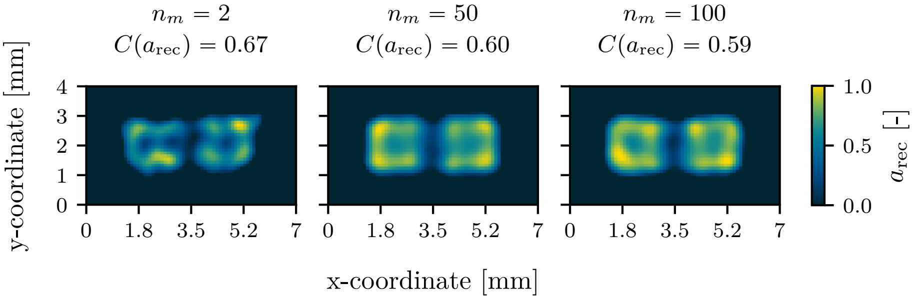

Figure 4.10: Reconstructed defect pairs for an investigated separation distance of $d_{\text{sep}} = 0.5\,\text{mm}$ and different number of simulated measurements of $n_m \in \{2, 50, 100\}$. The three reconstructions each form part of a data point in Figure 4.8. It can be observed that while a small number of measurements still leads to a perfectible reconstruction, after reaching a certain threshold (here ≈ 50), no significant improvement is made.

An experimental validation of the exponential convergence of the reconstruction quality can be found in Section 5.3.3 (cf. Figure 5.14).

5. Experimental Validation and Results

Within the following chapter, the previously proposed experimental approaches for achieving an SR reconstruction of internal defects are experimentally validated on a purpose-made OuT in conjunction with the proposed dedicated inversion techniques for the resulting photothermal SR reconstruction problem.

5.1 Object Under Test

For the validation of the proposed extension of the photothermal SR reconstruction technique to achieve true two-dimensional SR for arbitrary ROIs, a dedicated OuT has been designed and manufactured. The OuT resembles a $L = 4.5\,\mathrm{mm}$ thick plate made from 316L stainless steel. It has been additively manufactured layer-wise by means of laser powder bed fusion (PBF-LB) in a 2.5D process, which allows incorporating arbitrarily shaped internal defect structures. Each defect is introduced by locally not fusing the applied metal powder layer, which ultimately yields closed-off internal defects filled with the non-fused powdered base material. Due to different effective thermal conductivity (and slightly different effective density) of the bulk material and the powder, each defect also poses an effusivity contrast detectable by TT. A wireframe view of the OuT with visible internal defects is shown in Figure 5.1.

In order to be able to quantify the added benefit of the method, the OuT has been designed to incorporate several different pairs of identical cubical defects at different separation distances. This allows not only to quantify the reconstruction of the shape of individual defects, but also to visualize the improvement of detecting closely spaced defects as separate (cf. Figure 3.2). Furthermore, all defect pairs are available for testing at different orientations, allowing to additionally assess the SR-capabilities for directions that are not coinciding with the pixel grid of detector inside the IR-camera. A listing of all important dimensions and properties of the OuT can be found in Table 5.1.

Within the many different defect patterns contained in the OuT, two different ROIs have been utilized to be investigated within this thesis. The size and location of the two ROIs is shown in Figure 5.2.

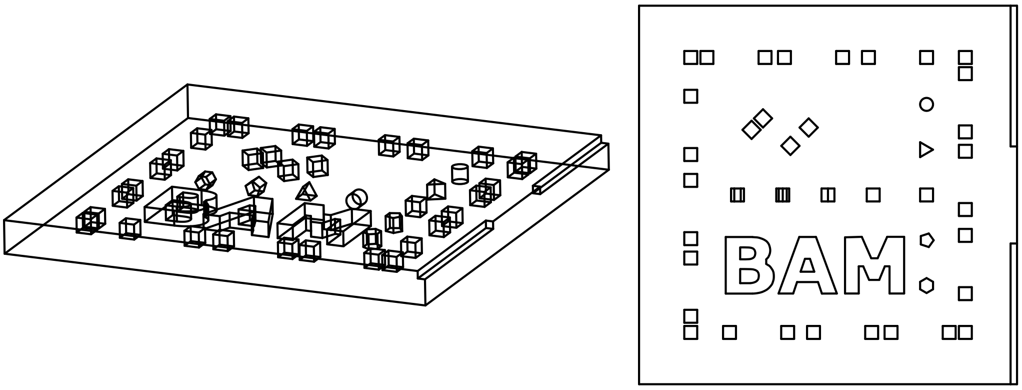

Figure 5.1: OuT specifically designed for the experimental validation of two-dimensional photothermal SR reconstruction. It has been additively manufactured (PBF-LB) from 316L stainless steel and measures 58.5 mm × 58.5 mm × 4.5 mm. It features several internal defects (regions of non-fused powder) at various separation distances. An overview over the important parameters can be found in Table 5.1.

Table 5.1: Properties of the OuT designed for the experimental validation of two-dimensional photothermal SR reconstruction.

Category	**Parameter**	**Value**	**Ref.**
OuT	material	316L stainless steel	
	side length	$d_{\mathrm{OuT}} = 58.5\,\mathrm{mm} \times 58.5\,\mathrm{mm}$	
	thickness	$L = 4.5\,\mathrm{mm}$	
	thermal diffusivity (calc.)	$\alpha = 3.76\,\mathrm{mm}^2/\mathrm{s}$	
	thermal conductivity	$k = 15\,\mathrm{W}/(\mathrm{m\,K})$	[83]
	density	$\rho = 7950\,\mathrm{kg}/\mathrm{m}^3$	[83]
	specific heat capacity	$c_p = 502\,\mathrm{J}/(\mathrm{kg\,K})$	[84]
Defects	shape	$d_{\mathrm{defect}} = 2\,\mathrm{mm} \times 2\,\mathrm{mm}$	
	depth below surface	$L_{\mathrm{defect}} = 0.5\,\mathrm{mm}$	
	separation distance	$d_{\mathrm{sep}} \in \{0.5,\ 1,\ 2,\ 4\}\,\mathrm{mm}$	
	contrast	$\zeta \approx 0.494$	Fig. 5.12

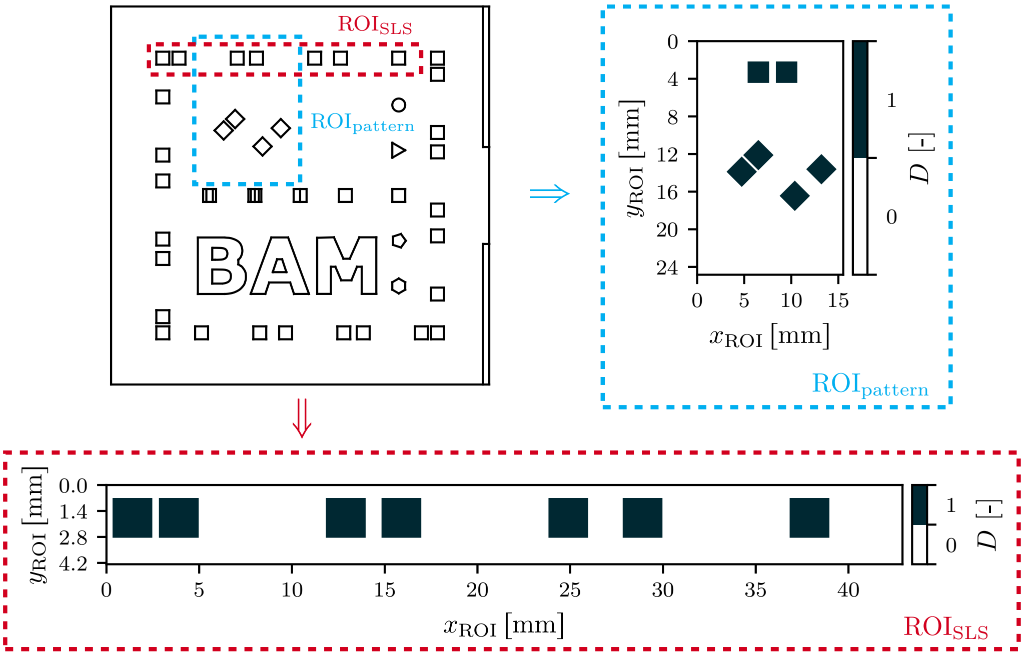

Figure 5.2: ROIs used for the experimental validation of the proposed two-dimensional photothermal SR reconstruction methodology. For the validation of the sequential laser scanning approach an ROI (ROI$_{\text{SLS}}$; red dashed area) containing three defect pairs and a single defect is used. The pattern projection approach is validated using an ROI (ROI$_{\text{pattern}}$; blue dashed area) containing three defect pairs oriented at different angles.

For validating the sequential laser scanning experimental approach, a horizontally drawn-out ROI near the top of the OuT has been investigated. It features three different defect pairs with different separation distances leading to $\gamma_{\text{sep}} \in \{1, 0.5, 0.25\}$ and a single defect with $\gamma_{\text{defect}} = 0.25$. As this ROI can be considered the two-dimensional variant of the prototypical one-dimensional ROI with internal defects investigated in the available literature on one-dimensional photothermal SR reconstruction, it enables (direct) comparison [54, A4, A5].

The two-dimensional pixel pattern projection approach on the other hand is examined on a different ROI more suitable to the aspect ratio of the utilized projector (cf. Section 5.3.1). Similarly, it features three different defect pairs with different separation distances leading to $\gamma_{\text{sep}} \in \{1, 0.5, 0.25\}$, of which two are oriented at a 45° angle towards the outer dimensions of the OuT. This allows also showcasing the performance for achieving SR along directions that do not by chance coincide with the pixel grid of the IR-camera utilized.

As the OuT has been purpose-made to specification for the work culminating in this thesis, the exact defect map D for both ROIs is known as a prior (deviations from the manufacturing tolerances are insignificant). This enables the application of the automated inversion method proposed in Section 4.3.2 to find the (optimal) regularization parameters for solving each individual photothermal SR reconstruction problem per ROI.

5.2 Sequential Laser Scanning

As the sequential laser scanning experimental approach to two-dimensional photothermal SR reconstruction can be implemented using common laboratory equipment also used for other laser-based TT, validation measurements as a proof-of-concept study have been conducted first using this approach. Additionally, its experimental implementation overlaps strongly with the already well-examined one-dimensional SR reconstruction variant to a certain extent, thus, previously gained experience could be transferred to the problem. However, the main focus was not yet directed towards optimal reconstruction quality and minimized efforts, which has been tackled afterwards by introducing two-dimensional pattern projection to the method.

5.2.1 Laser Scanning Setup

For examining the chosen ROI (cf. Figure 5.2) of the sequential laser scanning experimental approach the setup shown in Figure 5.3 has been utilized. Within this setup, the ROI has been illuminated point-wise with a laser spot with a diameter of $d_{\text{spot}} = 0.6\,\text{mm}$ with $\hat{Q} = 15\,\text{W}$ and $t_{\text{pulse}} = 0.5\,\text{s}$. The resulting temperature increase has been recorded with a spatial resolution

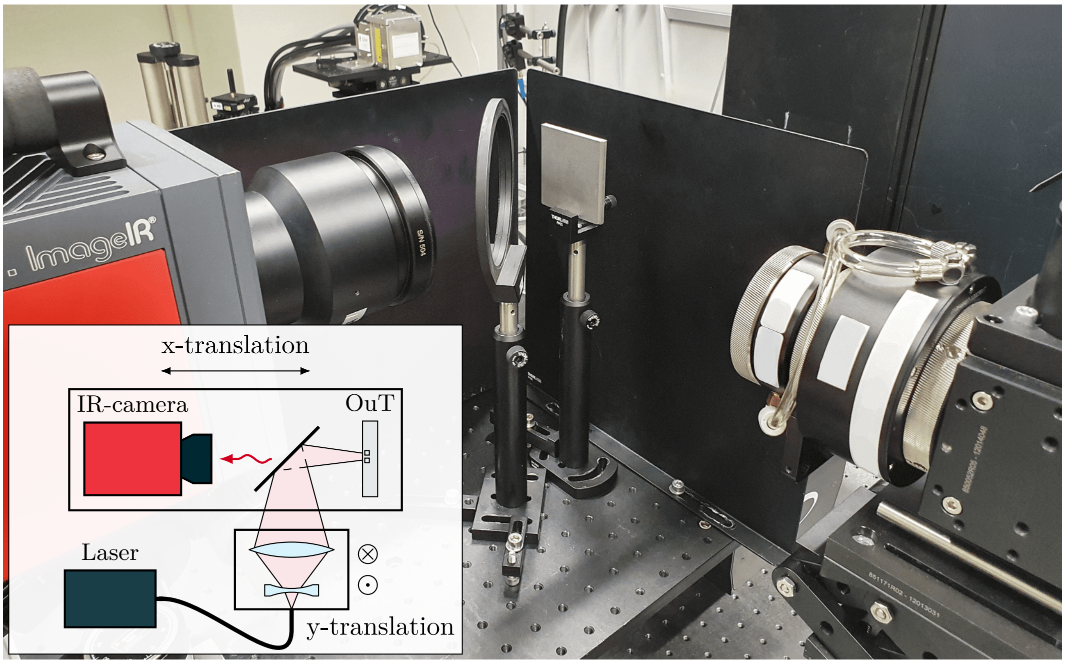

Figure 5.3: Laboratory setup for validating the sequential laser scanning experimental approach. The OuT is heated at every measurement grid position with a laser spot and the resulting change in temperature is recorded using an MWIR IR-camera. A dichroic mirror is used to align IR-camera and laser coaxially. While the OuT stays fixed with respect to the IR-camera, the laser is moved laterally and vertically to be able to point-wise scan the whole ROI.

of Δx, $\Delta y = 52\,\mu\text{m}$ at $f_{\text{cam}} = 100\,\text{Hz}$ using an ImageIR 9300 cooled MWIR IR-camera made by the company Infratec. In order to align the laser illumination and the IR-camera coaxially, a dichroic mirror has been utilized. This mirror is highly reflective for the laser wavelength of $\lambda = 940\,\text{nm}$, but transparent in the MWIR frequency band. The ROI has been heated for a total of $n_m = 403$ measurements spaced at a grid spacing of $r_d = 0.743\,\text{mm}$. To move the laser spot to the next measurement position, two motorized linear stages have been employed that either move the laser up and down (y-direction), or move the camera, OuT and dichroic mirror assembly as a unit in lateral direction (x-direction). This way, the ROI stays fixed within the field of view of the IR-camera, reducing the necessary post-processing efforts. A summary over all important measurement parameters is given in Table 5.2.

Table 5.2: Experimental parameters for validating the sequential laser scanning approach. The corresponding measurement setup is shown in Figure 5.3.

Category	**Parameter**	**Value**
Measurement grid	ROI size	$43\,\text{mm} \times 4.3\,\text{mm}$
	number of measurements	$n_m = 403$
	grid spacing	$r_d = 0.743\,\text{mm}$
Illumination	laser output power	$\hat{Q} = 15\,\text{W}$
	spot size	$d_{\text{spot}} = 0.6\,\text{mm}$
	pulse duration	$t_{\text{pulse}} = 500\,\text{ms}$
Temperature measurement	spatial resolution	Δx, $\Delta y = 52\,\mu\text{m}$
	sampling frequency	$f_{\text{cam}} = 100\,\text{Hz}$
	frequency band	MWIR

In order to guarantee the independence of each of the measurements and to not build up any thermal history within the OuT, between each of the $n_m = 403$ measurements the OuT has been given 20 s to cool back down to T_0. Overall, this leads to a total measurement duration of $\approx 150\,\text{min}$. While there is also the possibility to decrease the waiting time by compensating the data for the then occurring temperature build-up, ultimately, this has not been considered within this work as the focus was directed towards the potential improvements in measurement time introduced by the two-dimensional pattern projection (cf. Section 5.3.1).

5.2.2 Reconstruction Results

The obtained reconstructions of the ROI can be found in Figure 5.4. Here, in order to validate both of the proposed inversion techniques for the photothermal SR reconstruction inverse problem (sparse matrix stacking and inversion in frequency domain; cf. Section 4.1), the results of both methods are shown next to each other. Both methods are able to detect all the defects at reasonable quality. However, the reconstruction of the shape of each defect is still lacking. The reconstruction result obtained by inversion within the frequency domain also features some artifacts close to both ends of the ROI.

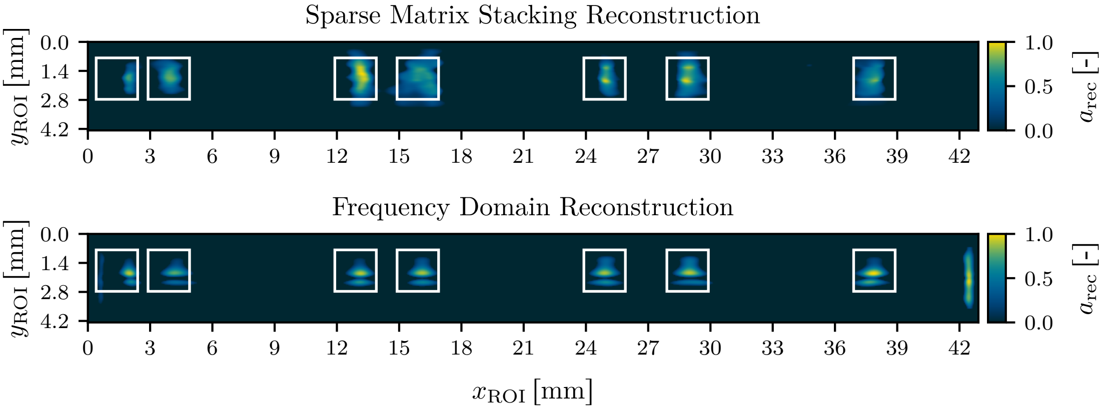

Figure 5.4: Reconstruction results obtained from the sequential laser scanning measurement approach: the reconstruction result generated by the sparse matrix stacking inversion technique is shown on the top, while the results obtained after inversion in the frequency domain is shown on the bottom. The true defect positions are indicated by white boxes. All specific parameters applied for each reconstruction can be found in Table 5.3.

The relative poorness of the reconstruction of the defect shapes can be mostly explained by the rather sparse measurement grid ($n_m = 403$ distributed over $43\,\mathrm{mm} \times 4.3\,\mathrm{mm}$ yields a measurement density of $\approx 2.18\,1/\mathrm{mm}^2$). For the one-dimensional pre-cursor of this work, typical measurement densities of $\approx 5.9\,1/\mathrm{mm}$ were utilized in order to achieve proper shape reconstruction [A4], which would translate to an infeasible $n_m \approx 6400$ for the two-dimensional case for the ROI at hand. Furthermore, the analytical investigations conducted in Section 4.3.3.2 also hint at the exponential penalty in shape reconstruction quality taken for conducting too few measurements. Even though this analytical study has been conducted for the compressed sensing (CS)-based pattern projection experimental approach (compared to the full matrix capture (FMC)-based sequential laser scanning approach), the overall tendency showcased by the study should remain valid. A mismatch in reconstructed shape is also an intractable challenge of regularized defect reconstruction as thoroughly investigated by Alazne Castelo Varela in her doctoral thesis [85].

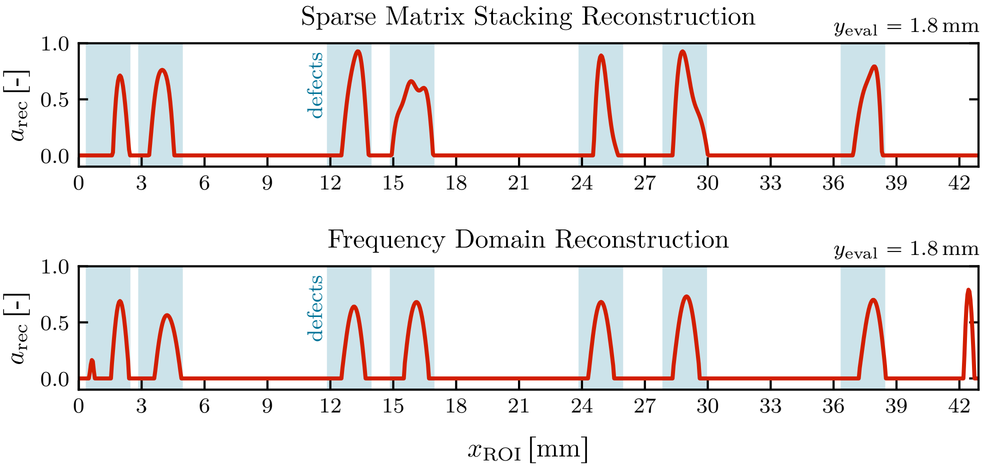

Figure 5.5: Sectional view of the reconstructions presented in Figure 5.4. The true defect positions are highlighted in blue color.

In this context the appearance of false positive signals within the reconstruction obtained by inversion in frequency space is not surprising, as near the edges of the ROI the information gained is reduced as the required homogeneity constraint for SR reconstruction (cf. Equation (2.74)) is more and more violated. However, the fact that the sparse matrix stacking approach does not show such artifacts indicates that the method is performing better at suppressing false positive signals.

The regularization parameters applied to each method leading to the reconstructions as presented in Figure 5.4 are stated in Table 5.3.

Table 5.3: Regularization parameters utilized to obtain the reconstruction results as presented in Figure 5.4.

Inversion Method	**Parameter**	**Value**
Sparse Matrix Stacking	penalty parameter	$\rho_{\mathrm{ADMM}} = 16$
	$\ell_{2,1}$-regularization	$\lambda_{2,1} = 1570$
	ℓ_2-regularization	$\lambda_2 = 100$
	iterations	$n_{\mathrm{iter}} = 400$
Frequency Domain Inversion	penalty parameter	$\rho_{\mathrm{ADMM}} = 16$
	$\ell_{2,1}$-regularization	$\lambda_{2,1} = 27$
	ℓ_2-regularization	$\lambda_2 = 500$
	iterations	$n_{\mathrm{iter}} = 400$

A quantitative comparison of the achieved reconstruction result with well-established TT methods can be found in Section 6.2.

5.3 Two-dimensional Pattern Projection

After the initial proof-of-concept experimental validation of two-dimensional photothermal SR reconstruction in its proposed form, more emphasis was laid onto making the experimental implementation of the method more viable for potential industrial application. As sequential laser scanning does not scale well to larger ROIs, and the shortcomings encountered are mostly based on the lack of sufficient measurements performed, the experimental approach has been fundamentally revised to make use of the projection of binary pixel patterns for the photothermal heating. Switching from an FMC to a CS based experimental approach also tackles the problem of lacking the necessary measurement densities to achieve optimal shape reconstruction.

5.3.1 Projection of Illumination Patterns

While illuminating an ROI with a round laser spot photothermally heating the OuT for performing TT is already a well-known concept within the field and can be performed using well available equipment, projecting pixelated patterns requires the use of a suitable projector. Even though there is already precedence to the use of digital micromirror device (DMD)-based digital light processing (DLP)-projectors for TT, their application so far has been mostly limited to theorizing their applicability and proof-of-concept studies [86–89], or use-cases within microscopic material characterization [90]. This can be mostly attributed to them only achieving rather small optical output power due to technological limits. At the heart of most DLP-projectors lies a DMD that is used to toggle individual pixels on and off in the output image and therefore controlling the resulting brightness of the individual pixel. Every pixel on a DMD consists of a microscopic MEMS-based flip-mirror that can be electrically toggled to flip into distinct orientations. A schematic view of the basic components of a DMD-based DLP-projector can be found in Figure 5.6.

However, thanks to steady technological advancement of the DLP technology mostly driven by the film/consumer electronics industry and more recently the additive manufacturing (AM) industry, the permissible optical power irradiating onto the DMD has increased dramatically and therefore also their achievable irradiance for the use-case of photothermal heating. An overview of the achievable irradiance with different DLP-projector technologies can be found in Appendix A4.

Within the work presented in this thesis, a top-of-the-line industrial laser-coupled DLP-projector based on the DLP650LNIR DMD chip manufactured by Texas Instruments has been procured (cf. Figure 5.7) [91]. This chip is rated for up to 160 W of incident optical power on the DMD in the near infrared (NIR) region. It features a total of 1280 × 800 individually addressable pixels and is able to project arbitrary binary patterns with an optical output power of up to $\hat{Q} = 86\,\mathrm{W}$ at $\beta = 1$ when coupled with a sufficiently powerful laser. In this case, the same NIR-laser operating at a wavelength of 940 nm as used for the sequential laser scanning setup is coupled to the projector set to a maximum output power of 270 W. This discrepancy in the ratio of input to output power directly indicates the heavy cooling necessary to operate the projector. In order to reach the output power as specified, the DMD-chip needs to be simultaneously water-cooled (from the back) and air-cooled (from the front) with a stream of compressed air.

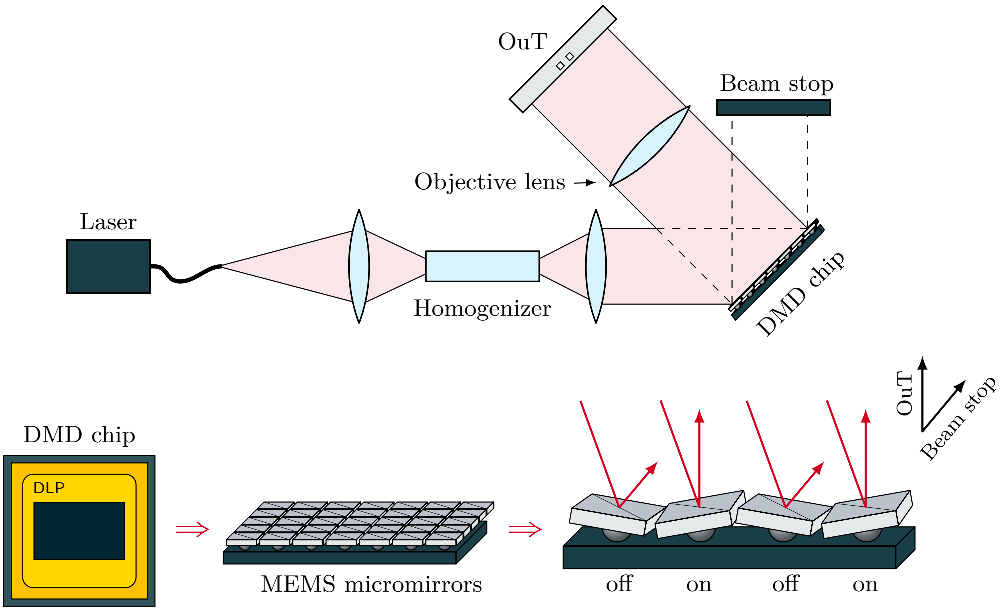

Figure 5.6: Schematic of a DMD-based DLP-projector: the heart of many modern DLP-projectors forms a DMD, consisting of a MEMS-device containing an array of small flip-mirrors. Depending on whether they are activated, the incoming laser beam is either directed toward the OuT or a beam stop on a per-pixel basis. Before hitting the DMD chip, the laser beam is spatially homogenized in intensity, typically by a light pipe, guaranteeing an even intensity distribution over all the pixels.

As the procured projector has been designed for the direct integration into AM machines, a mechanical mounting structure and an electrical input/output (I/O)-interface has been engineered as part of this thesis. An overview of the available interfaces of the projector for I/O, power and cooling can be found in Figure 5.8.

For projecting pixel-patterns onto an OuT, the projector has been integrated into the experimental setup as shown in Figure 5.9. Here, the projector is coupled to the same 940 nm NIR-laser as used for the sequential laser scanning setup. With the help of a 1.85× magnification objective, a pixel size on the ROI of $d_{\mathrm{pix}} = 20\,\mu\mathrm{m}$ has been achieved leading to a maximum irradiance of $\approx 21\,\mathrm{W/cm^2}$. Due to the rather small working distance of the utilized

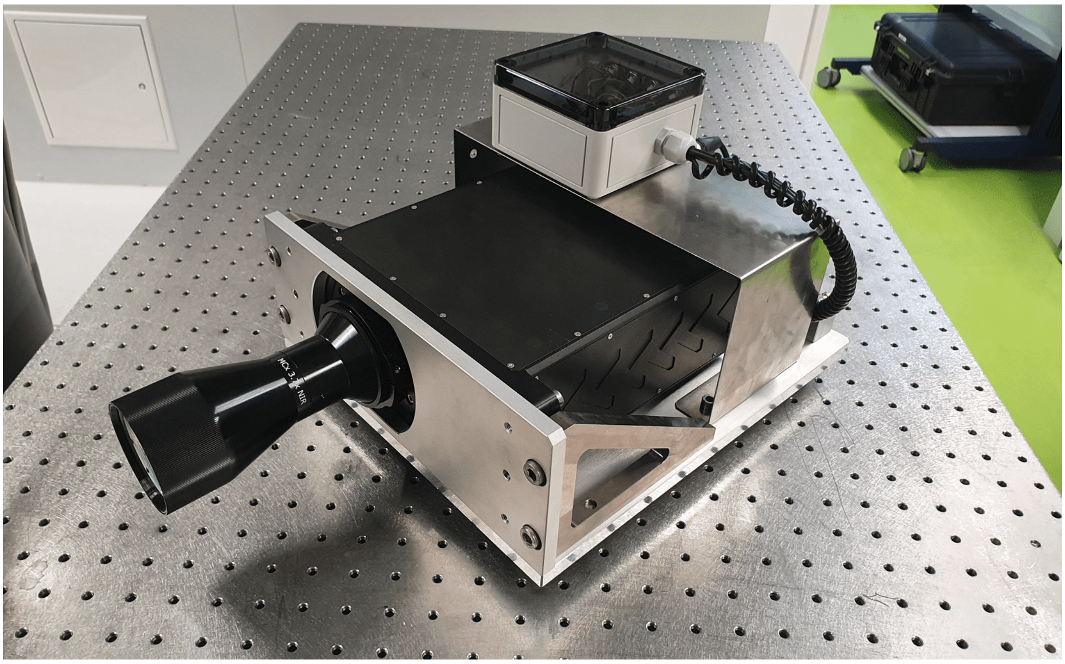

Figure 5.7: DLP-projector used within this thesis. This projector is based on a DLP650LNIR DMD chip, features 1280 × 800 individually addressable pixels and is able to project arbitrary binary patterns with an optical output power of up to $\hat{Q} = 86\,\mathrm{W}$ ($\beta = 1$). The output objective is exchangeable, allowing to adjust the size of the projection.

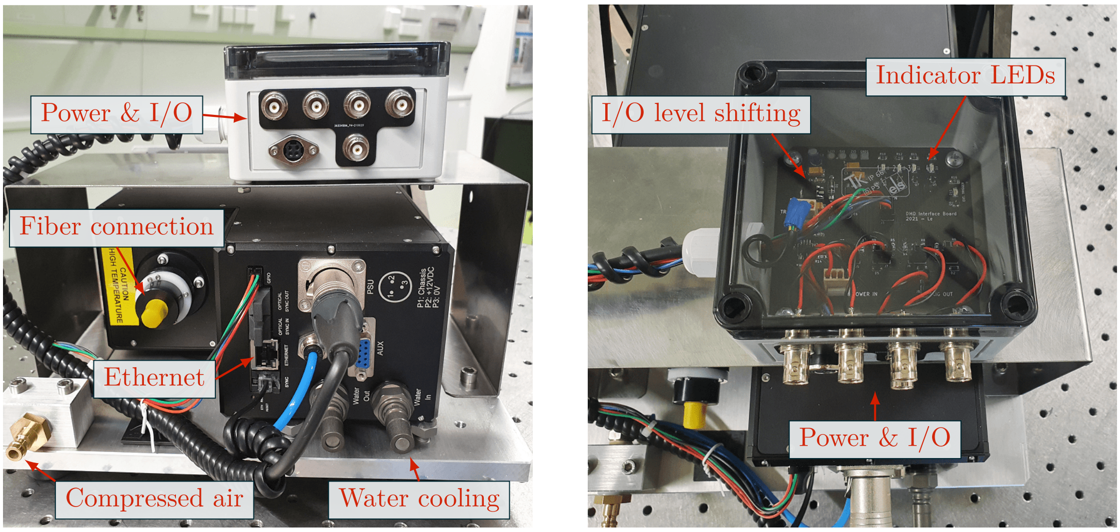

(a) Cooling (water and compressed air), laser and electrical interfaces necessary for operating the DLP-projector.

(b) Electrical interface box containing several I/O-level shifter, power filtering and indicator LEDs.

Figure 5.8: I/O-capabilities of the DLP-projector in use: the projector requires continuous cooling (compressed air & water) of its DMD chip, as well as an Ethernet and power connection (left). Its operation is synchronized by I/O-ports, which are made accessible by an electrical interface circuit developed as part of this thesis (right).

objective, a dichroic mirror has been used to fold the beam path, such that the resulting change in temperature due to the photothermal heating by the pixel patterns could be recorded coaxially using the same MWIR IR-camera as has already been utilized for the sequential laser scanning setup.

For the validation of the pattern projection approach, a projection of $n_m = 20$ different pixel patterns with a fill factor of $\beta = 0.5$ has been chosen as a representative parameter set for showcasing the capabilities of this specific experimental approach based on the observations made by analytical simulation of the expected performance (cf. Section 4.3.3). A detailed overview of the realized experimental parameters can be found in Table 5.4.

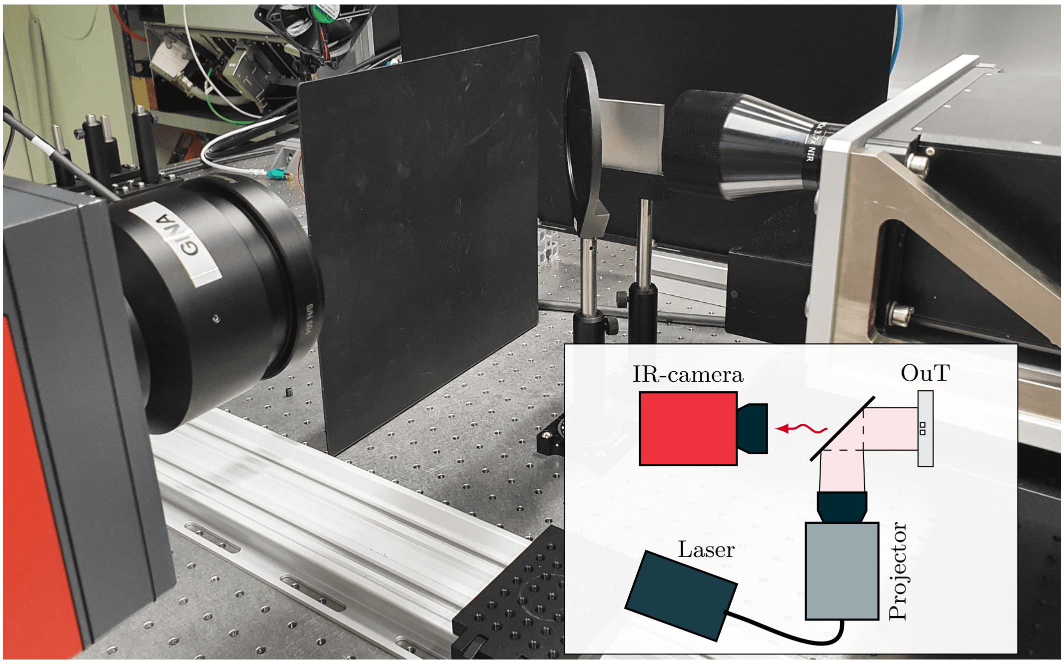

Figure 5.9: Laboratory setup for validating the two-dimensional pattern projection experimental approach. The OuT is heated using a DLP-projector, which projects two-dimensionally structured pixel patterns onto the ROI. The resulting temperature change is recorded with an MWIR IR-camera, which is coaxially aligned with the optical path via a dichroic mirror.

Between projecting each pattern, the OuT has been given 20 s to cool down back to T_0. For $n_m = 20$ projected patterns, this leads to a total measurement time of ≈ 8 min, which is 20× faster for a $\approx 2.2\times$ larger ROI than the measurement conducted with the sequential laser scanning approach.

While for the sequential laser scanning experimental approach all employed devices (laser, camera, linear stages) can be easily synchronized using a control computer, the pattern projection approach using the presented industrial grade DLP-projector is slightly more complex. In order to operate the projector, it is necessary to precompute all patterns used

Table 5.4: Experimental parameters for validating the two-dimensional pattern projection approach. The corresponding measurement setup is shown in Figure 5.9.

Category	Parameter	Value
DLP-projector	pixel size on ROI	$d_{\text{pix}} = 20\,\mu\text{m}$
	total pixels (x-direction)	$n_{\text{pix,x}} = 800$
	(y-direction)	$n_{\text{pix,y}} = 1280$
	laser output power (at $\beta = 1$)	$\hat{Q} = 86\,\text{W}$
Illumination pattern	ROI size	$16\,\text{mm} \times 25.6\,\text{mm}$
	number of measurements	$n_m = 20$
	fill factor	$\beta = 0.5$
	pixel cluster size	$d_{\text{spix}} = 0.4\,\text{mm}$
	pixels clustered	$n_{\text{clustered}} = 20$
	pulse duration	$t_{\text{pulse}} = 500\,\text{ms}$
Temperature measurement	spatial resolution	$\Delta x, \Delta y = 100\,\mu\text{m}$
	sampling frequency	$f_{\text{cam}} = 160\,\text{Hz}$
	frequency band	MWIR

for the n_m measurements and upload them to the projector via the Ethernet connection. Furthermore, the projector features an internal FPGA-based sequencer that mediates the projector's operation. It has to be programmed for every measurement by uploading program code written in a proprietary Turing-complete imperative programming language via the Ethernet connection. This sequencer code allows, among other things, to send images to the DMD-chip, cycle through the measurements, toggle the projector's I/O-ports to trigger the laser and IR-camera and wait for predefined durations for the OuT to cool down to T_0 between the measurements. Therefore, the whole experiment can be controlled using just the DLP-projector providing that a suitable sequencer code is uploaded beforehand.

To facilitate the communication with the DLP-projector, an extensive interface library (6000 LOC) has been programmed from scratch as part of this thesis as there is no software supplied by the manufacturer due to the projector being designed to be integrated directly into industrial machinery. A schematic overview of the interoperation of the experimental hardware used for pattern projection based photothermal SR reconstruction can be found in Figure 5.10.

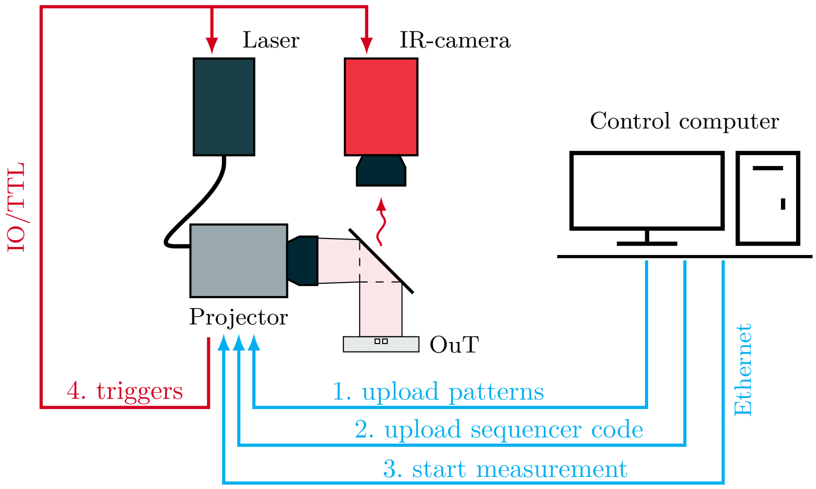

Figure 5.10: Interoperation diagram of the utilized hardware for pattern projection based photothermal SR reconstruction: a control computer uploads the set of n_m pixel patterns to the projector. Afterwards, the internal sequencer of the projector is programmed to project the patterns in sequence, trigger the camera and the laser via its I/O-ports and wait between the measurements for the OuT to cool down.

5.3.2 Reconstruction Results

Utilizing the previously described measurement setup and the experimental parameters described in Table 5.4, a reconstruction result as presented in Figure 5.11 has been obtained. The identified set of parameters applied for the inversion of the photothermal SR problem leading to this reconstruction can be found in Table 5.5. The regularization parameters have been determined automatically using the automatic regularization parameter determination method proposed in Section 4.3.2 without any further manual interference. As can be seen in Figure 5.11, all defects have been identified by the reconstruction without any false positive indication and their shape has been reconstructed with good accuracy. Only close to the edge of the ROI (especially visible for the rightmost defect), the reconstruction of the defect shapes is lacking, which can be explained by them already being to close to the edge of the ROI such that a degradation of reconstruction quality due to the local beginning violation of the homogeneity constraint for SR reconstruction (cf. Equation (2.74)) starts to occur. A sectional view of the reconstruction result at $y_{\text{eval}} = 2.8\,\text{mm}$ (uppermost defect pair) exemplarily shows that the defects can be undoubtedly separated with the gap separating both defects accurately reconstructed.

As the reconstruction has been obtained using only $n_m = 20$ measurements, the reconstruction result can be expected to still be improvable as there is still room to further increase the number of measurements for which an increase of reconstruction quality is predicted to occur (cf. Section 4.3.3.2). However, as one of the main goals of this work is to reduce the necessary

Table 5.5: Regularization parameters utilized to obtain the reconstruction results as presented in Figure 5.11.

Inversion Method	Parameter	Value
Frequency Domain Inversion	penalty parameter	$\rho_{\text{ADMM}} = 9900$
	$\ell_{2,1}$-regularization	$\lambda_{2,1} = 490$
	ℓ_2-regularization	$\lambda_2 = 34.4$
	iterations	$n_{\text{iter}} = 100$

time and effort to a minimum, the number of performed measurements has been deliberately chosen ambitiously low to showcase that $n_m = 20$ and the achieved result already pose a suitable compromise. Compared to the reconstruction results obtained using the sequential laser scanning experimental approach, the pattern projection experimental approach shows clearly superior reconstruction quality for a larger ROI at significantly reduced measurement efforts.

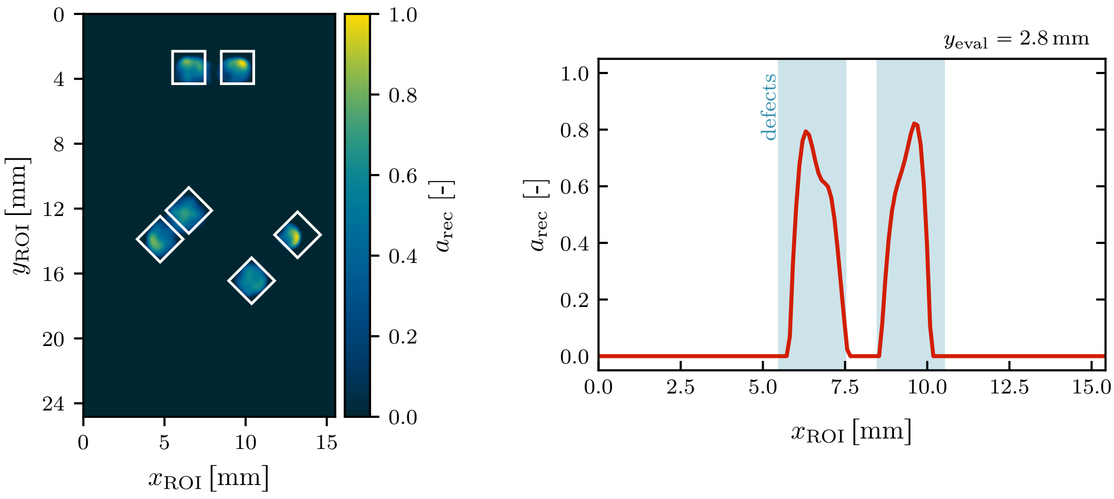

(a) Reconstruction result after pattern projection. The true defect positions are indicated as white boxes.

(b) Sectional view of the reconstruction result at $y_{\text{eval}} = 2.8$ mm. The true defect positions are highlighted with blue color.

Figure 5.11: Reconstruction results obtained from the pattern projection experimental approach: all specific parameters applied for each reconstruction can be found in Table 5.5. Similar figures have already been published in [A2].

A quantitative comparison of the achieved reconstruction result with well-established TT methods can be found in Section 6.3.

5.3.3 Validation of the Forward Solution

In order to also experimentally validate the forward solution to the photothermal SR reconstruction problem as proposed in Section 4.3.1, the previously described experimental setup for photothermal heating with pattern projection has also been utilized to generate measured temperature profiles for gauging them against synthetic data generated by the forward solution for identical parameters. This validation process aims to assess the accuracy of the forward solution by comparing the measured temperature profiles with the corresponding synthetic data, further confirming the observations made analytically on the influence of certain experimental parameters on the achievable reconstruction quality (cf. Section 5.3.3). In order to quantify the similarity of the synthetic data compared to the ground-truth measured data, the coefficient of determination $R^2 \in]-\infty, 1]$ between them is evaluated. R^2 is defined as follows:

$$R^2(T^m_{\text{meas,sim}}, T^m_{\text{meas}}) = 1 - \frac{\|T^m_{\text{meas}} - T^m_{\text{meas,sim}}\|_2^2}{\|T^m_{\text{meas}} - \overline{T^m_{\text{meas}}}\|_2^2} \,, \tag{5.1}$$

where a value of R^2 close to $R^2 \approx 1$ indicates a high agreement of the measured data and its synthetic approximation and $R^2 < 0$ indicates a poor concordance such that assuming a constant temperature value over the ROI would lead to better agreement than the simulation itself.

The temperature data for one representative measurement $T_{\text{diff,meas}}$ overlaid with the predicted temperature distribution $T_{\text{diff,sim}}$ by the forward solution for identical experimental parameters as given in Table 5.4 at $y_{\text{eval}} = 12.5\,\text{mm}$ is shown in Figure 5.12. At this offset in the ROI, one

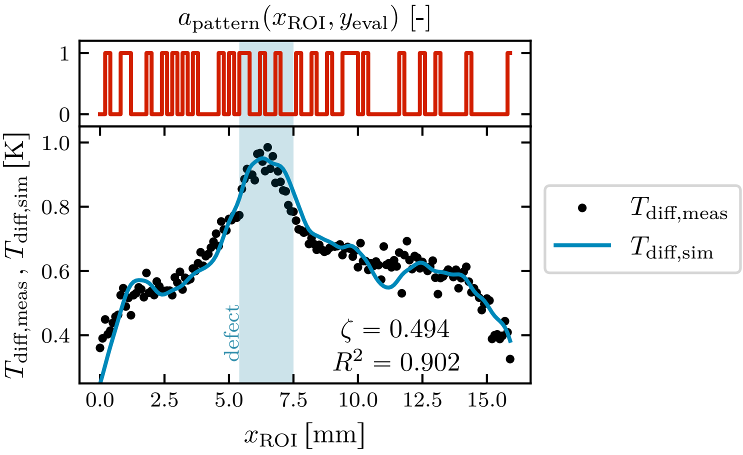

Figure 5.12: Quality of the forward solution and estimation of ζ. For the experimental parameters shown in Table 5.4, the quality of the forward solution is evaluated at $y_{\text{eval}} = 12.5\,\text{mm}$. For reference, on top the projected pattern a_{pattern} generating the temperature profile is shown. The defect contrast factor $\zeta = 0.494$ has been determined as best-fit. Measured and synthetic data lie in good agreement ($R^2 = 0.902$). A similar figure has already been published in [A2].

of the defects at a 45° angle is present. The defect contrast ζ necessary for the generation of the synthetic data (cf. Equation (4.25)) – previously unknown for the defects in this particular OuT – has been determined as the best fit value over all pixel coordinates and measurements, such that the coefficient of determination between the model and measured data is maximized. This way, a $\zeta = 0.494$ has been determined, leading to $R^2 = 0.902$ for the presented portion of the data, which indicates a reasonable performance of the forward solution in approximating measured data. As can be seen, the overall trend of the data is well captured by the synthetic data, equally near the defect present as well as near the edges of the ROI. For reference, the exact pattern leading to the temperature distribution at this location in the ROI shown in Figure 5.12 is displayed on the top.

Therefore, at least for the parameters utilized in this validation measurement, it can be argued that the forward solution proposed reasonably approximates measured data to a point that it can be confidently used for analytical investigations as performed in Section 4.3.3. In order to gain additional confidence, the two representative investigations on the achievable reconstruction quality (dependence on the pixel cluster size and number of measurements performed) already carried out, can be experimentally validated in a similar fashion.

Influence of the Pixel Cluster Size

In Section 4.3.3.1, the influence of the pixel cluster size d_{spix} has been explored by means of synthetic data generated by the proposed forward solution. To substantiate the validity of this study, the proposed forward solution has to also closely resemble measured data independent of the cluster size used for generating the illumination pattern. In order to evaluate this issue, multiple measurements with varying cluster size but otherwise identical experimental parameters as presented in Table 5.4 have been carried out. In total, patterns with cluster sizes of $d_{\mathrm{spix}} \in \{0.02, 0.1, 0.2, 0.4, 0.8\}$ mm corresponding to a clustering of $n_{\mathrm{clustered}} \in \{1, 5, 10, 20, 40\}$ and $n_m = 20$ each have been projected, and the resulting temperature distributions have been compared to the predicted temperature distributions by the forward solution by means of the coefficient of determination between them. The result of this procedure is shown in Figure 5.13.

In Figure 5.13 it can be observed that while the forward solution poses a suitable approximation for the measured data for small cluster sizes $d_{\mathrm{spix}} \leqslant 0.2\,\mathrm{mm}$, its validity drops off for larger values and also the variance in the quality of the agreement increases. This can be rooted in the decreasing dimensionality of the heat flow as d_{spix} increases. As the proposed forward solution is dependent on the PSF of the OuT, the PSF has to be valid for the investigated parameters as well. For larger d_{spix} this is not the case as the considered PSF within this thesis requires a three-dimensional heat flow, while for increasing d_{spix} the resulting heat flow converges to be one-dimensional. This phenomenon is also studied in literature [92, p. 69], where a rather conservative bound of $d_{\mathrm{spot}} \cong d_{\mathrm{spix}} > 20 \cdot L_{\mathrm{diff}}$ for d_{spix} is given at which

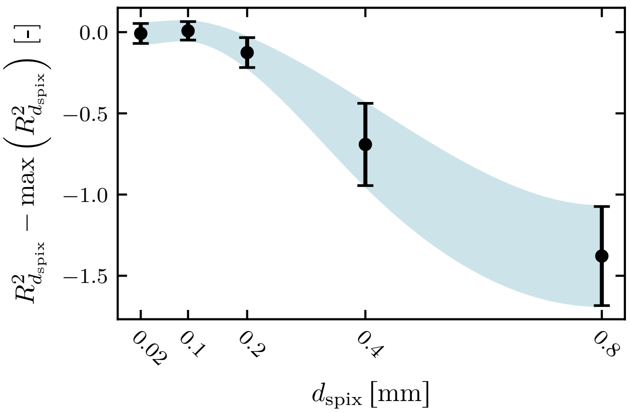

Figure 5.13: Influence of the pixel cluster size d_spix on the quality of the presented forward model measured by the determination coefficient. For each cluster size d_spix, $n_m = 20$ patterns have been projected, and the resulting temperature has been compared to the prediction of the forward model over all coordinates and all performed individual measurements. The presented data is normalized to the maximum achieved determination coefficient $\max\left(R^2\right) = 0.723$, which has been calculated over the full ROI including all edge effects and overlay errors for all measurements. The shown error bars indicate $\pm 1\sigma$ standard deviation. A similar figure has already been published in [A2].

the transition towards a fully one-dimensional heat flow is completed. Therefore, it can be concluded that when trying to correlate experimentally acquired data with synthetic data generated by the proposed forward solution, a cluster size of $d_\mathrm{spix} \approx 0.2\,\mathrm{mm}$ should not be exceeded for similar OuTs. As the derivation of the forward solution is tightly coupled to the underlying modelling approach of the photothermal SR reconstruction method itself, this threshold should be considered also for reconstructions on experimentally acquired data.

However, for the study presented in Section 4.3.3.1 where even larger cluster sizes up to $d_\mathrm{spix} = 3.2\,\mathrm{mm}$ have been investigated, this restriction does not invalidate the results obtained for those larger cluster sizes as both the data generation by means of the proposed forward solution and the reconstruction step have been performed with the same analytical PSF. Therefore, in this particular case, the PSF is always valid independent of the cluster size. This fact can be seen as an extrapolation of the expected behavior without considering the deterioration of the dimensionality of the resulting heat flow.

Reconstruction Quality vs. Number of Measurements

For the dependency of the achievable reconstruction quality on the number of performed measurements as investigated in Section 4.3.3.2, a similar validation measurement campaign can be conducted. Utilizing the experimental parameters as presented in Table 5.4 in order to generate reconstruction quality data points for $n_m \in \{2, 4, 6, 8, 10, 16, 20, 32, 40, 50, 80, 100\}$ for a cluster size of $d_{\text{spix}} \in \{0.4, 0.8\}$ mm each, the graph shown in Figure 5.14 has been obtained.

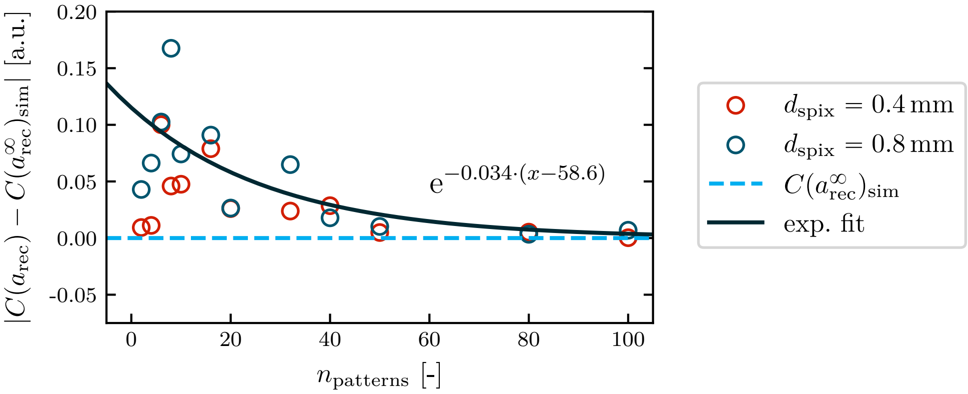

Figure 5.14: Experimental validation of the numerical study on the influence of the number of performed measurements on the reconstruction quality as presented in Figure 4.8. The achievable reconstruction quality has been quantified by means of the proposed quality metric for data points taken for $n_m \in \{2, 4, 6, 8, 10, 16, 20, 32, 40, 50, 80, 100\}$ at two different cluster sizes of $d_{\text{spix}} \in \{0.4, 0.8\}$ mm. For the data, the exponential trend line with parameters as obtained from the previously performed analytical study is shown. The experimentally obtained data closely resembles the same exponential convergence in reconstruction quality as predicted by the analytical study. A similar plot has already been published in [A1].

Here, the experimentally obtained reconstruction quality as quantified by the proposed quality metric (cf. Section 4.3.2) has been overlaid with the exponential trend line using the same parameters exactly as obtained from the previously performed analytical study. For better comparability, the experimental data has been linearly scaled to equal scale as the analytical results (same amplitude A as denoted in Equation (4.31)). It can be observed that the experimentally acquired data follows the previously determined exponential trend to the same extend as the analytically generated data. As has already been observed utilizing analytically generated data, increasing the number of performed measurements increases not only the achievable reconstruction quality but also decreases the observable scatter introduced by the reconstruction. Overall, this experimental validation measurement reinforces the observation made analytically, namely, that it is advisable to perform around at least $n_m = 50$ measurements for similar OuTs when a high fidelity in the reconstruction result is required.

6. Discussion of the Results

In order to benchmark the added benefit of the photothermal SR reconstruction results obtained in the previous chapter, the reconstruction results need to be put further in context with more well-established TT methods. As these methods commonly make use of homogeneous illumination of the ROI, reference measurements with homogeneous illumination have been conducted in the same setup as utilized to obtain the SR reconstructions. An exemplary thermogram obtained from such a homogeneous illumination measurement covering the whole OuT is shown in Figure 6.1 for reference.

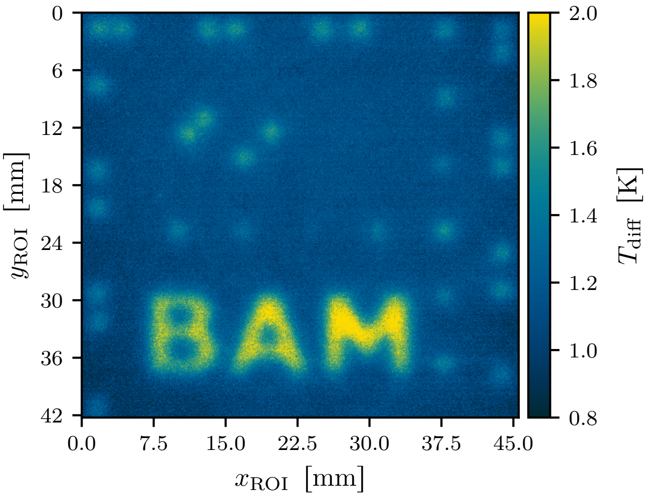

Figure 6.1: Maximum thermogram for a homogeneous illumination of the whole OuT as presented in Figure 5.1: for a $t_{\mathrm{pulse}} = 500\,\mathrm{ms}$ pulsed homogeneous laser illumination with $\hat{Q} = 456\,\mathrm{W}$ the shown thermogram at $t_{\mathrm{eval}} = 500\,\mathrm{ms}$ has been obtained. The visible hot spots indicate defective areas. Similar homogeneous illumination measurements will be used to benchmark the previously presented reconstruction results.

As reference methods, the acquired data from the homogeneous illumination measurements has been processed using the difference thermography method as well as PPT evaluation (cf. Section 2.1.4). Both methods have been selected as they are widely applied and well-studied. Furthermore, both methods require a representative and sound reference area, which is present in all the investigated ROIs. This allows both reference methods to be used under ideal conditions.

6.1 Comparison Metrics

Comparing inherently different thermographic data processing techniques is not a trivial task, as, by the nature of the underlying properties they make use of, they enhance the thermographic measurement result in different ways. Commonly in the field, different methods are compared by their improvement of the SNR or signal-to-background ratio (SBR), which are defined as follows [93]:

$$\mathrm{SNR} = 20 \cdot \log_{10}\left(\frac{A_{\mathrm{signal}}}{\sigma_{\mathrm{noise}}}\right)\,\mathrm{dB} \tag{6.1}$$

$$\mathrm{SBR} = 20 \cdot \log_{10}\left(\frac{\bar{A}_{\mathrm{signal}}}{\bar{A}_{\mathrm{background}}}\right)\,\mathrm{dB}\ , \tag{6.2}$$

where $\bar{A}_{\mathrm{signal}}$ and $\bar{A}_{\mathrm{background}}$ are the mean signal amplitude and the mean background signal amplitude, respectively. However, for the case of sparse defect reconstructions, as it is the case for the presented photothermal SR reconstruction results, these metrics can not be reasonably applied due to the lack of any background signal and the full suppression of measurement noise. Thus, in this case both metrics tend towards infinity (SNR, SBR $\to \infty$).

Therefore, other metrics are necessary for the quantitative comparison of the different data processing methods. One identified metric that can be utilized, is the NMSE (cf. Equation (4.27)) between the processed data and the true defect map D, which, in this special case, is well known for all investigated ROIs. The NMSE compares the processed data to the true defect map by essentially evaluating pixel-wise the ℓ_2 distance between both. As $D(x, y) \in [0, 1]$, for fair comparison, all data is scaled to the same interval first. This leads to the following metric having been evaluated for all results:

$$\mathrm{NMSE}_{\mathrm{eval}}(A_{\mathrm{signal}}, D) = \mathrm{NMSE}\left(\phi(|A_{\mathrm{signal}}|), D\right)\ , \tag{6.3}$$

where $\phi(\cdot)$ is the normalization function introduced in Equation (4.15).

Additionally, the coefficient of determination R^2 (cf. Equation (5.1)) has been identified as a well-suited metric for comparison of the results of different data processing methods. R^2, as a statistical measure quantifies, how much of the variance in the processed data can be attributed to the desired resemblance of the defect map D. Similarly to calculating the NMSE, the input data needs to be scaled first for a fair comparison as well:

$$R^2_{\mathrm{eval}}(A_{\mathrm{signal}}, D) = R^2\left(\phi(|A_{\mathrm{signal}}|), D\right)\ . \tag{6.4}$$

Lastly, Ahmadi [54] examined the use of the Wasserstein distance as a quality metric for evaluating the reconstruction quality of sparse SR reconstructions. It provides a measure of the cost it takes to transform one distribution into another (mean distance each element needs to be moved). Mathematically, the Wasserstein distance of the first moment between two one-dimensional distributions μ_x and ν_x is defined as follows:

$$\mathcal{W}_1(\mu_x, \nu_x) = \int_{\mathbb{R}} |\mathrm{CDF}_\mu^{-1}(x) - \mathrm{CDF}_\nu^{-1}(x)| \, \mathrm{d}x \ , \tag{6.5}$$

where CDF_μ and CDF_ν are the cumulative distribution functions of μ_x and ν_x respectively. In the presented TT context, μ_x and ν_x are considered to be continuous uniform distributions.

While the one-dimensional Wasserstein is sufficient for assessing one-dimensional thermographic problems as state-of-the-art for laser-based photothermal SR reconstruction prior to this work, for two-dimensional reconstructions it has to be expanded as well. Here, most commonly the sliced Wasserstein distance $\mathcal{W}_1^{sliced}(\mu_{x,y}, \nu_{x,y})$ can be applied, which is defined as the mean Wasserstein distance $\mathcal{W}_1(\mu_r, \nu_r)$ evaluated along all arbitrarily oriented one-dimensional slices $r_{x,y}$ through both two-dimensional distributions $\mu_{x,y}$ and $\nu_{x,y}$ [94]. This can be implemented by means of a Monte Carlo approach by sampling both distributions along randomly oriented slices $r_{x,y}$ and subsequently calculating the one-dimensional Wasserstein distance of each sample, which ultimately converges to $\mathcal{W}_1^{sliced}(\mu_{x,y}, \nu_{x,y})$ given sufficiently many samples. As every $\mathcal{W}_1(\mu_r, \nu_r)$ can be calculated very efficiently, $\mathcal{W}_1^{sliced}(\mu_{x,y}, \nu_{x,y})$ can be determined in this iterative process even up to high precision (guaranteed by a large amount of samples taken).

This leads to the following metric, by which all data processing methods have been evaluated by:

$$\mathcal{W}_{\mathrm{eval}}(A_{\mathrm{signal}}, D) = \mathcal{W}_1^{sliced}(\phi(|A_{\mathrm{signal}}|), D) \ . \tag{6.6}$$

An overview over all utilized metrics is given in Table 6.1.

Table 6.1: Overview over all applied metrics for quantitative comparison of different thermographic data processing methods with the achieved results by two-dimensional photothermal SR reconstruction.

	Metric	**Range**	
$\mathrm{NMSE}_{\mathrm{eval}}$	Normalized Mean Square Error	$[0, \infty[$	lower is better
R^2_{eval}	Coefficient of Determination	$]-\infty, 1]$	higher is better
$\mathcal{W}_{\mathrm{eval}}$	Wasserstein Distance	$[0, \infty[$	lower is better

Evaluating the quality of the processed data using the aforementioned metrics, however, is only accurately possible up to a certain threshold, as those metrics do not incorporate any knowledge about the nature of typical defects. This can be illustrated when evaluating a dataset where all values are set to zero. As defects are most often rare events, this trivial reconstruction approximates the true defect map already quite well. This effect is especially pronounced for the Wasserstein distance and NMSE metrics, while the R^2 metric is less affected due to its statistical nature. As a consequence, the results of both affected metrics have to be rated significantly above the score attributed to the all zeros dataset in order for any dataset to be considered reasonably portraying the true defect map. Those threshold values evaluated per investigated ROI can be found in Table 6.2.

Table 6.2: Proposed metrics evaluated for the trivial all zeros dataset for both investigated ROIs: for $\mathrm{NMSE}_{\mathrm{eval}}$ and $\mathcal{W}_{\mathrm{eval}}$ all results that are rated better than the indicated values for the trivial dataset do not unambiguously indicate a better resemblance of the true defect map D.

Metric	**All Zeros Dataset**	
	$\mathrm{ROI}_{\mathrm{SLS}}$	$\mathrm{ROI}_{\mathrm{pattern}}$
$\mathrm{NMSE}_{\mathrm{eval}}$	1.18	1.07
R^2_{eval}	-0.18	-0.07
$\mathcal{W}_{\mathrm{eval}}$	3.87	0.69

6.2 Sequential Laser Scanning

Evaluating the chosen reference methods (PPT and DT) on temperature data obtained by homogeneous illumination for the ROI utilized for the sequential laser scanning experimental approach, the datasets as shown in Figure 6.2 have been obtained.

Here, the added benefit of post-processing of thermographic measurement data is clearly showcased qualitatively by the very noticeable increase in the reconstruction quality of the underlying defect map. However, the shortcoming of classical thermographic data processing methods can also be observed, as all methods to their own extent feature a pronounced noise background that for more challenging OuTs/ROIs can make a proper defect reconstruction or even detection not viable. Furthermore, all defect signals are very circular in their shape, also showing clear evidence for the influence of the thermal diffusion process on the shape reconstruction (cf. Section 2.2.2). In contrast, both obtained photothermal SR reconstruction results as already introduced in Figure 5.4 are shown besides for reference. While those reconstructions are still lacking in form accuracy, the added benefit of the SR reconstruction can be clearly observed, as both reconstructions show no interfering noise background. The reconstruction obtained by the sparse matrix stacking reconstruction approach also already tends to correctly reconstruct the square shape of the defects. However, both reconstructions are far from perfect, which can be mainly attributed to the very coarse measurement grid (cf. analysis in Section 5.2.2) utilized, which was necessary to keep the experimental efforts manageable.

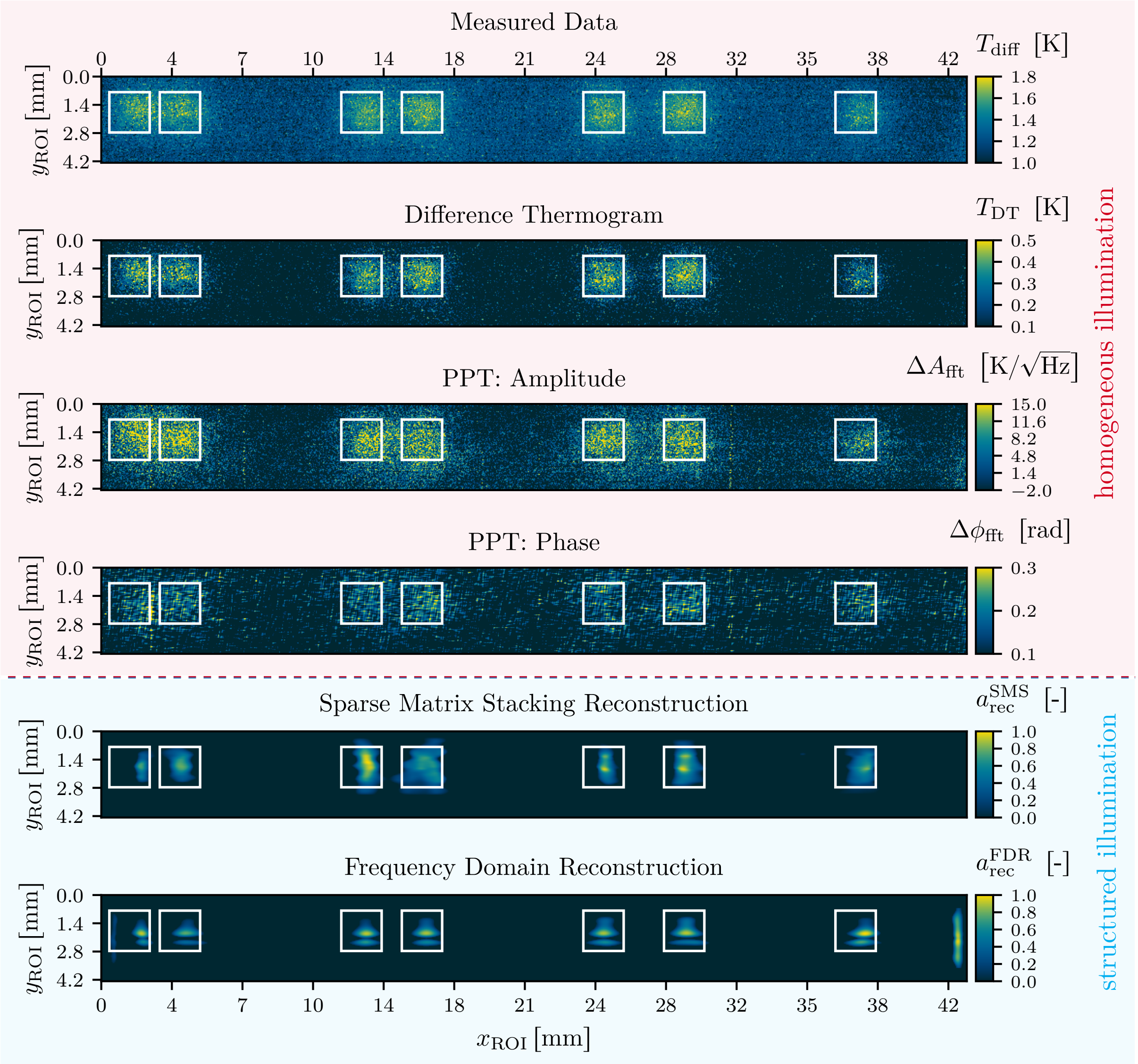

Figure 6.2: Qualitative comparison of the reconstruction results obtained via the sequential laser scanning approach with well-established TT reference methods based on homogeneous heating of the ROI (cf. Figure 5.4): for setting the reconstruction results into context, the temperature difference T_{diff} for a homogeneous illumination of the ROI with a laser pulse with $t_{\mathrm{pulse}} = 500\,\mathrm{ms}$ and $\hat{Q} = 456\,\mathrm{W}$ in conjunction with further post-processed versions of this dataset are shown, namely, the result of difference thermography T_{DT} and phase and amplitude PPT images ΔA_{fft} and $\Delta\phi_{\mathrm{fft}}$ for the 2$^{\mathrm{nd}}$ frequency component ($f_{\mathrm{fft}} = 0.105\,\mathrm{Hz}$). The true defect positions are indicated by white boxes. A similar figure has already been published in [A3].

To better visualize the datasets presented in Figure 6.2, a sectional view at $y_{\mathrm{eval}} = 1.8\,\mathrm{mm}$ of the DT dataset and the amplitude of the PPT evaluation dataset is shown overlaid with the SR reconstruction $a_{\mathrm{rec}}^{\mathrm{SMS}}$ obtained by the sparse matrix stacking inversion technique in Figure 6.3.

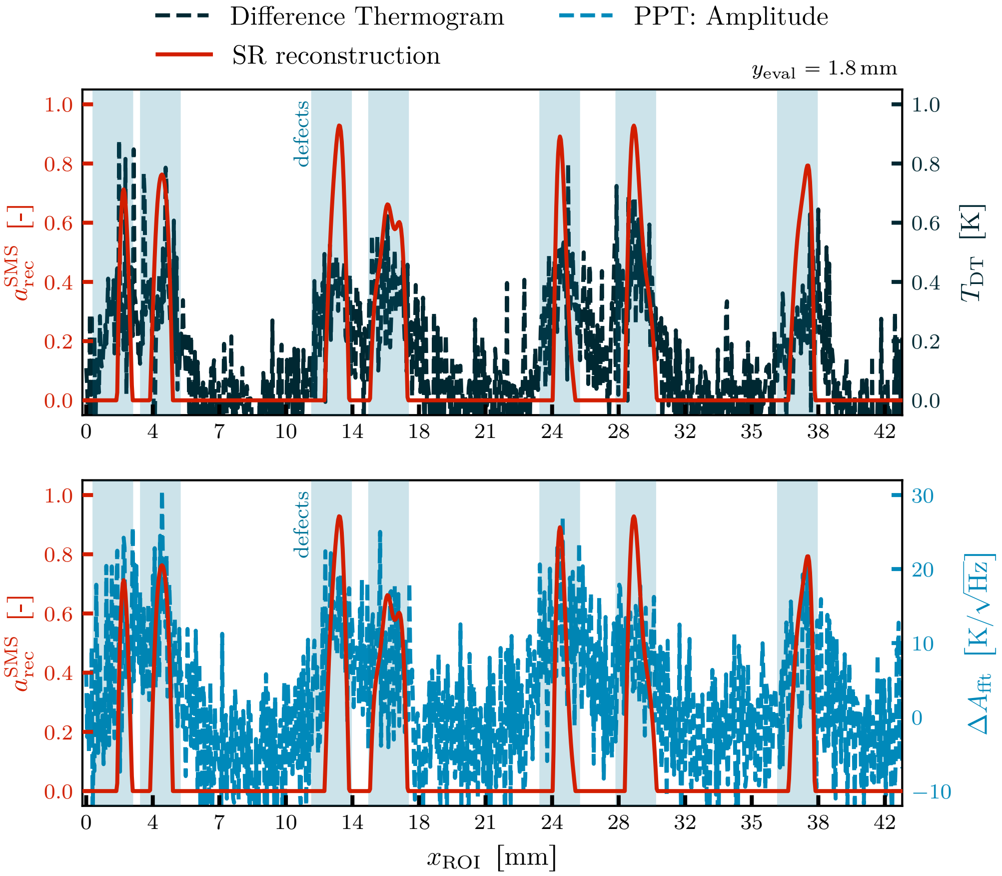

Figure 6.3: Sectional view of the difference thermography and PPT evaluation data presented in Figure 6.2 at $y_{\mathrm{eval}} = 1.8\,\mathrm{mm}$ overlaid with $a_{\mathrm{rec}}^{\mathrm{SMS}}$ obtained by the sparse matrix stacking inversion technique. Overlaying the inherently sparse SR reconstruction result further underlines the significant gain in contrast that can be achieved by SR reconstruction. The true defect positions are highlighted in blue color.

In order to quantify the differences seen in the different datasets and to rank the different methods, inputting all datasets in the proposed comparison metrics summarized in Table 6.1 leads to the values presented in Table 6.3.

Here, it can be observed that the SR reconstruction result obtained by the sparse matrix stacking inversion technique performs best according to the NMSE and R^2 metrics but performs slightly worse than the difference thermography result according to the Wasserstein metric. The sparse matrix stacking inversion technique has also overall (qualitatively and quantitatively) shown to outperform the frequency domain inversion technique when combined with coarse measurement grids for data obtained with the sequential laser scanning experimental approach.

Table 6.3: Comparison metrics results for the SR reconstructions obtained by the sequential laser scanning experimental approach for sparse matrix stacking inversion ($a_{\mathrm{rec}}^{\mathrm{SMS}}$) and frequency domain inversion ($a_{\mathrm{rec}}^{\mathrm{FDR}}$). The result for the best performing dataset for each metric is underlined and colored blue.

Metric	**Datasets**					
	T_{diff}	T_{DT}	ΔA_{fft}	$\Delta\phi_{\mathrm{fft}}$	$a_{\mathrm{rec}}^{\mathrm{SMS}}$	$a_{\mathrm{rec}}^{\mathrm{FDR}}$
$\mathrm{NMSE}_{\mathrm{eval}}$	2.42	0.85	1.03	0.94	0.78	0.96
R^2_{eval}	−1.42	0.15	−0.03	0.06	0.22	0.04
$\mathcal{W}_{\mathrm{eval}}$	11.66	2.91	3.77	3.15	3.04	3.29

6.3 Two-dimensional Pattern Projection

While the achieved reconstruction results by the sequential laser scanning approach were sufficient for a first proof of concept for two-dimensional SR reconstruction, the achieved reconstruction quality so far after investing reasonable experimental efforts leaves still room for improvement. Thus, the two-dimensional pattern projection experimental approach has been developed, analyzed and optimized, culminating in the exemplary reconstruction results already presented in Figure 5.11.

Acquiring the difference temperature T_{diff} after homogeneous illumination of the ROI utilized for two-dimensional pattern projection in the same setup projecting a single pattern with $\beta = 1$ (all pixels activated) at maximum output power ($\hat{Q} = 86\,\mathrm{W}$) of the projector and performing the selected post-processing methods (PPT and DT) for reference, leads to the datasets as presented in Figure 6.4.

While especially the amplitude image of the PPT and the DT results show a clear defect contrast improvement when compared with the initial dataset, qualitatively, both of these conventional methods are clearly outperformed by the SR reconstruction. The achieved reconstruction results shown features not only a perfectly sparse representation of the underlying defect map D, but also correctly reconstructed each defect with a high form accuracy. Solely the rightmost defect in the ROI is not fully reconstructed, which can be attributed to it lying very close to the edge of the ROI and therefore the illuminated area, leading to insufficient information about this area and a beginning local violation of the SR homogeneity constraint (cf. Equation (2.74)).

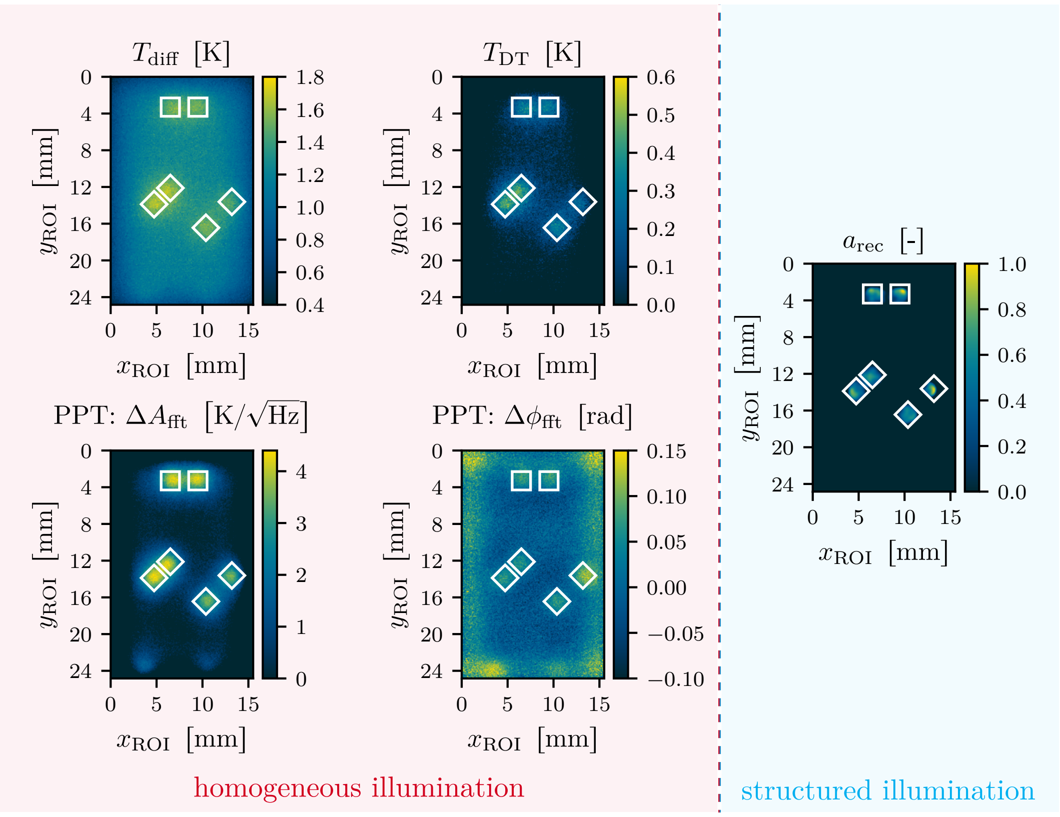

Figure 6.4: Qualitative comparison of the reconstruction results shown in Figure 5.11 obtained via the pattern projection approach with well-established TT methods based on homogeneous heating of the ROI serving as reference: for setting the obtained reconstruction results into context, the temperature difference T_{diff} for a homogeneous illumination of the ROI with a laser pulse with $t_{\mathrm{pulse}} = 500\,\mathrm{ms}$ in conjunction with further post-processed versions of this dataset are shown, namely, the result of difference thermography T_{DT} and phase and amplitude PPT images ΔA_{fft} and $\Delta\phi_{\mathrm{fft}}$ for the 3rd frequency component ($f_{\mathrm{fft}} = 0.516\,\mathrm{Hz}$). The laser power has been set to $\hat{Q} = 86\,\mathrm{W}$ in order to guarantee a fair comparison with the constrained output power capabilities of the utilized laser projector. The true defect positions are indicated by white boxes in each plot. A similar figure has already been published in [A2].

Figure 6.5 further illustrates these qualitatively outstanding results by showing a section of the different reconstructions at $y_{\mathrm{eval}} = 2.8\,\mathrm{mm}$, which intersects the upper defect pair featuring a separation distance of $d_{\mathrm{sep}} = 1\,\mathrm{mm}$. Both defects are well reconstructed in their respective shape and the separation distance is accurately reflected. Both conventional reference methods on the other hand only give an indication about the presence of the defect pair but severely lack information about the true defect shapes as can be expected by conventional non-diffusion corrected thermographic post-processing methods.

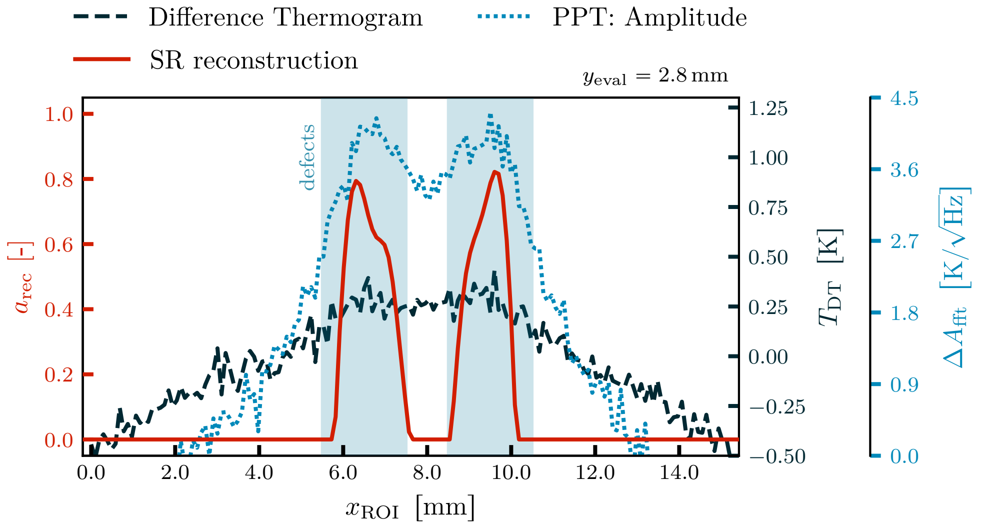

Figure 6.5: Sectional view of the difference thermography and PPT evaluation (amplitude) data presented in Figure 6.4 at $y_{\text{eval}} = 2.8\,\text{mm}$ overlaid with a_{rec} obtained via the frequency domain inversion approach. The defect pair centered in this section of the data is well reconstructed by the SR reconstruction result, while both conventional reference methods only vaguely indicate the true defect geometries. The true defect positions (defect pair with $d_{\text{sep}} = 1\,\text{mm}$) are highlighted in blue color. A similar figure has already been published in [A2].

When inputting all acquired data sets into the comparison metrics identified in Table 6.1, the results as shown in Table 6.4 are obtained. In this quantitative comparison, for the NMSE and R^2 metrics the SR-reconstructions clearly outperforms all reference methods by a large margin. Again, only for the Wasserstein metric $\mathcal{W}_{\text{eval}}$ the PPT phase image performs slightly better than the SR reconstruction. However, due to the high degree of sparsity of the true defect map within the ROI, both best performing methods according to the Wasserstein metric (SR reconstruction and the PPT phase image) perform close to a dataset containing all zeros (cf. Table 6.2). Therefore, the Wasserstein metric is less significant in this circumstance.

Table 6.4: Comparison metrics results for the SR reconstructions obtained by the two-dimensional pattern projection experimental approach for frequency domain inversion (a_{rec}). The result for the best performing dataset for each metric is underlined and colored blue.

Metric	**Datasets**				
	T_{diff}	T_{DT}	ΔA_{fft}	$\Delta\phi_{\text{fft}}$	a_{rec}
$\text{NMSE}_{\text{eval}}$	6.24	1.78	1.03	1.38	$\underline{0.59}$
R^2_{eval}	−5.24	−0.78	−0.03	−0.38	$\underline{0.41}$
$\mathcal{W}_{\text{eval}}$	6.20	1.80	0.93	$\underline{0.45}$	0.47

6.4 Key Result Summary and Observed Limitations

The following key observations have been made evaluating the different experimental results presented in Chapter 5 and the quantitative comparison of the achieved reconstruction results with well-established conventional TT post-processing techniques as presented in Chapter 6:

- True two-dimensional photothermal SR reconstruction has been achieved and the resulting sparse reconstruction of the underlying defect map outperforms representative well-established TT reference methods.
- Analytical studies given the novelly introduced forward solution and automated inversion represent a viable tool for parameter studies and optimization and their predictions withstand experimentally validation.
- The two-dimensional pattern projection experimental implementation approach has proven to at least reduce measurement efforts by a factor of 20× compared to the more traditional sequential laser scanning experimental approach.
- Quantitatively and qualitatively, the two-dimensional pattern projection experimental implementation approach has resulted in the best SR reconstruction of the true defect map.
- Frequency domain based inversion of the photothermal SR problem has shown to be the preferred inversion technique due to its better computational complexity and accurate reconstruction results given sufficient information density in the SR measurements.
- In contrast, the sparse matrix stacking inversion technique has proven to better suppress noise or false-positive signals (homogeneity constraint violations), but at high computational complexity.

Ultimately, the following limitations have been identified:

- Noise based quantitative comparison (SNR, SBR) of reconstruction results is not viable due to the sparse nature of the SR defect reconstruction.
- Frequency domain based inversion of the photothermal SR problem has proven to be less suited for very coarse measurement grids (cf. Figure 5.4; artifacts)
- A quantitative comparison of the results ideally requires a more sophisticated metric as well-established metrics cannot correctly quantify the sparsity benefit (cf. Table 6.2; all zeros dataset).

7. Conclusion and Outlook

7.1 Summary

Even though thermographic nondestructive testing (NDT) is a well-established method for detecting internal defects in several fields of industrial application, it inherently lacks in terms of the resolution of the shape of those defects. While this is a crucial aspect in the assessment of the impact of those defects on the object under test's (OuT's) specification, the diffusive nature of heat conduction sets a natural limit towards the achievable reconstruction quality for conventional thermographic NDT methods (cf. Section 3.1). Exceeding this limit is the main goal of thermographic super resolution (SR) methods, which achieve this goal by combining the information gathered from multiple differing measurements with spatially structured heating by applying mathematical optimization algorithms that exploit the use of physically relevant priors.

Starting from pre-existing foundational work on theorizing the principle of achieving a SR reconstruction of internal defects by means of the photothermal SR reconstruction method and foundational academic work to its application for the reconstruction of deeply-buried one-dimensional defect structures, the work conducted within this thesis elevated the method towards an applicability for two-dimensional regions of interest (ROIs) containing arbitrarily shaped defects, as it is the norm for most industrial application scenarios. In order to meet this challenge, the following achievements have been made:

The underlying severely ill-posed and heavily regularized inverse problem of photothermal SR reconstruction has been reformulated for two-dimensional ROIs and two distinct methods for its inversion have been proposed (sequential matrix stacking: cf. Section 4.1.1; inversion in frequency space: cf. Section 4.1.2), studied and put to the test.

From the ill-posed inverse problem a forward solution has been derived that allows for the generation of synthetic measurement data (cf. Section 4.3.1). In conjunction with the introduction of an automated method to determine the necessary regularization parameters for the photothermal SR reconstruction, these advances make it possible to make predictions about the performance of the method based on analytical simulations.

Utilizing those newly available tools, two exemplary numerical studies have been conducted in order to thoroughly investigate the influence of the number of conducted measurements and the pixel size of the laser illumination used for photothermal heating. For both parameters, their dependency on the achievable reconstruction quality has been analyzed in this way within a parameter space that could not have been feasibly covered prior by a purely experimental study (cf. Section 4.3.3).

On the practical side, the experimental implementation of photothermal SR reconstruction has been expanded to deal with arbitrarily sized two-dimensional ROIs. This has been achieved first by upgrading the already established sequential scanning approach towards the scanning of two-dimensional ROIs in a proof-of-concept phase (cf. Section 5.2.1). Subsequently, as the sequential scanning approach is not feasibly scalable to larger ROIs in practical use cases, the latest laser-coupled digital light processing (DLP) projector technology has been adapted to the method. This has required as an integral part of this work the planning, designing and procuring of the experimental setup and the extensive creation of software to facilitate the communication with the projector and its synchronization with all involved measurement equipment. Ultimately, the use of a DLP-projector has sped up the experimental implementation significantly (up to 20×; cf. Section 5.3.1) by projecting binary pixel patterns that cover the whole ROI. While there is some precedence to the use of DLP projectors in thermographic testing, their application within this thesis mark the first point where the application for testing macroscopic metallic objects has been proven feasible.

Utilizing this novelly adapted experimental strategy, all analytical results acquired have been put to the test and validated in dedicated measurement campaigns. Overall, as a high consistency between the measured data points and corresponding analytically generated data points could be observed, the proposed analytical simulation approach proved to be a successful tool to make predictions about the behavior of the method (cf. Section 5.3.3).

Furthermore, different ROIs of a purpose-made OuT have been thermographically tested for internal defects using the proposed two-dimensional photothermal SR reconstruction approach as well as several well-established thermographic reference methods based on homogeneous illumination. In direct qualitative and quantitative comparison, the proposed photothermal SR reconstruction approach has proven to significantly outperform the available reference methods in terms of shape reconstruction of the internal defects (cf. Chapter 6).

In conclusion, the research objectives as stated in Section 3.3 have been widely met and the accomplishments of this thesis can be summarized as follows:

- Laser-based photothermal SR reconstruction has been expanded to cope with two-dimensional ROIs encompassing arbitrarily shaped defects.
- Two different numerical methods for the inversion of the underlying severely ill-posed inverse problem have been proposed and successfully applied to experimentally acquired data.
- A proof-of-concept experimental approach has been implemented which is capable of investigating two-dimensional ROIs using standard equipment commonly found in laser-based active thermography. This experimental approach has already been able to prove a significant improvement of the achievable resolution of the reconstruction of internal defects.
- The experimental approach has been refined by the introduction of a state-of-the-art digital micromirror device (DMD)-based laser-coupled DLP-projector, which so far has only seen very limited use in thermography but enabled a significant reduction in the required experimental efforts at better reconstruction results.
- An analytical approach to simulating a photothermal SR reconstruction experiment has been derived, which allows studying the influence of different parameters on the reconstruction result accelerating the optimization of method and adaption to other experimental requirements.
- The analytical simulation has been automated by deriving a forward solution to the photothermal SR reconstruction inverse problem which allows for the generation of synthetic measurement data for arbitrary ROIs and defect distributions. Furthermore, the inversion of the ill-posed inverse problem has been automated by automatically determining the (optimal) set of regularization parameters for the inversion.
- Concomitantly, all findings have been thoroughly experimentally validated and all analytically obtained results could be recreated using experimentally acquired data.
- The technology readiness level (TRL) level of the method could be steadily improved from an initial TRL 3 to an estimated TRL 4–5 thanks to the work encompassed by this thesis.

7.2 Outlook

While the work culminating in this thesis has managed to increase the TRL of the method from an estimated TRL 3 to TRL 4–5, the current state of the photothermal SR reconstruction method has clearly not reached full maturity. The auspicious results that have been already obtained further corroborate that investing in further work to increase the TRL even more is well worth the effort.

Automated Photothermal Super Resolution Reconstruction

When trying to envision the next steps that naturally unfold, it is beneficial to illustrate the process of performing a photothermal SR reconstruction measurement as shown in Figure 7.1 (a).

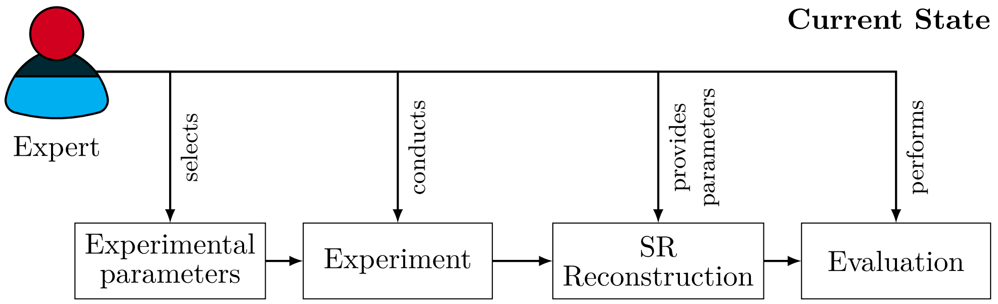

(a) Current state of the overall process behind two-dimensional photothermal SR reconstruction: as the method is still at TRL 4-5 after the improvements by the works of this thesis, a trained expert is still required for performing all individual steps.

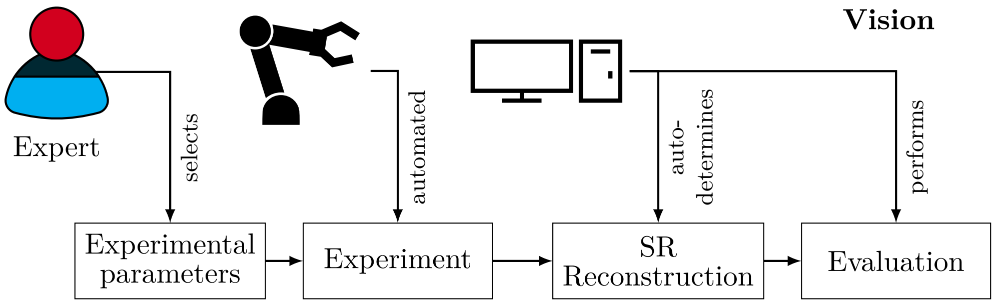

(b) Long-term vision for two-dimensional photothermal SR reconstruction: the involvement of trained experts is minimized such that the method can be viably used in an integrated Industry 4.0 environment.

Figure 7.1: Current state and vision for two-dimensional photothermal SR reconstruction

In its current state, all necessary steps to test a single OuT have to be performed by a trained expert. While this is acceptable for very highly specialized application fields where accuracy of the method is valued above the inherent cost, for wider application a larger degree of automation has to be introduced to the method. This necessary automation has to take several forms, as the different tasks to be performed feature their own unique set of requirements. On the practical side, the currently static experimental implementation of the method needs to be adapted to be able to deal with complex shaped OuTs, which requires automated manipulation of the OuT (e.g., by means of a robotic arm [95, 96]). On the data processing side, a substantial automation effort needs to be undertaken to be able to automatically determine suitable regularization parameters even for unknown OuTs, as this is currently the main bottleneck in every measurement campaign. Furthermore, the final evaluation of the achieved reconstruction result invites to be automated such that it can be performed algorithmically, as the significantly improved machine readability of the result is one of the major benefits of the photothermal SR reconstruction method compared to other available thermographic testing (TT) techniques.

The envisioned idealized future for the application of two-dimensional photothermal SR reconstruction measurements comprises the following steps, which are also displayed graphically in Figure 7.1 (b):

- Choose experimental parameters on basis of simulations (forward solution & numerical studies) suitable for the OuT/ROI at hand.
- Run a fully automated version of the experimental implementation suitable for OuTs with arbitrarily curved surfaces.
- Reconstruct the defects from the measurements with the optimal set of regularization parameters $\{\lambda_{2,1}, \lambda_2\}$, determined automatically from the measurements themselves (cf. first works by Ahmadi et al. [97] and Hauffen et al. [98]).
- Automatically evaluate the reconstruction results and process them further as part of the documentation of the OuT's lifecycle.

Further Experimental Improvement

The introduction of laser-coupled DLP-projectors to the photothermal SR reconstruction method lead to a massive improvement in reducing the experimental efforts while achieving high reconstruction quality. However, the limited power output of available DLP-projectors – even though constantly improving (cf. Appendix A4) – is problematic for resolving deeper defect depths. This influence on the depth at which defects can be detected is governed by the following points:

- The detectability of defects is closely bound to the achievable signal-to-noise ratio (SNR) of the individual measurements that are combined by the photothermal SR reconstruction algorithm. As the measurement noise is mostly fixed to the noise equivalent temperature difference (NETD) of the utilized infrared camera, increasing the signal amplitude is the only feasibly accessible way to increase the SNR. Thus, sufficiently strong photothermal heating is required (i.e., high irradiance on the ROI and therefore high optical output power of the projector).

- As the method is formulated to utilize short pulses (i.e., $t_{\text{pulse}} \ll t_{\text{diff}}(L_{\text{defect}})$), especially for thermally fast materials (high thermal diffusivity α) the duration of the illumination should be kept short. This further limits the photothermally deposited energy.
- The thermal signal strength decays with $\propto (\alpha\, t)^{-3/2}$ (cf. Equation (2.17)). Therefore, for a sufficient SNR for the detection of deeply-buried defects, substantial initial heating is necessary such that at $t \approx t_{\text{diff}}(L_{\text{defect}})$ the SNR is still high enough.

In summary, the ideal photothermal heating comprises a short pulse at high irradiance such that sufficient heating and therefore adequate SNR can be guaranteed. However, in reality, current DLP-technology quickly reaches its limits. The fact that the utilized approach consists of projecting patterns with significant white-content ($\beta \leqslant 0.5$), further limits the maximum possible deposited energy. As the DLP-technology at least needs to improve in this regard for another order of magnitude before the achievable irradiances cannot be considered the major bottleneck for the testing of thermally fast materials (like most metals) anymore, on the short to mid term scale another solution needs to bridge this gap.

An obvious solution would be provided by the utilization of more powerful illumination sources. While for a single DLP-projector the limits are already reached, the combination of multiple projectors similar to the three-chip design of modern consumer grade DLP-projectors could be a viable solution. While with three-chip based DLP-projectors the individual light sources with one DMD each are combined as individual color channels [99], in the proposed approach, several projectors could be combined to increase the overall irradiance on the ROI. Another possibility would be to directly combine multiple laser sources, such that each pixel of the illumination is facilitated by its own laser source. Such an approach can already be observed in experimental laser powder bed fusion (PBF-LB) setups, where each layer in the PBF-LB process is fused by a single-shot illumination utilizing an array of $\approx 10^6$ diode lasers (cf. EOS «LaserProFusion» technology [100]).

However, so far this process has not reached commercial maturity and such vast laser diode arrays are not yet available on the market. Until then, what is left would be to take advantage of the general versatility of laser-based active TT by combining the pattern projection approach with different photothermal techniques, introducing a temporal structuring of the illumination to increase the depth range of the defect detection. Temporal structuring has already proven to be a viable approach for increasing the depth range of TT and their experimental implementation can be easily superimposed onto the photothermal SR reconstruction problem. Possible temporal structuring methods for the photothermal excitation that are proposed to be investigated, comprise thermal wave radar [101], chirped pulse excitation [102] or pulse compression using coded excitation [103, 104].

Three-dimensional Photothermal SR Reconstruction

While this thesis has improved the photothermal SR reconstruction method from only operating on one-dimensional ROIs to being capable of reconstructing arbitrarily shaped defects in two-dimensional ROIs, the method still only outputs a two-dimensional defect map. With the vision of a photothermal computed tomography (CT) method in mind, the next step would be to extend the method to three-dimensional defect reconstruction. This can be tackled in several ways: one possibility would be to evaluate the current "planar" version of the photothermal SR reconstruction problem for multiple depths by choosing multiple t_{eval} values (corresponding to multiple diffusion lengths according to Equation (2.13)) and perform one reconstruction each. Afterwards, the resulting defect maps could be combined into a single three-dimensional defect map. Another option would be to perform a continuous evaluation of the depth by extending the photothermal SR problem as follows (cf. Equation (2.71)):

$$\begin{aligned} T_{\text{diff}}(r, z^2/\alpha) &= \Phi_{\text{PSF}}(r, z^2/\alpha) *_r \ (a_{\text{ext}}(r) + a_{\text{int}}(r, z)) \\ &= \Phi_{\text{PSF}}(r, z^2/\alpha) *_r \ a(r, z) \end{aligned} \quad . \tag{7.1}$$

On the downside, the introduction of the depth information will increase the sparsity of the defect map and therefore further increase the ill-posedness of the problem, which in conjunction with the increased computational complexity will make the reconstruction problem even more challenging. However, the introduction of depth information will also increase the information content of the measurements and therefore the potential increasing the reliability of the method for the reconstruction of complex defects in demanding testing scenarios.

Another possibility would be to extend the photothermal SR reconstruction problem to three-dimensional defect reconstruction by adding depth information via the virtual wave (VW) transformation, which is a well suited post-processing technique to increase the depth resolution of active TT [105]. Ultimately, the results from the photothermal SR reconstruction and additional post-processing of the initially acquired thermographic data based on the VW transformation could be fused together to yield a high-resolution three-dimensional defect reconstruction.

Appendices

A1. Derivation of the Fourier Transform of the Thermal Point Spread Function

The continuous Fourier transform of the Green's function of the heat partial differential equation (PDE), as stated in Equation (2.17), evaluated at the diffusion time $t = {}^{L^2}\!/\!_{\alpha}$ for a penetration depth of L can be derived as follows:

$$\mathcal{F}\left[G_{\text{heat}}(r, {}^{L^2}\!/\!_{\alpha})\right](\zeta_r) = \int\limits_{\infty}^{\infty} \frac{1}{\left(4\pi L^2\right)^{3/2}} \cdot \exp\left(-\frac{\|r\|_2^2}{4L^2}\right) \exp\left(2\pi i \zeta_r \|r\|_2\right)\, \mathrm{d}r \tag{A1.2}$$

$$= \frac{1}{\left(4\pi L^2\right)^{3/2}} \cdot \int\limits_{\infty}^{\infty} \exp\left(-\frac{\|r\|_2^2}{4L^2}\right) \Big[\cos\left(2\pi\zeta_r\|r\|_2\right) - i \sin\left(2\pi\zeta_r\|r\|_2\right)\Big]\, \mathrm{d}r \tag{A1.3}$$

$$= \frac{1}{\left(4\pi L^2\right)^{3/2}} \cdot \left[\int\limits_{\infty}^{\infty} \exp\left(-\frac{\|r\|_2^2}{4L^2}\right) \cos\left(2\pi\zeta_r\|r\|_2\right)\, \mathrm{d}r \right.$$
$$\left. - i \cdot \underbrace{\int\limits_{\infty}^{\infty} \exp\left(-\frac{\|r\|_2^2}{4L^2}\right) \sin\left(2\pi\zeta_r\|r\|_2\right)\, \mathrm{d}r}_{=\,0 \text{ as integrand is odd.}} \right] \tag{A1.4}$$

$$= \frac{1}{\left(4\pi L^2\right)^{3/2}} \cdot \int\limits_{\infty}^{\infty} \exp\left(-\frac{\|r\|_2^2}{4L^2}\right) \cos\left(2\pi\zeta_r\|r\|_2\right)\, \mathrm{d}r\ . \tag{A1.5}$$

Abramowitz and Stegun give the following identity [106, p. 302: Eq. 7.4.6]:

$$\int\limits_{0}^{\infty} \exp\left(-at^2\right) \cos\left(2xt\right)\, \mathrm{d}t = \frac{1}{2}\sqrt{\frac{\pi}{a}} \exp\left(-\frac{x^2}{a}\right) \qquad \text{for } \operatorname{Re}(a) > 0\ . \tag{A1.6}$$

Inserting Equation (A1.5) into Equation (A1.6) yields the following:

$$\mathcal{F}\left[G_{\text{heat}}(r, {}^{L^2}\!/\!_{\alpha})\right](\zeta_r) = \frac{1}{2\pi L} \cdot \exp\left(-4\pi^2 L^2 \zeta_r^2\right)\ . \qquad \square \tag{A1.7}$$

A2. Derivation of the Fourier Transform of a Gaussian Beam Profile

The intensity profile of a Gaussian beam focused onto the x-y plane in cylindrical coordinates $r = \sqrt{x^2 + y^2}$ is given as:

$$I_{\mathrm{r,Gaussian}}(r, z = 0) = I_0 \cdot \exp\left(-\frac{2r^2}{d_{\mathrm{spot}}^2}\right) \;, \tag{A2.8}$$

with I_0 being the intensity at $I(r = 0, z = 0)$ and d_{spot} the $1/\mathrm{e}^2$ diameter of the intensity profile (spot size). The Fourier transform of Equation (A2.8) can be acquired in a similar argument to the one presented in Appendix A1. According to Equation (A1.6), $\mathcal{F}[I_{\mathrm{r,Gaussian}}](\zeta_r)$ for $a = 2/d_{\mathrm{spot}}^2$ is given as follows:

$$\int_0^\infty \exp\left(-at^2\right)\cos\left(2xt\right)\,\mathrm{d}t = \frac{1}{2}\sqrt{\frac{\pi}{a}}\exp\left(-\frac{x^2}{a}\right) \qquad \text{for } \mathrm{Re}(a) > 0 \tag{A2.9}$$

$$\Rightarrow \qquad \mathcal{F}[I_{\mathrm{r,Gaussian}}](\zeta_r) = \frac{I_0}{2}\sqrt{\frac{\pi d_{\mathrm{spot}}^2}{2}}\exp\left(\frac{-d_{\mathrm{spot}}^2\zeta_r^2}{2}\right) \;. \qquad \square \tag{A2.10}$$

A3. Derivation of the Thermal Sparrow Limit

If two thermal point spread functions (PSFs) are arranged at a separation distance of d next to each other, they are inseparable by definition of the Sparrow limit (cf. Section 2.2.1) if no minimum can be observed between them. This is true, if the following conditions are fulfilled:

$$\frac{\delta}{\delta r}\left(G_{\mathrm{sum}}(r = 0, L^2/\alpha)\right) = 0 \tag{A3.11}$$

$$\frac{\delta^2}{\delta r^2}\left(G_{\mathrm{sum}}(r = 0, L^2/\alpha)\right) \leqslant 0 \;, \tag{A3.12}$$

$$\text{where} \qquad G_{\mathrm{sum}}(r, L^2/\alpha) = G_{\mathrm{heat}}(r + d/2, L^2/\alpha) + G_{\mathrm{heat}}(r - d/2, L^2/\alpha) \;. \tag{A3.13}$$

The condition stated in Equation (A3.12) demands that the second derivative in space at the center of the two PSFs is less or equal to zero, which means that the sum of the two PSFs needs to still be concave or flat at this position leading to no observable minimum. For an extremum to occur in the first place, the first derivative also needs to equal zero as demanded by Equation (A3.11). The second derivative in space of $G_{\text{sum}}(r, {}^{L^2}\!/_{\alpha})$ is given as:

$$\frac{\delta^2}{\delta r^2}\left(G_{\text{sum}}(r, {}^{L^2}\!/_{\alpha})\right) = \frac{1}{\left(4\pi L^2\right)^{3/2}} \cdot \frac{\delta^2}{\delta r^2}\left(\exp\left(-\frac{\left(r+\frac{d}{2}\right)^2}{4L^2}\right) + \exp\left(-\frac{\left(r-\frac{d}{2}\right)^2}{4L^2}\right)\right) \tag{A3.14}$$

$$\begin{aligned} \Rightarrow \quad &= \frac{1}{\left(4\pi L^2\right)^{3/2}} \cdot \frac{\delta}{\delta r}\left(-\frac{(2r+d)\cdot\exp\left(-\frac{(2r+d)^2}{16L^2}\right)}{4L^2}\right. \\ &\qquad\qquad \left. + \frac{(-2r+d)\cdot\exp\left(-\frac{(-2r+d)^2}{16L^2}\right)}{4L^2}\right) \end{aligned} \tag{A3.15}$$

$$\begin{aligned} \Rightarrow \quad &= \frac{1}{\left(4\pi L^2\right)^{3/2}} \cdot \left(\frac{(4r^2+4r\,d+d^2-8L^2)\cdot\exp\left(-\frac{(2r+d)^2}{16L^2}\right)}{16L^4}\right. \\ &\qquad\qquad \left. + \frac{(4r^2-4r\,d+d^2-8L^2)\cdot\exp\left(-\frac{(-2r+d)^2}{16L^2}\right)}{16L^4}\right) \end{aligned} \tag{A3.16}$$

From Equation (A3.15) it can be already inferred that the condition for the first derivative to equal zero, as stated in Equation (A3.11), holds true for all separation distances d and diffusion lengths L:

$$\begin{aligned} &\frac{\delta}{\delta r}\left(G_{\text{sum}}(r, {}^{L^2}\!/_{\alpha})\right) = \\ &\frac{1}{\left(4\pi L^2\right)^{3/2}} \cdot \left(-\frac{(2r+d)\cdot\exp\left(-\frac{(2r+d)^2}{16L^2}\right)}{4L^2} + \frac{(-2r+d)\cdot\exp\left(-\frac{(-2r+d)^2}{16L^2}\right)}{4L^2}\right) \end{aligned} \tag{A3.17}$$

$$\begin{aligned} \Rightarrow \quad &\frac{\delta}{\delta r}\left(G_{\text{sum}}(r=0, {}^{L^2}\!/_{\alpha})\right) = \\ &\quad \frac{1}{\left(4\pi L^2\right)^{3/2}} \cdot \left(-\frac{d\cdot\exp\left(-\frac{d^2}{16L^2}\right)}{4L^2} + \frac{d\cdot\exp\left(-\frac{d^2}{16L^2}\right)}{4L^2}\right) = 0 \quad \forall d, L \end{aligned} . \tag{A3.18}$$

This thermal Sparrow Limit is then met, if the following inequality is fulfilled:

$$\frac{\delta^2}{\delta r^2}\left(G_{\text{sum}}(r=0, {}^{L^2}\!/_{\alpha})\right) \leqslant 0 \tag{A3.19}$$

$$\overset{\text{Eq. (A3.16)}}{\Rightarrow} \qquad \frac{1}{\left(4\pi L^2\right)^{3/2}} \cdot \frac{(d^2-8L^2)\cdot\exp\left(-\frac{d^2}{16L^2}\right)}{8L^4} \leqslant 0 \tag{A3.20}$$

$$\overset{L>0,\ d\geqslant 0}{\Rightarrow} \qquad d^2 - 8L^2 \leqslant 0 \tag{A3.21}$$

$$\Rightarrow \qquad d \leqslant 2\sqrt{2}L \qquad \square \tag{A3.22}$$

A4. Achievable Irradiances using DLP-based Projectors

DLP-based projectors are widely encountered in daily live as they are used to project all sorts of imagery (movies, presentations, etc.). One of the main key specifications of any projector is its brightness (emitted luminous flux Φ_v measured in Lumen [lm]), as it determines the image contrast and governs the visibility of the projected image with respect to the ambient lighting conditions. However, for considering their application for photothermal heating of objects, the emitted radiant flux Φ (measured in Watt [W]) is the required characteristic. Both are linked by the luminous efficacy $K(\lambda)$ [lm/W]:

$$K(\lambda) = \frac{\Phi_v}{\Phi} \, , \tag{A4.23}$$

which is modelled after the sensitivity curve of the human eye for daylight vision (cf. Figure A4.1) [108].

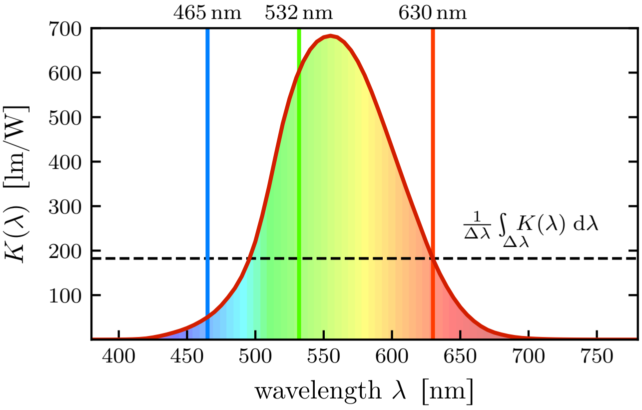

Figure A4.1: Spectral luminous efficacy $K(\lambda)$ of the human eye for photopic vision (well-lit conditions). The luminous efficacy correlates the photometric luminous flux (perceived brightness) to the radiometric radiant flux. $K(\lambda)$ has a maximum at $\lambda = 555\,\mathrm{nm}$ with $K(555\,\mathrm{nm}) = 683\,\mathrm{lm/W}$. For a true white light source, a mean value of $\int_\lambda K(\lambda)\,\mathrm{d}\lambda \approx 183\,\mathrm{lm/W}$ is reached, while white light that is created by the combination of red (630 nm), green (532 nm) and blue light (465 nm), achieves a luminous efficacy of $\approx 300\,\mathrm{lm/W}$.

Typical modern DLP-based projectors feature in the order of $\sim 1000\,\mathrm{lm}$ to $10000\,\mathrm{lm}$ of luminous flux exiting the projector depending on the built-in light source. Notably, the brightest laser projectors that are in public use are three-chip DLP laser projectors (one DLP and laser light source per color channel) featuring $\sim 55\,000\,\mathrm{lm}$ [99]. Those are used in the largest cinemas with screen sizes up to $\approx 500\,\mathrm{m}^2$. Due to them having independent laser light sources per color channel, they also offer high luminous efficacies of $\sim 300\,\mathrm{lm/W}$, leading to a total radiant flux of:

$$\Phi = \frac{50\,000\,\mathrm{lm}}{300\,\mathrm{lm/W}} \approx 167\,\mathrm{W}\ . \tag{A4.24}$$

While a radiant flux of 167 W is a quite a lot in the context of photothermal heating, these projectors are very costly, very large and weigh multiple hundred kilograms [99]. To achieve the irradiance values typically necessary to guarantee sufficient photothermal heating for higher conductivity materials such as metals ($10\,\mathrm{W/cm^2}$ to $100\,\mathrm{W/cm^2}$), the image of such a projector would need to be projected down to a total area of $16.7\,\mathrm{cm^2}$ to $1.67\,\mathrm{cm^2}$ to reach sufficient irradiance values, which ranges several magnitudes outside their contemplated area of operation. In contrast, most consumer grade laser-based DLP-projectors do not feature independent laser sources for each color channel and instead only come with a single laser light source that is used to handle several color channels at once. This drastically decreases the radiant flux to a point where it is hardly viable for macroscopic TT (microscopic applications exist, cf. [90]). An overview of different projector types is given in Table A4.1.

Table A4.1: Different projector types with typical brightness, radiant flux and max. ROI size to achieve sufficient irradiance for photothermal heating. For all projectors, a luminous efficacy of ≈ 300 lm/W is assumed [107, 109].

Projector	**Brightness**	**Radiant flux**	**projection area [cm²]**	
	typ. [lm]	typ. [W]	at $10\,\mathrm{W/cm^2}$	at $100\,\mathrm{W/cm^2}$
LED-based	∼ 1000	3	0.3	0.03
LCD-based	∼ 3000	10	1	0.1
DLP-based (standard)	∼ 8000	27	2.7	0.27
DLP-based (top tier)	∼ 50000	167	16.7	1.67
DLP-based (Fig. 5.7)	-	86	8.6	0.86

Table A4.1 also comprises the industrial grade DLP-projector utilized within this thesis (cf. Figure 5.7) for reference. As it is designed to be used with a NIR laser source, no brightness value can be attributed. However, it can be seen that for an affordable single chip design, it features a substantial radiant flux, which is only outmatched by the largest cinema projectors. However, as it is designed to be used for industrial applications it is much more adaptable to laboratory use.

Related Author’s Publications

The following publications have been published as a result of the research work culminating in this thesis:

Reviewed Journal Articles

[A1] **J. Lecompagnon**, P. Hirsch, C. Rupprecht and M. Ziegler. “Influence of the number of measurements on detecting internal defects using photothermal super resolution reconstruction with random pixel patterns”. In: *Quantitative InfraRed Thermography Journal* (June 6, 2023), pp. 1–11. DOI: 10.1080/17686733.2023.2223392.

[A2] **J. Lecompagnon**, P. D. Hirsch, C. Rupprecht and M. Ziegler. “Nondestructive thermographic detection of internal defects using pixel-pattern based laser excitation and photothermal super resolution reconstruction”. In: *Scientific Reports* 13.3416 (Feb. 28, 2023), pp. 1–13. DOI: 10.1038/s41598-023-30494-2.

[A3] **J. Lecompagnon**, S. Ahmadi, P. Hirsch, C. Rupprecht and M. Ziegler. “Thermographic detection of internal defects using 2D photothermal super resolution reconstruction with sequential laser heating”. In: *Journal of Applied Physics* 131.18, 185107 (May 2022). DOI: 10.1063/5.0088102.

[A4] S. Ahmadi, **J. Lecompagnon**, P. D. Hirsch, P. Burgholzer, P. Jung, G. Caire and M. Ziegler. “Laser excited super resolution thermal imaging for nondestructive inspection of internal defects”. In: *Scientific Reports* 10.22357 (Dec. 21, 2020). **BAM Paper of the Month 04/2021**, pp. 1–8. DOI: 10.1038/s41598-020-77979-y.

[A5] S. Ahmadi, G. Thummerer, S. Breitwieser, G. Mayr, **J. Lecompagnon**, P. Burgholzer, P. Jung, G. Caire and M. Ziegler. “Multidimensional Reconstruction of Internal Defects in Additively Manufactured Steel Using Photothermal Super Resolution Combined With Virtual Wave-Based Image Processing”. In: *IEEE Transactions on Industrial Informatics* 17.11 (Nov. 2021), pp. 7368–7378. DOI: 10.1109/tii.2021.3054411.

Conference Papers

[C1] **J. Lecompagnon**, P. Hirsch, C. Rupprecht and M. Ziegler. "Detektion innenliegender Defekte mittels photothermischer Super-Resolution-Rekonstruktion und 2D-Beleuchtungsmustern". In: *Thermographie-Kolloquium der Deutschen Gesellschaft für Zerstörungsfreie Prüfung (DGZfP).* Saarbrücken, Sept. 29, 2022. URN: urn:nbn:de:kobv:b43-565222 .

[C2] **J. Lecompagnon**, P. Hirsch, C. Rupprecht and M. Ziegler. "Detection of internal defects applying photothermal super resolution reconstruction utilizing two-dimensional high-power random pixel patterns". In: *Proceedings of the 2022 International Conference on Quantitative InfraRed Thermography.* Best Student Paper Award Nominee. QIRT Council, July 4, 2022. DOI: 10.21611/qirt.2022.1005.

[C3] **J. Lecompagnon**, P. Hirsch, C. Rupprecht and M. Ziegler. "Hochaufgelöste thermografische Detektion eingeschlossener Defekte mit Hilfe von 2D-strukturierten Beleuchtungsmustern". In: *Jahrestagung der Deutschen Gesellschaft für Zerstörungsfreie Prüfung (DGZfP).* Vol. BB 177. Kassel, May 24, 2022. URL: https://jahrestagung.dgzfp.de/portals/jt2022/bb177/inhalt/di.1.a.3.pdf.

[C4] **J. Lecompagnon**, P. Hirsch, C. Rupprecht and M. Ziegler. "Thermographic testing using 2D pseudo-random illumination and photothermal super resolution reconstruction". In: *Thermosense: Thermal Infrared Applications XLIV.* Ed. by A. Mendioroz and N. P. Avdelidis. Vol. 12109. **Awarded with the Best Student Paper Award**. International Society for Optics and Photonics. SPIE, May 2022, pp. 10–18. DOI: 10.1117/12.2618562.

[C5] **J. Lecompagnon**, S. Ahmadi, P. Hirsch, C. Rupprecht and M. Ziegler. "Investigations on photothermal super resolution reconstruction using 2D-structured illumination patterns". In: *SPIE Future Sensing Technologies 2021.* Ed. by M. Kimata, J. A. Shaw and C. R. Valenta. Vol. 11914. International Society for Optics and Photonics. SPIE, Nov. 2021, pp. 124–131. DOI: 10.1117/12.2603838.

[C6] **J. Lecompagnon**, S. Ahmadi, P. D. Hirsch and M. Ziegler. "2D-Photothermal super resolution with sparse matrix stacking". In: *SMSI 2021 - Sensors and Instrumentation.* AMA Service GmbH, Von-Münchhausen-Str. 49, 31515 Wunstorf, Germany, May 4, 2021. Chap. C2 IRS^2 Satellite Conference: Infrared Sensor Applications: Non-destructive Testing, Spectroscopy, pp. 183–184. DOI: 10.5162/SMSI2021/C2.2.

[C7] **J. Lecompagnon**, S. Ahmadi, P. Hirsch and M. Ziegler. "Full-frame thermographic super-resolution with 2D-structured laser heating". In: *Thermosense: Thermal Infrared Applications XLIII*. Ed. by J. N. Zalameda and A. Mendioroz. Vol. 11743. International Society for Optics and Photonics. SPIE, Apr. 2021, pp. 200–208. DOI: 10.1117/12.2586093.

Presented Scientific Posters

[P1] **J. Lecompagnon**, P. Hirsch, C. Rupprecht and M. Ziegler. *Thermographic super resolution reconstruction using 2D pseudo-random pattern illumination.* ICPPP21 International Conference on Photoacoustic and Photothermal Phenomena. June 21, 2022. URN: urn:nbn:de:kobv:b43-551224 .

[P2] **J. Lecompagnon**, S. Ahmadi, P. Hirsch and M. Ziegler. *Thermografische Super Resolution mit 2D-strukturierter Erwärmung.* Jahrestagung der Deutschen Gesellschaft für Zerstörungsfreie Prüfung (DGZfP). May 11, 2021. URN: urn:nbn:de:kobv:b43-526396 .

References

[1] P. Cawley. “Non-destructive testing — current capabilities and future directions”. In: *Proceedings of the Institution of Mechanical Engineers, Part L: Journal of Materials: Design and Applications* 215.4 (Oct. 2001), pp. 213–223. DOI: 10.1177/146442070121500403.

[2] G. Maritz. *Advancing industrial plant advantage. Driving industrial plant performance through advanced NDT methods.* en. Tech. rep. TÜV SÜD AG, 2019. 12 pp. URL: https://www.tuvsud.com/en-gb/-/media/global/pdf-files/whitepaper-report-e-books/tuvsud-advancing-industrial-plant-advantage.pdf (visited on 05/30/2023).

[3] DIN EN ISO 9712:2022-09. *Non-destructive testing - Qualification and certification of NDT personnel (ISO 9712:2021).* Tech. rep. Sept. 2022. DOI: https://dx.doi.org/10.31030/3301059.

[4] European Federation for NDT (EFNDT). *List of EFNDT Member Associations.* May 30, 2023. URL: https://www.efndt.org/Members.

[5] M. Gupta, M. A. Khan, R. Butola and R. M. Singari. “Advances in applications of Non-Destructive Testing (NDT): A review”. In: *Advances in Materials and Processing Technologies* 8.2 (Apr. 2021), pp. 2286–2307. DOI: 10.1080/2374068x.2021.1909332.

[6] V. Vavilov. “Thermal NDT: historical milestones, state-of-the-art and trends”. In: *Quantitative InfraRed Thermography Journal* 11.1 (Jan. 2014), pp. 66–83. DOI: 10.1080/17686733.2014.897016.

[7] F. Khodayar, S. Sojasi and X. Maldague. “Infrared thermography and NDT: 2050 horizon”. In: *Quantitative InfraRed Thermography Journal* 13.2 (July 2016), pp. 210–231. DOI: 10.1080/17686733.2016.1200265.

[8] Deutsches Kupferinstitut. *Werkstoffdatenblatt: Cu-OFE.* 2019. URL: https://kupfer.de/wp-content/uploads/2019/11/Cu-OFE.pdf (visited on 11/25/2022).

[9] thyssenkrupp Materials Services GmbH. *Werkstoffdatenblatt: Aluminiumlegierung: AlMgSi0.5.* 2017. URL: https://de.materials4me.com/media/pdf/26/7e/8c/Werkstoffdatenblatt_zum_Werkstoff_EN_AW-6060.pdf (visited on 11/25/2022).

[10] thyssenkrupp Materials Services GmbH. *Werkstoffdatenblatt: Warmgewalzter unlegierter Baustahl: S235JR.* 2017. URL: https://de.materials4me.com/media/pdf/e7/7d/30/Werkstoffdatenblatt_zum_Werkstoff_S235JR.pdf (visited on 11/25/2022).

[11] thyssenkrupp Materials Services GmbH. *Werkstoffdatenblatt: Austenitischer korrosionsbeständiger Stahl: 1.4301.* 2017. URL: http://www.otto-online.de/media/files/1.4301-werkstoffdatenblatt.pdf (visited on 11/25/2022).

[12] Wefapress Beck + Co. GmbH. *Technisches Datenblatt: POM.* 2020. URL: https://www.wefapress.com/sites/default/files/wim/downloads/de/PEEK-Datenblatt.pdf (visited on 11/25/2022).

[13] Wefapress Beck + Co. GmbH. *Technisches Datenblatt: PEEK.* 2020. URL: https://www.wefapress.com/sites/default/files/wim/downloads/de/POM-Datenblatt.pdf (visited on 11/25/2022).

[14] J. C. Dixon. "Appendix B: Properties of Air". In: *The Shock Absorber Handbook.* John Wiley & Sons, Ltd, Sept. 14, 2007, pp. 375–378. ISBN: 9780470516430. DOI: https://doi.org/10.1002/9780470516430.app2.

[15] J. Fourier. *Théorie analytique de la chaleur.* Chez Firmin Didot, père et fils, 1822. DOI: 10.3931/e-rara-19706.

[16] A. Fick. "Ueber Diffusion". In: *Annalen der Physik und Chemie* 170.1 (1855), pp. 59–86. DOI: 10.1002/andp.18551700105.

[17] K. Cole, J. Beck, A. Haji-Sheikh and B. Litkouhi. *Heat Conduction Using Greens Functions.* CRC Press, July 2010. DOI: 10.1201/9781439895214.

[18] D. G. Duffy. *Green's Functions with Applications.* Chapman and Hall/CRC, Mar. 2015. DOI: 10.1201/9781315371412.

[19] DIN EN 16714-1:2016-11. *Non-destructive testing - Thermographic testing - Part 1: General principles.* Tech. rep. Nov. 2016. DOI: https://dx.doi.org/10.31030/2415706.

[20] DIN EN 17119:2018-10. *Non-destructive testing - Thermographic testing - Active thermography.* Tech. rep. Oct. 2018. DOI: https://dx.doi.org/10.31030/2868198.

[21] W. J. Parker, R. J. Jenkins, C. P. Butler and G. L. Abbott. "Flash Method of Determining Thermal Diffusivity, Heat Capacity, and Thermal Conductivity". In: *Journal of Applied Physics* 32.9 (Sept. 1961), pp. 1679–1684. DOI: 10.1063/1.1728417.

[22] R. Krankenhagen and C. Maierhofer. "Measurement of the radiative energy output of flash lamps by means of thermal thin probes". In: *Infrared Physics & Technology* 67 (Nov. 2014), pp. 363–370. DOI: 10.1016/j.infrared.2014.07.012.

[23] R. Krankenhagen and S. J. Altenburg. "Transient behaviour of the energy release after the discharge of flash lamps – A consideration of the afterglow". In: *Infrared Physics & Technology* 119 (Dec. 2021), p. 103951. DOI: 10.1016/j.infrared.2021.103951.

[24] M. Ziegler, E. Thiel and T. Studemund. "Thermography using a 1D laser array – From planar to structured heating". In: *Materials Testing* 60.7-8 (July 2018), pp. 749–757. DOI: 10.3139/120.111209.

[25] DIN EN ISO 9-1:2021-01. *Safety of machinery - Laser processing machines - Part 1: Laser safety requirements (ISO 11553-1:2020).* Tech. rep. Jan. 2021. DOI: https://dx.doi.org/10.31030/3115536.

[26] K. Garrity. *NIST ITS-90 Thermocouple Database - SRD 60.* 2000. DOI: 10.18434/T4S888. URL: https://srdata.nist.gov/its90/main/its90_main_page.html (visited on 12/08/2022).

[27] DIN EN 60751:2009-05. *Industrial platinum resistance thermometers and platinum temperature sensors (IEC 60751:2008).* Tech. rep. May 2009. DOI: https://dx.doi.org/10.31030/1507857.

[28] M. Planck. "Ueber das Gesetz der Energieverteilung im Normalspectrum". In: *Annalen der Physik* 309.3 (1901), pp. 553–563. DOI: 10.1002/andp.19013090310.

[29] W. Wien. "Eine neue Beziehung der Strahlung schwarzer Körper zum zweiten Hauptsatz der Wärmetheorie". In: *Sitzungsberichte der Königlich Preussischen Akademie der Wissenschaften zu Berlin.* Vol. 1. Königlich Preussische Akademie der Wissenschaften zu Berlin, 1883, pp. 55–62.

[30] E. Tiesinga, P. J. Mohr, D. B. Newell and B. N. Taylor. "CODATA recommended values of the fundamental physical constants: 2018". In: *Reviews of Modern Physics* 93.2 (June 2021), p. 025010. DOI: 10.1103/revmodphys.93.025010.

[31] J. H. Lambert. *Lamberts Photometrie (Photometria sive de mensura et gradibus luminis colorum et umbrae (1760)).* German. Ed. by E. Anding. Ausgaben 31-33 von Ostwalds Klassiker der exakten Wissenschaften Nr. 33. W. Engelmann, 1892.

[32] H. S. Carslaw and J. C. Jaeger. *Conduction of heat in solids.* Second Edition. Oxford University Press, 1959.

[33] S. M. Shepard. "Advances in pulsed thermography". In: *Thermosense XXIII.* Ed. by A. E. Rozlosnik and R. B. Dinwiddie. SPIE, Mar. 23, 2001. DOI: 10.1117/12.421032.

[34] D. L. Balageas, J.-M. Roche, F.-H. Leroy, W.-M. Liu and A. M. Gorbach. "The thermographic signal reconstruction method: A powerful tool for the enhancement of transient thermographic images". In: *Biocybernetics and Biomedical Engineering* 35.1 (2015), pp. 1–9. DOI: 10.1016/j.bbe.2014.07.002.

[35] X. P. V. Maldague and S. Marinetti. "Pulse phase infrared thermography". In: *Journal of Applied Physics* 79.5 (Mar. 1996), pp. 2694–2698. DOI: 10.1063/1.362662.

[36] C. Ibarra-Castanedo and X. P. V. Maldague. "Pulsed phase thermography reviewed". In: *Quantitative InfraRed Thermography Journal* 1.1 (June 2004), pp. 47–70. DOI: 10.3166/qirt.1.47-70.

[37] G. Busse and A. Rosencwaig. "Subsurface imaging with photoacoustics". In: *Applied Physics Letters* 36.10 (May 1980), pp. 815–816. DOI: 10.1063/1.91327.

[38] C. Ibarra-Castanedo, J.-M. Piau, S. Guilbert, N. P. Avdelidis, M. Genest, A. Bendada and X. P. V. Maldague. “Comparative Study of Active Thermography Techniques for the Nondestructive Evaluation of Honeycomb Structures”. In: *Research in Nondestructive Evaluation* 20.1 (Jan. 2009), pp. 1–31. DOI: 10.1080/09349840802366617.

[39] C. M. Sparrow. “On Spectroscopic Resolving Power”. In: *The Astrophysical Journal* 44 (Sept. 1916), p. 76. DOI: 10.1086/142271.

[40] W. J. Smith. *Practical Optical System Layout: And Use of Stock Lenses.* McGraw-Hill Education, 1997. ISBN: 9780070592544.

[41] K. Fliegel. “Modeling and Measurement of Image Sensor Characteristics”. In: *Radioengineering* 13.4 (Dec. 2004), pp. 27–34. ISSN: 1805-9600.

[42] M. Ben-Ezra, A. Zomet and S. K. Nayar. “Video super-resolution using controlled subpixel detector shifts”. In: *IEEE Transactions on Pattern Analysis and Machine Intelligence* 27.6 (June 2005), pp. 977–987. DOI: 10.1109/tpami.2005.129.

[43] M. S. Alam, J. G. Bognar, R. C. Hardie and B. J. Yasuda. “Infrared image registration and high-resolution reconstruction using multiple translationally shifted aliased video frames”. In: *IEEE Transactions on Instrumentation and Measurement* 49.5 (2000), pp. 915–923. DOI: 10.1109/19.872908.

[44] E. Mandanici, L. Tavasci, F. Corsini and S. Gandolfi. “A multi-image super-resolution algorithm applied to thermal imagery”. In: *Applied Geomatics* 11.3 (Feb. 2019), pp. 215–228. DOI: 10.1007/s12518-019-00253-y.

[45] F. Göttfert, J. Bohm, K. Heisig, G. Dammass and M. Krauß. “Optimizing microscan for radiometry with cooled IR cameras.”. In: *Infrared Imaging Systems: Design, Analysis, Modeling, and Testing XXX*. Ed. by K. A. Krapels and G. C. Holst. SPIE, May 2019. DOI: 10.1117/12.2519933.

[46] X. Zhang, C. Li, Q. Meng, S. Liu, Y. Zhang and J. Wang. “Infrared Image Super Resolution by Combining Compressive Sensing and Deep Learning”. In: *Sensors* 18.8 (Aug. 2018), p. 2587. DOI: 10.3390/s18082587.

[47] S. W. Hell and J. Wichmann. “Breaking the diffraction resolution limit by stimulated emission: stimulated-emission-depletion fluorescence microscopy”. In: *Optics Letters* 19.11 (June 1994), p. 780. DOI: 10.1364/ol.19.000780.

[48] M. G. L. Gustafsson. “Surpassing the lateral resolution limit by a factor of two using structured illumination microscopy. SHORT COMMUNICATION”. In: *Journal of Microscopy* 198.2 (May 2000), pp. 82–87. DOI: 10.1046/j.1365-2818.2000.00710.x.

[49] M. G. L. Gustafsson, L. Shao, P. M. Carlton, C. J. R. Wang, I. N. Golubovskaya, W. Z. Cande, D. A. Agard and J. W. Sedat. “Three-Dimensional Resolution Doubling in Wide-Field Fluorescence Microscopy by Structured Illumination”. In: *Biophysical Journal* 94.12 (June 2008), pp. 4957–4970. DOI: 10.1529/biophysj.107.120345.

[50] M. Bouzin, M. Marini, A. Zeynali, M. Borzenkov, L. Sironi, L. D'Alfonso, F. Mingozzi, F. Granucci, P. Pallavicini, G. Chirico and M. Collini. "Photo-activated raster scanning thermal imaging at sub-diffraction resolution". In: *Nature Communications* 10.1 (Dec. 2019). DOI: 10.1038/s41467-019-13447-0.

[51] M. Marini, M. Bouzin, R. Scodellaro, L. D'Alfonso, L. Sironi, F. Granucci, F. Mingozzi, G. Chirico and M. Collini. "Quantitative active super-resolution thermal imaging: The melanoma case study". In: *Biomolecular Concepts* 13.1 (Jan. 2022), pp. 242–255. DOI: 10.1515/bmc-2022-0015.

[52] P. Burgholzer, T. Berer, J. Gruber and G. Mayr. "Super-resolution thermographic imaging using blind structured illumination". In: *Applied Physics Letters* 111.3 (July 2017), p. 031908. DOI: 10.1063/1.4995410.

[53] S. Ahmadi, P. Burgholzer, P. Jung, G. Caire and M. Ziegler. "Super resolution laser line scanning thermography". In: *Optics and Lasers in Engineering* 134 (Nov. 2020), p. 106279. DOI: 10.1016/j.optlaseng.2020.106279.

[54] S. Ahmadi. "Super resolution laser thermography using spatially and temporally structured heating". PhD thesis. Technische Universität Berlin, 2021. DOI: 10.14279/DEPOSITONCE-12017.

[55] S. K. Lau, D. P. Almond and P. M. Patel. "Transient thermal wave techniques for the evaluation of surface coatings". In: *Journal of Physics D: Applied Physics* 24.3 (Mar. 1991), pp. 428–436. DOI: 10.1088/0022-3727/24/3/029.

[56] T. W. Murray, M. Haltmeier, T. Berer, E. Leiss-Holzinger and P. Burgholzer. "Super-resolution photoacoustic microscopy using blind structured illumination". In: *Optica* 4.1 (Dec. 2016), p. 17. DOI: 10.1364/optica.4.000017.

[57] T. W. Murray, M. Haltmeier, T. Berer, E. Leiss-Holzinger and P. Burgholzer. "Supplement 1: Super-resolution photoacoustic microscopy using blind structured illumination". In: (Jan. 2017). DOI: 10.1364/OPTICA.4.000017.s001.

[58] X. P. V. Maldague. *Theory and Practice of Infrared Technology for Nondestructive Testing*. 2nd ed. John Wiley & Sons, Apr. 16, 2001. 704 pp. ISBN: 978-0-471-18190-3.

[59] X. P. V. Maldague and P. O. Moore. *Nondestructive Testing Handbook: Infrared and Thermal Testing*. 3rd ed. Nondestructive testing handbook. Amer Society for Nondestructive, 2001. ISBN: 9781571170811.

[60] D. P. Almond and S. G. Pickering. "An analytical study of the pulsed thermography defect detection limit". In: *Journal of Applied Physics* 111.9 (May 2012). DOI: 10.1063/1.4704684.

[61] P. Burgholzer and G. Hendorfer. “Limits of Spatial Resolution for Thermography and Other Non-destructive Imaging Methods Based on Diffusion Waves”. In: *International Journal of Thermophysics* 34.8-9 (Sept. 2013), pp. 1617–1632. DOI: 10.1007/s10765-013-1513-0.

[62] E. Marín. “Basic principles of thermal wave physicsand related techniques”. In: *Thermal Wave Physics and Related Photothermal Techniques: Basic Principles and Recent Developments*. Ed. by E. M. Moares. 2009, pp. 1–27. ISBN: 978-81-7895-401-1.

[63] P. Burgholzer. “Thermodynamic Limits of Spatial Resolution in Active Thermography”. In: *International Journal of Thermophysics* 36.9 (May 2015), pp. 2328–2341. DOI: 10.1007/s10765-015-1890-7.

[64] P. Burgholzer, T. Berer, M. Ziegler, E. Thiel, S. Ahmadi, J. Gruber, G. Mayr and G. Hendorfer. “Blind structured illumination as excitation for super-resolution photothermal radiometry”. In: *Quantitative InfraRed Thermography Journal* 17.4 (2020), pp. 268–278. DOI: 10.1080/17686733.2019.1655247.

[65] S. Ahmadi, P. Burgholzer, G. Mayr, P. Jung, G. Caire and M. Ziegler. “Photothermal super resolution imaging: A comparison of different thermographic reconstruction techniques”. In: *NDT& E International* 111 (Apr. 2020), p. 102228. DOI: 10.1016/j.ndteint.2020.102228.

[66] J. C. Mankins. *Technology Readiness Levels. A White Paper*. Research rep. Advanced Concepts Office - Office of Space Access and Technology - NASA, Apr. 6, 1995. URL: http://www.artemisinnovation.com/images/TRL_White_Paper_2004-Edited.pdf.

[67] P. Rodriguez. “Total Variation Regularization Algorithms for Images Corrupted with Different Noise Models: A Review”. In: *Journal of Electrical and Computer Engineering* 2013 (2013), pp. 1–18. DOI: 10.1155/2013/217021.

[68] F. Elsner and B. D. Wandelt. “Efficient Wiener filtering without preconditioning”. In: *Astronomy & Astrophysics* 549 (Jan. 2013). DOI: 10.1051/0004-6361/201220586.

[69] A. Beck and M. Teboulle. “A Fast Iterative Shrinkage-Thresholding Algorithm for Linear Inverse Problems”. In: *SIAM Journal on Imaging Sciences* 2.1 (Jan. 2009), pp. 183–202. DOI: 10.1137/080716542.

[70] S. Boyd. “Distributed Optimization and Statistical Learning via the Alternating Direction Method of Multipliers”. In: *Foundations and Trends in Machine Learning* 3.1 (2010), pp. 1–122. DOI: 10.1561/2200000016.

[71] P. C. Hansen. “REGULARIZATION TOOLS: A Matlab package for analysis and solution of discrete ill-posed problems”. In: *Numerical Algorithms* 6.1 (Mar. 1994), pp. 1–35. DOI: 10.1007/bf02149761.

[72] P. C. Hansen. “The L-curve and its use in the numerical treatment of inverse problems”. English. In: *Computational Inverse Problems in Electrocardiology*. Ed. by P. Johnston. Advances in Computational Bioengineering. WIT Press, 2000, pp. 119–142. ISBN: 978-1-85312-614-7.

[73] N. Parikh and S. Boyd. “Proximal Algorithms”. In: *Foundations and Trends in Optimization* 1.3 (Jan. 13, 2014), pp. 127–239. DOI: 10.1561/2400000003.

[74] Y.-L. Yu. “On Decomposing the Proximal Map”. In: *Advances in Neural Information Processing Systems*. Ed. by C. J. Burges, L. Bottou, M. Welling, Z. Ghahramani and K. Q. Weinberger. Vol. 26. Curran Associates, Inc., 2013. URL: https://proceedings.neurips.cc/paper/2013/file/98dce83da57b0395e163467c9dae521b-Paper.pdf.

[75] R. Yuster and U. Zwick. “Fast sparse matrix multiplication”. In: *ACM Transactions on Algorithms* 1.1 (July 2005), pp. 2–13. DOI: 10.1145/1077464.1077466.

[76] J. E. Bresenham. “Algorithm for computer control of a digital plotter”. In: *IBM Systems Journal* 4.1 (1965), pp. 25–30. DOI: 10.1147/sj.41.0025.

[77] P. Jaccard. “The Distribution Of The Flora In The Alpine Zone”. In: *New Phytologist* 11.2 (Feb. 1912), pp. 37–50. DOI: 10.1111/j.1469-8137.1912.tb05611.x.

[78] Z. Wang, A. C. Bovik, H. R. Sheikh and E. P. Simoncelli. “Image Quality Assessment: From Error Visibility to Structural Similarity”. In: *IEEE Transactions on Image Processing* 13.4 (Apr. 2004), pp. 600–612. DOI: 10.1109/tip.2003.819861.

[79] A. Saberironaghi, J. Ren and M. El-Gindy. “Defect Detection Methods for Industrial Products Using Deep Learning Techniques: A Review”. In: *Algorithms* 16.2 (Feb. 2023), p. 95. DOI: 10.3390/a16020095.

[80] R. Storn and K. Price. “Differential Evolution - A Simple and Efficient Heuristic for global Optimization over Continuous Spaces”. In: *Journal of Global Optimization* 11.4 (1997), pp. 341–359. DOI: 10.1023/a:1008202821328.

[81] R. Storn. “On the usage of differential evolution for function optimization”. In: *Proceedings of North American Fuzzy Information Processing*. IEEE, June 1996. DOI: 10.1109/nafips.1996.534789.

[82] A. P. Piotrowski. “Review of Differential Evolution population size”. In: *Swarm and Evolutionary Computation* 32 (Feb. 2017), pp. 1–24. DOI: 10.1016/j.swevo.2016.05.003.

[83] Erpro Group - SAS. *Material Data Sheet Stainless Steel 316L / 1.4404 / A276*. 2019. URL: https://erpro-group.com/wp-content/uploads/2019/04/Fe_316L.pdf.

[84] ASM International. *Materials and coatings for medical devices: cardiovascular*. Materials and processes for medical devices. Page 135. Materials Park, Ohio: ASM International, 2009. ISBN: 9781615030002.

[85] A. C. Varela. “Characterization ofvertical cracks using lock-in vibrothermography”. PhD thesis. Universidad del Pais Vasco (UPV/EHU), 2017. URL: https://www.ehu.eus/photothermal/TesisAlazneCastelo.

[86] A. Ravichandran. “Spatial and temporal modulation of heat source using light modulator for advanced thermography”. MA thesis. Missouri University of Science and Technology, Department of Mechanical and Aerospace Engineering, 2015. 60 pp. URL: https://scholarsmine.mst.edu/masters_theses/7411.

[87] E. Thiel, M. Kreutzbruck and M. Ziegler. “Spatial and temporal control of thermal waves by using DMDs for interference based crack detection”. In: *SPIE Proceedings*. Ed. by M. R. Douglass, P. S. King and B. L. Lee. SPIE, Mar. 2016. DOI: 10.1117/12.2210918.

[88] J. D. Pribe, S. C. Thandu, Z. Yin and E. C. Kinzel. “Toward DMD illuminated spatial-temporal modulated thermography”. In: *SPIE Proceedings*. Ed. by J. N. Zalameda and P. Bison. SPIE, May 2016. DOI: 10.1117/12.2223859.

[89] E. Thiel and M. Ziegler. “Subsurface defect localization by structured heating using laser projected photothermal thermography”. In: *Journal of Visualized Experiments* 123 (May 2017). DOI: 10.3791/55733.

[90] Q. Zheng, D. Chalise, M. Jia, Y. Zeng, M. Zeng, M. Saeidi-Javash, A. N. M. Tanvir, G. Uahengo, S. Kaur, J. E. Garay, T. Luo, Y. Zhang, R. S. Prasher and C. Dames. “Structured illumination with thermal imaging (SI-TI): A dynamically reconfigurable metrology for parallelized thermal transport characterization”. In: *Applied Physics Reviews* 9.2 (June 2022), p. 021411. DOI: 10.1063/5.0079842.

[91] Texas Instruments Inc. *Datasheet: DLP650LNIR 0.65 NIR WXGA S450 DMD*. Nov. 2018. URL: https://www.ti.com/lit/gpn/dlp650lnir (visited on 04/11/2023).

[92] D. P. Almond and P. M. Patel. *Photothermal Science and Techniques*. Chapman & Hall Series in Accounting and Finance. Springer Netherlands, 1996. ISBN: 9780412578809.

[93] R. Usamentiaga, C. Ibarra-Castanedo and X. Maldague. “More than Fifty Shades of Grey: Quantitative Characterization of Defects and Interpretation Using SNR and CNR”. In: *Journal of Nondestructive Evaluation* 37.2 (Mar. 2018). DOI: 10.1007/s10921-018-0479-z.

[94] N. Bonneel, J. Rabin, G. Peyré and H. Pfister. “Sliced and Radon Wasserstein Barycenters of Measures”. In: *Journal of Mathematical Imaging and Vision* 51.1 (Apr. 2014), pp. 22–45. DOI: 10.1007/s10851-014-0506-3.

[95] T. Schmidt, S. Dutta and T. Ullmann. “Production integrated NDT by means of automated Thermography”. In: *Proceedings of the 2012 International Conference on Quantitative InfraRed Thermography*. QIRT Council, 2012. DOI: 10.21611/qirt.2012.331.

[96] N. W. Pech-May, P. Hirsch and M. Ziegler. “Robot-assisted laser thermography: towards automatic characterization of surface defects”. In: *Proceedings of the 2022 International Conference on Quantitative InfraRed Thermography.* QIRT Council, 2022. DOI: 10.21611/qirt.2022.1002.

[97] S. Ahmadi, L. Kästner, J. C. Hauffen, P. Jung and M. Ziegler. “Photothermal-SR-Net: a customized deep unfolding neural network for photothermal super resolution imaging”. In: *IEEE Transactions on Instrumentation and Measurement* 71 (2022), pp. 1–9. DOI: 10.1109/tim.2022.3154803.

[98] J. C. Hauffen, L. Kästner, S. Ahmadi, P. Jung, G. Caire and M. Ziegler. “Learned block iterative shrinkage thresholding algorithm for photothermal super resolution imaging”. In: *Sensors* 22.15 (July 2022), p. 5533. DOI: 10.3390/s22155533.

[99] Barco N.V. *Datasheet: DP4K-60L Ultra-bright 6P RGB laser cinema projector for premium large screens.* Tech. rep. Feb. 24, 2021. URL: https://www.barco.com/services/website/en/ProductSpecSheet/ProductSpecSheetFile?productId=e34bc152-329c-4cb9-b56b-a92b065984dc (visited on 04/03/2023).

[100] EOS GmbH. *EOS LaserProFusion Technology.* June 5, 2023. URL: https://www.eos.info/en/innovations/3d-printing-of-the-future/laserpro-fusion.

[101] N. Tabatabaei and A. Mandelis. “Thermal-wave radar: A novel subsurface imaging modality with extended depth-resolution dynamic range”. In: *Review of Scientific Instruments* 80.3 (Mar. 2009), p. 034902. DOI: 10.1063/1.3095560.

[102] R. Mulaveesala and S. Tuli. “Implementation of frequency-modulated thermal wave imaging for non-destructive sub-surface defect detection”. In: *Insight - Non-Destructive Testing and Condition Monitoring* 47.4 (Apr. 2005), pp. 206–208. DOI: 10.1784/insi.47.4.206.63156.

[103] G. Silipigni, P. Burrascano, D. A. Hutchins, S. Laureti, R. Petrucci, L. Senni, L. Torre and M. Ricci. “Optimization of the pulse-compression technique applied to the infrared thermography nondestructive evaluation”. In: *NDT& E International* 87 (Apr. 2017), pp. 100–110. DOI: 10.1016/j.ndteint.2017.01.011.

[104] N. W. Pech-May, A. Paul and M. Ziegler. “Pulse-compression laser thermography using a modified Barker code: enhanced detection of subsurface defects”. In: *Thermosense: Thermal Infrared Applications XLIII.* Ed. by J. N. Zalameda and A. Mendioroz. SPIE, Apr. 2021. DOI: 10.1117/12.2586078.

[105] P. Burgholzer, M. Thor, J. Gruber and G. Mayr. “Three-dimensional thermographic imaging using a virtual wave concept”. In: *Journal of Applied Physics* 121.10 (Mar. 2017), p. 105102. DOI: 10.1063/1.4978010.

[106] M. Abramowitz and I. A. Stegun. *Handbook of Mathematical Functions with Formulas, Graphs, and Mathematical Tables.* Nr. 1972. Vol. Bd. 55. Applied mathematics series. U.S. Government Printing Office, 1968. ISBN: 9780160002021.

[107] DIAL GmbH. *Theoretical maximum luminous efficacy of white LEDs.* Apr. 4, 2023. URL: https://www.dial.de/en-GB/projects/efficiency-of-leds-the-highest-luminous-efficacy-of-a-white-led.

[108] International Commission on Illumination (CIE). *Selected Colorimetric Tables: 1964 standard colorimetric observer (data table).* Vienna, Austria, Oct. 24, 2007. URL: https://cie.co.at/technical-work/technical-resources (visited on 04/03/2023).

[109] K. Schulmeister and J. Daem. “Risk of retinal injury from «Risk Group 2» laser illuminated projectors”. In: *Journal of Laser Applications* 28.4 (Nov. 2016), p. 042002. DOI: 10.2351/1.4954930.

List of Figures, Tables and Algorithms

List of Figures

1.1 Selection of different NDT methods according to DIN EN ISO 9712:2022-09. . . 1

2.1 Defects, inhomogeneities and irregularities detectable by TT. 5
2.2 Internal defects, inhomogeneities and irregularities impeding heat flow. 7
2.3 OuT with simplified BCs typical for TT. 10
2.4 Principle of adding instationary BCs via a convolution with the Green's function. 11
2.5 Comparison between active and passive thermographic testing. 12
2.6 Schematic of a thermographic measurement setup using different types of photothermal excitation. 14
2.7 Scheme of a temperature measurement using a thermocouple. 15
2.8 Resistance thermometer measurement scheme. 16
2.9 Spectral radiance $L_\lambda(\lambda, T)$ of a black body radiator. 18
2.10 Lambertian surface emitting thermal radiation onto a detector positioned at a distance r. 19
2.11 Influence of the spectral sensitivity band of a radiometric detector. 20
2.12 Schematic structure of a bolometer. 21
2.13 Schematic of a CMOS-based detector. 22
2.14 Temperature evolution after a Dirac-like heating with one-dimensional heat flow. 24
2.15 Impact factors on the resolution of internal defects using active TT. 27
2.16 Modulation transfer function (MTF) of an ideal lens for different f-numbers. . . 29
2.17 Modulation transfer function (MTF) of the thermal diffusion $\mathrm{MTF}_{\mathrm{diffusion}}$ evaluated at different depths. 30
2.18 Modulation transfer function (MTF) of the Gaussian beam profile for different spot sizes d_{spot}. 32
2.19 Modulation transfer function (MTF) of the flat-top profile for different spot sizes d_{spot}. 33
2.20 Principle of geometric super resolution. 34

2.21 Principle of optical super resolution. 36
2.22 Defect model within photothermal SR. 38

3.1 Defect aspect ratio as defined within the context of TT. 43
3.2 Thermographic defect signals distorted by thermal diffusion. 44
3.3 Difference between propagating and diffusive energy transport. 46

4.1 Necessary transformation of the illumination strategy for sequential laser scanning. 58
4.2 Selection of the optimal measurement grid spacing. 60
4.3 Multiple simultaneous illuminations and measurement grid abstraction. 61
4.4 Schematic depiction of a binary pixelated illumination pattern and its properties. 63
4.5 Defect map to be used within the parameter studies on photothermal SR reconstruction with pixel pattern illumination. 71
4.6 Study results on the dependence of the pixel cluster size on the reconstruction quality for three different defect separation distances. 73
4.7 Reconstructed defect pairs for a separation distance of $d_{\mathrm{sep}} = 0.5\,\mathrm{mm}$ and three different cluster sizes. 74
4.8 Study results on the dependence of the number of measurements performed on the reconstruction quality for three different defect separation distances. 75
4.9 Data points as shown in Figure 4.8 plotted with logarithmic y-scale. 76
4.10 Reconstructed defect pairs for three different number of measurements and $d_{\mathrm{sep}} = 0.5\,\mathrm{mm}$. 77

5.1 OuT specifically designed for the experimental validation of two-dimensional photothermal SR reconstruction. 80
5.2 ROIs used for the experimental validation of the proposed SR reconstruction methodology. 81
5.3 Laboratory setup for validating the sequential laser scanning experimental approach. 82
5.4 Reconstruction results obtained from the sequential laser scanning measurement approach. 84
5.5 Sectional view of the reconstructions presented in Figure 5.4. 85
5.6 Schematic of a DMD-based DLP-projector. 87
5.7 DLP-projector used to project two-dimensional structured pixel patterns onto the ROI. 88
5.8 I/O-capabilities of the DLP-projector in use. 88

5.9 Laboratory setup for validating the two-dimensional pattern projection experimental approach. 89
5.10 Interoperation diagram of the utilized hardware for pattern projection based photothermal SR reconstruction. 91
5.11 Reconstruction results obtained from the pattern projection experimental approach. 92
5.12 Quality of the forward solution and estimation of ζ. 93
5.13 Influence of the pixel cluster size on the quality of the presented forward model. 95
5.14 Experimental validation of the numerical study on the influence of the number of performed measurements on the reconstruction quality. 96

6.1 Maximum thermogram for a homogeneous illumination of the whole OuT as presented in Figure 5.1. 97
6.2 Qualitative comparison of the reconstruction results obtained via the sequential laser scanning approach with well-established TT methods. 101
6.3 Sectional view of the data presented in Figure 6.2 at $y_{\text{eval}} = 1.8\,\text{mm}$. 102
6.4 Qualitative comparison of the reconstruction results obtained via the pattern projection approach with well-established TT methods. 104
6.5 Sectional view of the data presented in Figure 6.4 at $y_{\text{eval}} = 2.8\,\text{mm}$. 105

7.1 Current state and vision for two-dimensional photothermal SR reconstruction . 110

A4.1 Spectral luminous efficacy of the human eye for photopic vision. 118

List of Tables

2.1 Thermal properties of a selected set of materials. 6
2.2 Common boundary conditions for PDEs. 10

4.1 Proximal operators for a set of common regularization tasks. 52
4.2 Experimental parameters of the presented SR reconstruction approach. 65
4.3 Candidate metrics for quantitatively comparing SR reconstruction results. . . . 68
4.4 Shared experimental parameters assumed for the subsequent parameter studies on photothermal SR reconstruction with pixel pattern illumination. 72
4.5 Illumination parameters used for studying the influence of $n_{\text{clustered}}$ on the reconstruction quality of SR reconstruction with pixel pattern illumination. . . 73

4.6 Illumination parameters used for studying the influence of n_m on the reconstruction quality of photothermal SR reconstruction with pixel pattern illumination. 75

5.1 Properties of the OuT designed for experimental validation of 2D-SR reconstruction. 80
5.2 Experimental parameters for validating the sequential laser scanning approach. 83
5.3 Regularization parameters utilized to obtain the reconstruction results as presented in Figure 5.4. 85
5.4 Experimental parameters for validating the two-dimensional pattern projection approach. 90
5.5 Regularization parameters utilized to obtain the reconstruction result as presented in Figure 5.11. 92

6.1 Overview over all applied metrics for quantitative comparison of different thermographic data processing methods with photothermal SR reconstruction. 99
6.2 Proposed metrics evaluated for the trivial all zeros dataset for both investigated ROIs. 100
6.3 Comparison metrics results for the SR reconstructions obtained by the sequential laser scanning experimental approach. 103
6.4 Comparison metrics results for the SR reconstructions obtained by the two-dimensional pattern projection experimental approach. 105

A4.1 Different projector types with typical brightness, radiant flux and max. reasonable ROI sizes for TT. 119

List of Algorithms

4.1 Basic ADMM algorithm for solving regularized multiplicative minimization problems. 51
4.2 Sparse Matrix Stacking Reconstruction. 55
4.3 Frequency Domain Reconstruction. 57
4.4 Pseudo-random pattern generation. 64